



Minimally-invasive Theranostics based on Triplet-Triplet Annihilation

DISSERTATION

zur Erlangung des akademischen Grades
Doctor rerum naturalium (Dr.rer.nat.)

im Promotionsfach Physikalische Chemie
am Fachbereich Chemie, Pharmazie, Geographie und
Geowissenschaften
der Johannes Gutenberg-Universität Mainz

vorgelegt von

Nadzeya Nazarova

geboren in Pinsk, Weißrussland

Mainz, Januar 2020

Die vorliegende Arbeit wurde im Zeitraum von Dezember 2015 bis August 2018 am Max-Planck-Institut für Polymerforschung im Arbeitskreis von [REDACTED] unter der Betreuung von [REDACTED] angefertigt.

Gutachter:

[REDACTED]

Max-Planck-Institut für Polymerforschung, Mainz

[REDACTED]

Johannes Gutenberg-Universität, Mainz

Dekan:

[REDACTED]

Johannes Gutenberg-Universität, Mainz

Tag der Verteidigung: 24. Juni 2020

Erklärung

Hiermit versichere ich, die vorliegende Arbeit selbstständig und ohne Benutzung anderer als der angegebenen Hilfsmittel angefertigt zu haben. Alle Stellen, die wörtlich oder sinngemäß aus Veröffentlichungen oder anderen Quellen entnommen sind, wurden als solche eindeutig kenntlich gemacht. Diese Arbeit ist in gleicher oder ähnlicher Form noch nicht veröffentlicht und auch keiner anderen Prüfungsbehörde vorgelegt worden.

Nadzeya Nazarova

Mainz, Januar 2020

Abstract

Simultaneous and real-time sensing of specific cellular parameters can be achieved by the use of multifunctional nanocarriers. Multifunctional nanocarriers combine multiple properties in single particles, and enable minimally invasive and all-optical monitoring of specific physiological parameters at a cellular level with unprecedented efficiency and sensitivity.

This study is devoted to the synthesis of entirely organic upconversion nanoparticles (UCNPs) and to the investigation of their unique optical properties and cytotoxic effects. These UCNPs provide an excellent platform to construct multifunctional nanocarriers for various biomedical applications, because of their anti-Stokes luminescence properties and strong dependence of the efficiency of triplet-triplet annihilation assisted upconversion (TTA-UC) on the local temperature and oxygen content.

This thesis includes an up-to-date literature review on the application of UCNPs as a therapy and diagnostics (theranostic) platform. The thesis also describes: i) the fundamental theoretical aspects of the TTA-UC; ii) the advantages of the use of this TTA-UC process for biosensing purposes; iii) the requirements to the structural and energetic characteristics of the couples of sensitizer/emitter; iv) and a theoretical prediction for the maximal quantum yields of delayed emitter fluorescence (dEF) and residual sensitizer phosphorescence (rSPh).

The selected matrix composition for UCNPs formation is entirely biocompatible, mostly consisting of natural waxes and vegetable oils. Spectroscopic techniques were used to assess the effectiveness of the TTA-UC process in organogel matrix and UCNPs. The matrix material ensures the significant increase of the rotational diffusion of the optically active molecules for a temperature interval centered at 36 °C. The optimal UCNP-composition (Y-894 / DBOV-Mes in rice bran oil 30 wt.% / squalene 30 wt.% / carnauba wax 40 wt.% / Tween-20) demonstrates the monotonic increase of the dEF-signal and decrease of the rSPh-signal at monotonically increasing the sample temperature, that leads to exclusively sustainable T-calibration curve. The obtained UCNP-composition demonstrates highly stable dispersions with pronounced oxygen scavenging ability.

We have determined the cytotoxicity of the UCNPs and their optimal concentration for efficient intracellular T-sensing through the cooperation with the biologists from our group. The upper limit of the solid content of the sensing UCNPs ($1250 \mu\text{g mL}^{-1}$) demonstrates high T-sensitivity – up to 250 mK, optically achieved in the ambient environment, around the life-science relevant temperature of $T = 36 \text{ }^\circ\text{C}$. The UCNPs are well tolerated by bio-objects and highly suited for biomedical applications as suggested by the fluorescence microscopy of cellular uptake process and cytotoxicity test.

Additionally, we studied external-stimuli responsive protection of excited triplet states against deactivation by singlet oxygen. The sacrificial singlet oxygen scavenging capability of N-butyl-2-pyridone provides long-term protection of the triplet-triplet annihilation photon energy upconversion process against photooxidation.

Zusammenfassung

Die Entwicklung multifunktionaler Nanoträger, die in der Lage sind, bestimmte Zellparameter gleichzeitig in Echtzeit zu erfassen, ist für viele Forscher weiterhin eine vorrangige Aufgabe. Eine Einzigartigkeit solcher Nanoträger beruht auf einer Kombination mehrerer nützlicher Eigenschaften in einem Partikel. Dies ermöglicht ein minimal invasives und rein optisches Monitoring spezifischer physiologischer Parameter auf zellulärer Ebene mit bisher unerreichter Effizienz und Empfindlichkeit.

Diese Studie befasst sich mit der Synthese von Aufkonversions-Nanopartikeln (UCNPs), die vollständig aus organischen Materialien bestehen, und der Untersuchung ihrer einzigartigen optischen Eigenschaften und zytotoxischen Effekte. Ihre Eigenschaften der Anti-Stokes-Lumineszenz, eine starke Abhängigkeit der Effizienz des durch Triplet-Triplett-Annihilation unterstützten Aufkonversions-Prozesses (TTA-UC) von der lokalen Temperatur und des Sauerstoffgehalts bieten eine hervorragende Plattform für den Aufbau solcher multifunktionaler Nanoträger für verschiedene biomedizinische Anwendungen.

Diese Arbeit enthält eine aktuelle Literaturübersicht über die Anwendung von UCNPs als theranostische Plattform. Die Arbeit beschreibt auch i) die grundlegenden theoretischen Aspekte von TTA-UC; ii) die Vorteile der Verwendung dieses TTA-UC-Verfahrens für Biosensingzwecke; iii) die Anforderungen an die strukturellen und energetischen Eigenschaften der Sensibilisator / Emitter-Paare; iv) und eine theoretische Vorhersage für die maximalen Quantenausbeuten der Fluoreszenz-verzögerten Emitter (dEF) und der restlichen Sensibilisatorphosphoreszenz (rSPh).

Die für die Bildung von UCNPs ausgewählte Matrixzusammensetzung ist vollständig biokompatibel und besteht hauptsächlich aus natürlichen Wachsen und Pflanzenölen. Spektroskopische Techniken wurden verwendet, um die Wirksamkeit des TTA-UC-Prozesses in Organogelmatrix und UCNPs zu bewerten. Das Matrixmaterial sorgt für eine signifikante Erhöhung der Rotationsdiffusion der optisch aktiven Moleküle für ein Temperaturintervall von 36 °C. Die optimale UCNP-Zusammensetzung (Y-894 / DBOV-Mes in Reiskleieöl 30 Gew.% / Squalen 30 Gew.% / Carnaubawachs 40 Gew.% / Tween-20) zeigt die monotone Zunahme des dEF-Signals und Abnahme des rSPh-Signals bei monotoner Erhöhung der Proben temperatur, so dass eine ausschließlich nachhaltige T -

Kalibrierungskurve erhalten wird. Die erhaltene UCNP-Zusammensetzung zeigt hochstabile Dispersionen mit ausgeprägtem Sauerstoffaufnahmevermögen.

Aufgrund der Zusammenarbeit mit Biologen aus unserer Gruppe wurde die Zytotoxizität der UCNPs und die optimale Konzentration der UCNPs für ein effizientes intrazelluläres T-Sensing bestimmt. Die Obergrenze des Feststoffgehalts der abführenden UPNPs ($1250 \mu\text{g mL}^{-1}$) zeigt eine hohe T-Empfindlichkeit - bis zu 250 mK, die in der Umgebung optisch erreicht wird, um die Life-Science-relevante Temperatur von $T = 36 \text{ }^\circ\text{C}$. Die Fluoreszenzmikroskopie des Zellaufnahmeprozesses und des Zytotoxizitätstests legen nahe, dass die UCNPs von Bioobjekten gut vertragen werden und sich hervorragend für biomedizinische Anwendungen eignen.

Zusätzlich wurde der Schutz angeregter Triplettzustände durch externe Stimuli gegen Deaktivierung durch Singulett-Sauerstoff untersucht. Das Opfer-Singulett-Sauerstofffangvermögen von N-butyl-2-pyridon bietet einen Langzeitschutz eines Aufwärtsumwandlungsprozesses von Triplett-Triplett-Annihilationsphotonenenergie gegen Photooxidation.

List of contents

Abstract	1
Zusammenfassung	3
List of contents	5
Motivation and objectives	9
Chapter 1: Introduction	11
1.1 Biology of cancer cells.....	11
1.2 Intracellular techniques for oxygen concentration and temperature measurements	13
1.3 Nanocarriers applied to diagnostic and therapeutic purposes	15
1.3.1 Organic nanoparticles.....	16
1.3.2 Inorganic nanoparticles	18
1.4 Nanocarriers for TTA-UC.....	19
Chapter 2: Triplet-triplet annihilation upconversion: mechanism description and fundamental principles	21
2.1 The mechanism of the TTA–UC process.....	21
2.2 Requirements for the TTA-UC.....	23
2.3 Energy losses in the TTA-UC process	24
2.4 The sensitivity of the TTA-UC to environmental parameters	26
2.4.1 Oxygen effect on the TTA-UC process.....	26
2.4.2 Temperature effect on the TTA-UC process.....	28
Chapter 3: Stimuli-responsive protection of optically excited triplet ensembles against deactivation by molecular oxygen	31
3.1 Introduction.....	31
3.2 Reversible binding of oxygen to aromatic compounds	33
3.3 Experimental part	34
3.3.1 Materials.....	34
3.3.2 Method	36
3.4 Results and discussion.....	37
3.4.1 N-butyl-2-pyridone effect on the TTA-UC process.....	37
3.4.2 Solvation shell tuning.....	40
3.4.3 Temperature effect	42

3.5 Conclusions.....	46
Chapter 4: Optical temperature sensing in organogel matrices via annihilation upconversion.....	47
4.1 Introduction.....	47
4.2 Vegetable oils as singlet oxygen scavengers	48
4.3 Natural waxes as a temperature dependent matrix	50
4.4 Ratiometric temperature sensing.....	52
4.5 Experimental part	55
4.5.1 Materials.....	55
4.5.2 Method	57
4.5.3 Sample preparation	57
4.6 Results and discussion.....	58
4.6.1 Organogel matrices containing emitter molecules with different amphiphilicity ...	58
4.6.2 Temperature dependence of composition-tunable organogel matrices.....	60
4.6.3 Organogel matrices containing different vegetable oils	62
4.6.4 UC-organogel matrix composition with maximal temperature sensitivity	63
4.6.5 Amphiphilic additives effect on ratiometric temperature response of UC-organogel matrices.....	64
4.7 Conclusions.....	70
Chapter 5: Sensing technique based on solid lipid upconverting nanoparticles..	73
5.1 Introduction.....	73
5.2 Optical properties of tissue and requirements to sensing tool	74
5.3 Sensing procedure	75
5.4 Experimental part	76
5.4.1 Materials.....	76
5.4.2 UC solid lipid nanoparticles synthesis	79
5.4.3 Methods.....	80
5.4.3.1 Luminescence measurements.....	80
5.4.3.2 Scanning electron microscopy.....	81
5.4.3.3 Particle size analysis	81
5.4.3.4 Fluorescence microscopy.....	82
5.5 Results and discussion.....	82

5.5.1 Particle characterization	82
5.5.2 Efficiency of dEF and rSPh as a function of solid-liquid lipid ratio in a matrix core of UC-SLNPs.....	84
5.5.3 Oxygen sensitivity of UC-SLNPs	85
5.5.4 Temperature sensitivity of UC-SLNPs.....	89
5.6 Cytotoxicity studies of UC-SLNPs	95
5.6.1 Cytotoxicity test of surfactants.....	95
5.6.2 Definition of the upper limit of cytotoxic concentration of UC-SLNPs	97
5.6.3 Visualization of UC-SLNPs.....	100
5.6.4 Uptake mechanism of UC-SLNPs by HeLa cells.....	102
5.7 T-sensing in cell cytoplasm environment.....	103
5.7.1 Optimization of T-sensing system	103
5.7.2 Intracellular T-sensing in HeLa cells.....	106
5.8 Conclusion.....	108
Summary and conclusions	109
References	111
List of abbreviations	123
Acknowledgments	127
Scientific contributions	129

Motivation and objectives

All the biochemical reactions responsible for the cellular functions occur either exothermically or endothermically at particular locations within the cell organelles exposed to different oxygen conditions. They are fundamentally co-regulated by the intracellular temperature distribution. In a living object, the intracellular oxygen concentration, as well as the local temperature, is tightly regulated and maintained within the narrow physiological limits. For the normal vital activity and metabolism, cells keep up such crucial parameters of the intracellular environment like temperature and oxygen content in narrow physiological limits.^{1,2} The deviation above or below these limits leads to cell dysfunction and may subsequently provoke different disturbances in an organism.

In an ideal case, minimally-invasive intracellular oximetry and thermometry could allow us to monitor physiological and metabolic parameters in biological specimens, and consequently would allow us to evaluate the efficiency of drug treatment or other external stimuli, such as chemical and environmental stress.³ However, despite broadly studied, it is still a considerable technological challenge to perform the intracellular minimally-invasive real-time monitoring of local oxygen concentration and local temperature distribution.

Miniaturization of the optical sensing tools is an essential step for the development of biomedical sensing techniques and devices. The miniaturization enables the detection of studied parameters with the required sensitivity and selectivity. Optical sensing has an additional requirement in terms of spectral mismatch: there are strongly contradictive demands for the wavelength of the excitation light.⁴ As a consequence of the tissue transparency properties, wavelengths at the range of $\Delta\lambda \sim 700 \div 940$ nm are well transmitted, while photons with enough high energy, namely $\lambda \ll 700$ nm, can initiate biochemical processes and serve as a sensing tool.⁴

A possible solution to these sensing problems is the process of triplet-triplet annihilation assisted upconversion (TTA-UC). The TTA-UC-based sensing technique uses a ratiometric material response on the acting parameter (sample temperature, local viscosity change, or variation of the oxygen concentration) instead of single material response. The TTA-UC relies on optically created densely populated organic triplet

ensembles, in which the inter-molecular energy transfer depends strongly on a variety of environmental parameters, such as temperature, viscosity, the presence of heavy metal atoms or oxidizing agents, as well as on the contamination with molecular oxygen. The use of the mutual dependence of the residual sensitizer phosphorescence (rSPh) and emitter delayed fluorescence (dEF) on the acting parameter ensures the elimination and compensation measurement errors. There is a variety of distortion factors affecting the signal observed: the influence of measurement conditions on the emission intensity, fluctuations in excitation and instabilities in detection, concentration, or inhomogeneous distribution of the sensing material.⁵

Furthermore, TTA-UC is the only upconversion method that has been experimentally demonstrated to operate with noncoherent low-intensity illumination such as sunlight.⁶ This unique process allows the generation of high-energy photons from the lower-energy excitation photons at very low intensity, and extremely low spectral power density of the used optical source.^{7,8}

The miniemulsion polymerization method is an effective strategy for the synthesis of novel nanomaterials, in which the structure, morphology, and size parameters can be easier controlled in comparison with other heterophase polymerization methods.^{9,10} The miniemulsion process allows the encapsulation of molecular compounds, liquids, or solid materials (e.g., dyes, photoinitiators, drugs, or DNA) inside the nanoparticles.¹¹ Thus, a variation of encapsulated materials enables to obtain nanoparticles with desired properties.

Merging the techniques of annihilation upconversion and miniemulsion polymerization leads to the creation of ultimate sensing tools, demonstrating simultaneous, real-time and spatially local – temperature and oxygen sensing in living objects.^{12,13}

The objective of this thesis is to demonstrate the main advantage of the realized experimental system, namely that both temperature (T) and molecular oxygen (O_2) – sensing procedures can be performed via a single nano-confined object, delivering complete independent optical signals, revealing the local temperature and oxygen concentration.

Chapter 1: Introduction

Despite the remarkable progress in cancer research, cancer continues to be challenging for modern medicine. The chance of curing will significantly increase if cancer is diagnosed at early-stage of the disease and then treated adequately. Despite the progress made in improving cancer diagnostic approaches using techniques such as computed tomography (CT), magnetic resonance imaging (MRI), single photon emission computed tomography (SPECT), positron emission computed tomography (PET), and their hybrid techniques, including SPECT/CT, PET/CT, and PET/MRI,¹⁴⁻²³ the development of non-invasive, high precision and ultrasensitive techniques for early diagnosis remains one of the priority tasks for the scientific community. Since the existing cancer screening techniques have some limitations, such as being expensive and time-consuming, they also have the risk of side effects, for instance, they are not suitable for young women (in case of diagnostic mammography).²⁴ Therefore, there is a need to identify a technology that can improve the precision and accuracy of an early cancer detection.

In recent years, the use of nanocarriers (polymer-drug conjugates, polymer-protein conjugates, liposomes, polymeric nanoparticles, polymersomes, micelles, nanoshells, immunotoxins, immunopolymers) as a diagnostic, prognostic, and therapeutic platform for various biomedical applications has been increased vastly – at least on the *in vitro* level, especially for the potential cancer treatment.²⁵⁻²⁷ Advances in nanocarrier engineering have contributed to the development of novel nanoscale biosensing approaches. These approaches may help in understanding the mechanisms of diseases at the cellular level and recognition of the disease at an early stage, and also can be used for the monitoring early response of the disease to actual treatment and evaluate treatment efficacy.

1.1 Biology of cancer cells

Healthy cells become tumor cells through the mutations taking place in deoxyribonucleic acid (DNA). Generally, when the DNA sequences are injured, the cells activate their repair mechanism or programmed process of cellular self-destruction in the dependence on a

degree of damage.²⁸ Unfortunately, in some cases, cancer cells can acquire mutations or other changes. That allows to escape the detection by the immune system and the tumor is progressing.²⁹ The tumor progression is considered as a process involving mutation and selection of cells with the progressively increasing capacity for proliferation, survival, and invasion.²⁸

Extracellular and intracellular microenvironments of healthy and diseased tissues exhibit differences in temperature, oxygenation, pH value, redox potentials, protein and enzyme concentrations.³⁰ Altered cellular metabolism is one of the most obvious cancer hallmarks.³¹ In a cancer metabolic reprogramming increased glucose uptake into the cells is observed. The cells produce much less adenosine 5'-triphosphate (ATP) from aerobic glycolysis (only 2 ATPs per mole of glucose), whereas oxidative phosphorylation in healthy cells generates up to 36 ATPs upon complete oxidation of one glucose molecule. This inefficient ATP-producing metabolic pathway in cancer cells is known as the Warburg effect.³² Compared to the healthy cells which are using glycolysis only when oxygen supply is limited (anaerobic glycolysis), the cancer cells prefer using glycolysis even in normoxic conditions.³³ Aerobic glycolysis is a result of an energy dysregulation in cancer cells driven by various factors, such as activation of oncogenes, loss of tumor suppressors, and mitochondrial DNA mutation.³²

Oxygen supply in tumor tissues is not regulated according to the metabolic demand, as is the case with healthy tissues.³⁴ Median oxygenation in healthy tissues averages about 5% oxygen and ranges from about 3% to 7.4%, at physiological hypoxia from 2% to 6% oxygen.²⁹ Importantly, that oxygen level severely reduces in tumor cells and ranges between approximately 0.3% and 4.2% oxygen.³⁵ Hypoxia, or reduced oxygenation, may identify an aggressive phenotype of tumors which is resistant to conventional cancer therapies.³⁴ The tumors with large pathological hypoxia regions may have a better ability to metastasize than well-oxygenated tumors.³⁶ Clinical studies have clearly shown that the presence of hypoxic regions in tumors significantly reduces the overall survival of patients.³⁷

Temperature plays a vital role in many cellular processes such as cell metabolism, cell division, and gene expression.³⁸ The local temperature depends on thermoregulatory mechanisms and exo-endothemic biochemical processes, which are altered in

pathology.³⁹ Since blood flow to the tumor tissue is significantly less than to healthy tissue, thermal energy generated by the tumor metabolism is carried away less rapidly from the tumor than from the healthy tissue. Thus, the tumor tissue is characterized by a higher temperature than the healthy tissue due to impaired thermoregulatory mechanisms.³⁹

The intracellular thermometry and oximetry are considered to be accurate indicators of cell behavior.³⁵ The deviation of these essential parameters from the physiological norm reflects different disturbances in the cells and can be used as an indicator of a number of diseases, including various types of cancer. Therefore, the development of a nanoscale minimally-invasive and bio-acceptable prognostic tool possessing high sensitivity to the detection of pre-cancerous or cancerous changes in cells can help clinicians and oncologists to decide about adequate therapy approaches and to consequently improve the quality and expectancy of life.

1.2 Intracellular techniques for oxygen concentration and temperature measurements

Biosensors are analytical devices that are capable of providing the conversion of a biological response into a quantifiable and processable signal.⁴⁰ The biosensors can broadly be classified into different classes according to the type of signal transduction (optical, electrochemical, thermometric, piezoelectric or magnetic) or the type of biorecognition element (nucleic acid, enzymes, proteins, antibodies, and cells).⁴¹ Optical biosensors are more versatile than other types of biosensors. The optical biosensing mechanism is based on the interaction of the optical field with a biorecognition light-sensitive object and the registration of a converted signal in dependence on an acting parameter.⁴² Generally, optical biosensing can be implemented by two detection protocols: label-free (evanescent wave fluorescence, bioluminescent optical fibre, surface plasmon resonance and localized surface plasmon resonance, reflectometric interference spectroscopy, waveguide interferometric, ellipsometric, surface-enhanced Raman scattering biosensors) and label-based (fluorescent labeling, isotopic labeling, chemiluminescent labeling, electrochemically active probe labeling, and nanoparticle labeling).^{43, 44} In a label-free detection method the measured signal is generated directly

by the interaction of the analysed material with the transducer,⁴² while the label-based detection method employs a label and the measured signal is generated by a colorimetric, fluorescent or luminescent method.⁴²

A commercial biosensor that is capable to carry out minimally-invasive, simultaneous and independent quantitative measurements of cellular temperature and oxygen concentration has not been demonstrated yet, regardless of the considerable amount of conducted research. The current employing tools for measuring tissue oxygenation (pO_2) such as oxygen polarographic electrodes, the OxyLite fluorescence-quenching technique, direct injection of oxygen-sensitive NMR probes based on fluorine are invasive and limited in *in vivo* application.⁴⁵ The present developments and techniques, that are used to measure the internal temperature of living cells, are based on luminescent and non-luminescent thermometry. As thermal probes in the luminescent thermometry organic dyes, QDs, or Ln^{3+} ions, can be encapsulated in polymer and organic–inorganic hybrid matrices. Non-luminescent thermometry encompasses scanning thermal microscopy, nanolithography thermometry, carbon nanotube thermometry, and biomaterials thermometry.^{46,47} Many of these techniques have several restrictions such as being toxic, getting affected by the cell components, being not user-friendly and needing bulky equipment.⁴⁷

Currently, the methods based on phosphorescence and fluorescence are most commonly used for biosensing applications.^{48,49} The approaches based on fluorescence or phosphorescence intensity measurements and oxygen-dependent quenching of fluorescence or phosphorescence are well-established techniques with excellent sensitivity to temperature and specificity to oxygen.⁵⁰⁻⁵³ However, the sensing techniques based on these optical processes have the lack of reliability, since phosphorescence and fluorescence are integral parameters depending simultaneously on several environmental parameters such as the local temperature, local oxygen contamination, and also molecular concentration fluctuations of dye molecules and their photobleaching.^{53,54}

The optical sensing based on the triplet-triplet annihilation upconversion process (TTA-UC) represents a new approach for testing the physiological parameters of living objects. The sensing process involves an optical excitation of upconverting dyes at so-called

upconversion regime, followed by ratiometric registration of two optical signals – delayed emitter fluorescence (dEF) and residual sensitizer phosphorescence (rSPh) – as a function of the local temperature in an oxygen environment. The use of the mutual dependence of the rSPh and dEF on the acting parameter ensures inherent/instantaneous compensation regarding other unwanted local changes of the sample parameters.⁵⁵ The excitation at the tissue transparency window combined with extremely low excitation intensity and ratiometric type registration ensures a high signal to noise ratio, keeping the sensing procedure minimally invasive.

1.3 Nanocarriers applied to diagnostic and therapeutic purposes

The use of nanocarriers as biosensing instruments, smart imaging agents, and targeted drug delivery systems significantly influences the effectiveness of the cancer diagnostic methods and treatment approaches. Many nanomaterials such as polymer-based nanomaterials, liposomes, quantum dots (QD), carbon-based nanomaterials, metal- or oxide-based nanomaterials, UCNPs possess intrinsic therapeutic/diagnostic potential due to physical and biochemical properties.⁵⁵⁻⁵⁷ Each of these nanomaterials can be modified with polymers, nanocomplexes, other nanoparticles, dendrimers, macromolecular scale complexes, or biomolecules such as proteins, antibodies, antigens, and can produce a multitude of modifications to achieve higher selectivity.⁵⁸ For the development of nanomaterials with high specificity regardless of the application, several factors should be taken into account, including their size, shape, modifications, composition, stability, biocompatibility, biodegradation, and biodispersion.^{58,59} These parameters can improve the nanomaterial performance in biological systems and, consequently, their capabilities. Carrier materials can be broadly classified into two groups: organic carriers and inorganic carriers. Regardless the nature of the carrier material, the outer surface of the carrier should be hydrophilic to ensure an effective nanoparticle distribution in blood circulatory system.⁶⁰

Most of the organic nanocarriers can be obtained by self-assembly or chemical binding of small organic building blocks (“bottom-up” techniques) for fabrication a wide range of the organic systems such as micelles, liposomes, polymersomes, vesicles, polymer

conjugates, capsules, dendrimers, and polymeric NPs. In the “top-down” techniques, large objects have to be disintegrated. Here are the most common techniques: the mechanical milling, microfluidics and lithography. The organic nanocarriers can load molecules either by conjugation on the surface or in the core, or by physical encapsulation, which makes them promising drug delivery systems.^{55,61}

There are three techniques for producing inorganic nanocarriers: physical methods (pulsed laser ablation, vapor condensation), chemical syntheses, and mechanical processes (bead milling). The photophysical properties of inorganic nanocarriers combined with their ability to be functionalized with biomolecules make them promising nanostructure for a variety of bioanalytical purposes: ions detection, detection of organic compounds, detection of biomolecules, pH nanosensor.⁶² In particular, metal and metal oxide NPs are being investigated intensely for therapeutic and imaging applications.

1.3.1 Organic nanoparticles

Organic nanoparticles can be commonly described as solid particles composed of organic compounds (mainly lipids or polymers) ranging in diameter from 10 nm to 1 μm .⁶³ Such a type of nanoparticles has attracted significant attention due to their excellent biocompatibility, low toxicity, and potential applications in biosensorics, medical photonics, bioimaging, and so forth.^{55,64-68}

The main groups of organic nanocarriers include carbon, polymer, and lipid-based nanocarriers. Their organic nature minimizes intrinsic toxicity and makes them suitable for the incorporation of both therapeutic agents and imaging agents in a single nanocarrier. That allows the potential for combining treatment and diagnosis (theranostics).

Liposomes are the most studied colloidal nanocarrier systems in the perspective of drug delivery vehicles. Conventional liposomes (“first-generation liposomes”) are artificially prepared vesicles made of a lipid bilayer composed of natural or synthetic lipids.⁶⁹ The main disadvantages of the possible applications of the conventional liposomes as drug delivery systems are their high uptake by the macrophages and consequent removal from the blood circulation.⁶⁹ The liposomes with modified surfaces (“second-generation

liposomes”) allow inhibiting the detection mechanism by the phagocytes system and extend the blood circulation periods of nanocarriers. The presence of biocompatible synthetic polymers poly-ethylene glycol (PEG) derivatives or poly(ethyl ethylene phosphate) (PEEP) on outer membranes leads to an adsorption of specific proteins which provide the stealth effect.⁷⁰

The first US Food and Drug Administration (FDA) approved an organic anticancer nano-drug (1995) is Doxil® (doxorubicin hydrochloride liposome injection).⁷¹ Doxil® has been approved for AIDS-related Kaposi’s sarcoma for the treatment of platinum-based chemotherapy-resistant ovarian cancer and multiple myeloma, as well as for metastatic breast cancer.^{71,72} The Doxil’s® action leads to slow down or stop cancer cell growth.⁷¹ Various novel nano-drug formulations based on similar so called “stealth” liposomes or other organic nanocarriers loaded with different active drugs or with drug combinations are widely investigated now. The organic drug carrier, approved by the FDA in October 2015, is Onivyde® (nanoliposomal formulation of irinotecan).⁷³ Onivyde® is intended for the treatment of gemcitabine-based chemotherapy-resistant metastatic adenocarcinoma of the pancreas.^{72,74} The mechanism of Onivyde’s® action is based on the effect of component irinotecan, and its metabolite SN-38 on cancer cells causing DNA damage and cell death.⁷⁴

Many FDA-approved nano-drugs are based on polymers. Plegridy® (peginterferon beta-1a) was approved for the treatment of relapsing-remitting multiple sclerosis, Adynovate® (antihemophilic factor) for bleeding prophylaxis and the treatment of acute bleeding in hemophilia A,⁷⁵ Zilretta® (triamcinolone acetonide extended-release injectable suspension) was approved in October 2017 for the treatment of osteoarthritis knee pain.⁶⁰ Many polymer-containing formulations of nano-drugs are being investigated in clinical trials.⁷⁵

Many of the liposomal nanoformulations of drugs are under clinical investigation. Arikayce® (liposomal formulation of amikacin) is intended for the treatment of serious chronic lung infections, as well as Pulmaquin® (combines liposomal and aqueous-phase ciprofloxacin) for patients with either cystic fibrosis. More complex liposomal drug delivery systems are also in the clinical phase trials. ThermoDox® (lysolipid thermally sensitive liposome) represents a thermally sensitive liposomal encapsulation of doxorubicin which

rapidly changes the structure when it is exposed to high heat (~ 41 °C) and intended for the treatment of a wide range of cancers.⁷² On reaching microvessels within a heated tumor, the drug is released and quickly penetrates tumor cells.⁷⁶ In this way, a site-specific release of the drug is achieved.

By choosing appropriate materials and design features, organic-based nanoparticles can demonstrate stimuli-responsiveness. These nanoparticles can sense physiological changes within an organism, providing powerful opportunities in next-generation diagnostics.⁷⁷

1.3.2 Inorganic nanoparticles

Inorganic nanoparticles have a vast potential in modern biomedical applications due to their unique material- and size-dependent physiochemical properties.⁵⁵ In particular, optical, magnetic and electrical properties, in addition to stability, and ease of functionalization, make the inorganic nanoparticles attractive alternatives for diagnostic and therapeutic purposes.⁷⁸

The inorganic nanoparticles include noble metal, metal oxide, semiconductor and silica-based nanoparticles. They exhibit magnetic, electrical and optical properties.⁷⁹ These physical properties can be varied by changing the size, shape, and surface modifications of the NPs. Some inorganic NP-based agents have already been clinically approved, such as aminosilane-coated superparamagnetic iron oxide nanoparticles designed for tumor therapy (glioblastoma) using local tissue hyperthermia, the iron oxide-based nanoparticles are also employed as magnetic resonance imaging (MRI) contrast agent (Feraheme®) for the detection and characterization of especially small focal liver lesions.^{72,77}

The toxicity of inorganic NPs is an unavoidable aspect of concern for *in vivo* applications. The surface modification with different inorganic/organic molecules, polymers such as hydrophobic or hydrophilic, neutral or charged, synthetic or natural may reduce their toxicity⁸⁰⁻⁸³ and improve functionality. For example, the surface coating of magnetic NPs ensures preventing the release of toxic ions from a magnetic core into biological media and shielding the magnetic core from oxidation and corrosion.⁶⁷ The specific surface

coating of NPs inhibits the adsorption of plasma proteins during *in vivo* applications, thus achieving the NPs circulation time in blood for longer and maximizes the possibility to reach target tissues.⁸³

1.4 Nanocarriers for TTA-UC

In recent years, upconversion-luminescence materials have drawn widespread interest in biomedical research, because it enables an increasing excitation penetration depth in tissue by using the longer wavelength of the incident light, compared with conventional downconversion-luminescence materials. There are various optical mechanisms for realizing the upconversion processes such as two-photon absorption, second harmonic generation, lanthanide (Ln^{+3}) based upconversion, and TTA-UC. Among the various principles of light upconversion, TTA-UC is the only upconversion method that has been experimentally demonstrated to operate with noncoherent low-intensity illumination (in order of $\text{mW}\cdot\text{cm}^{-2}$).¹⁷ This unique process allows the generation of high-energy photons from lower-energy excitation photons at very low intensity and extremely low spectral power density of the optical source used.^{18,19} The TTA system consists of a sensitizer molecule (absorbing species) and an emitter molecule (emitting species), both form the energetically optimized upconversion dyes pair. An additional advantage for the wide application of the TTA-UC based techniques in medicine is also an extensive library of upconversion dyes: a required wavelength range of excitation and emission can be carried out by a selection of appropriate sensitizer and emitter pairs. Since all optical properties of biological tissues regarding light penetration must be taken into account. The lower energy photons can penetrate in tissues much deeper than photons with high-energy.⁵³

Nanoparticles for upconversion have emerged as promising agents for biological sensing, imaging technologies, and theranostics. To date, most of the reported luminescent nanothermometers, which are used to detect the local temperature of a living cell with sub-micrometric spatial resolution, are developed by using lanthanide and transition metal based upconversion nanoparticles.⁵³ In contrast, the TTA-UC based nanoparticles were mainly fabricated for bioimaging applications.^{55,72,84,85} However, inorganic

nanoparticles are more toxic and limited for *in vivo* applications in comparison with organic nanoparticles.⁵⁵ The synergy of the organic nanoparticle biosafety and the TTA-UC process advantages in one biosensing tool provides the creation of a new approach for simultaneous, real-time and spatially local thermometry and oximetry in living objects.^{12,13}

Chapter 2: Triplet-triplet annihilation upconversion: mechanism description and fundamental principles

This chapter provides a brief overview of the mechanism and fundamental principles of the TTA-UC process, which will help in the understanding of the research presented in this thesis. The general fundamental concepts, terms, and definitions related to the presented work are explained in short. This section will also focus on the critical role of oxygen and its influence on the TTA-UC process.

2.1 The mechanism of the TTA-UC process

Photon upconversion is an anti-Stokes emission process that involves the conversion of lower energy photons into higher energy photons. The photon upconversion, based on TTA, also known as p-type delayed fluorescence, was first reported by Parker and Hatchard in 1962 within the pairs of phenanthrene–naphthalene and proflavin–anthracene.⁸⁶ However, only in the 21st century, the process has found wide applications in bioimaging, biosensing, and may be used for drug delivery (phototriggered targeting systems).^{53,87-91}

The TTA-UC process is performed in a metal-organic bichromophore system consisting of an emitter (typically aromatic hydrocarbons) and a sensitizer (metallated macrocycles)⁹² as an energetically optimized pair. The process is based on the photophysical interplay of sensitizer and emitter molecules.⁹³ A schematic representation of the TTA-UC mechanism and the detailed energy transfer processes is shown in Figure 2.1.

The photon energy is absorbed by the sensitizer molecules (the red arrow, Figure 2.1) and stored in its long-lived triplet states, formed in the process of intersystem crossing (ISC) (Equations 2.1 and 2.2). However, the intramolecular transitions between states with different multiplicity are spin-forbidden. Nevertheless, the effect of the spin-orbit coupling allows for the coupling of a singlet state to a triplet state in the presence of a heavy metal atom. In the case of such heavy metals like palladium or platinum, the yield of the ISC approaches close to unity.⁹⁴ Thus, the use of organometallic compounds as sensitizer could significantly enhance the efficiency of the ISC.

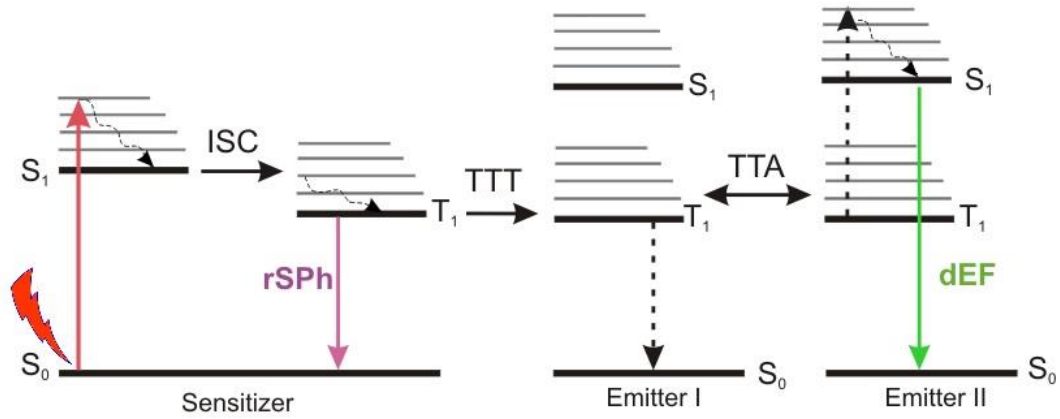
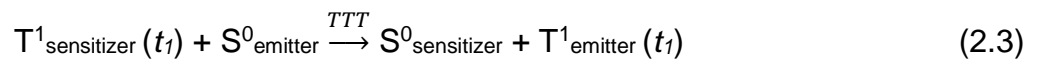


Figure 2.1 - Simplified energetic scheme of the TTA–UC process. The red arrow means excitation, green arrow – delayed emitter fluorescence (dEF), violet arrow – residual sensitizer phosphorescence (rSPh). ISC - intersystem crossing process, TTT - triplet-triplet energy transfer process, TTA - triplet-triplet annihilation process, S – singlet state, T – triplet state.

The depopulation channels for these sensitizer triplet states ($T^1_{\text{sensitizer}}$) include a radiative decay (rSPh, Figure 2.1 violet arrow), the non-radiative energy dissipation or the transfer of the energy to an emitter triplet state (T^1_{emitter}) by a Dexter-type, called triplet-triplet energy transfer process (TTT) (Equations 2.3 and 2.4).

Then two emitter molecules in their excited T^1_{emitter} interact and undergo inter-molecular triplet-triplet annihilation process (TTA). In results, one emitter molecule accumulates their triplet excited states energies to form higher singlet excited state (S^1_{emitter}), and the other molecule returns to its singlet ground state. Finally, the excited emitter singlet state decays radiatively back to the ground state by dEF (green arrow, Figure 2.1) bearing high energy photons (Equation 2.5).

All the energy transfer processes of TTA-UC can be described in the following equations:





where $h\nu_{dEF} > h\nu_{exc}$,

h is Planck's constant,

$h\nu_{exc}$ – frequency of excitation light,

$h\nu_{dEF}$ - frequency of emitted light,

the index (t_i) represents the triplet states created at the moments $t = t_i$, $i = 1, 2$ correspondingly.

2.2 Requirements for the TTA-UC

The process of TTA-UC is represented by a sequence of mutually complementary events: ISC, TTT, TTA, and consequent dEF. For the achievement of maximal efficiency of the TTA-UC process in total, the efficiency of each event in the sequence should be maximized.⁹⁵

The first requirement refers to the ISC process: there must exist a large difference between the ISC-coefficients of the sensitizer and the emitter molecules (Equation 2.6). The high ISC-coefficient of sensitizer molecules reflects an efficient population of the sensitizer triplet states via the single-photon absorption. In turn, a weak ISC-coefficient of the emitter reflects an absence of the emitter triplet states depopulation via phosphorescence and storage the energy for the consequent process of TTA.⁹⁶ This requirement can be summarized in the following inequality:

$$C_{\text{sensitizer}}^{ISC} \gg C_{\text{emitter}}^{ISC} \quad (2.6)$$

The efficiency of TTT from the sensitizer to the emitter depends on the overlap of their triplet manifolds (Equation 2.7).⁹⁷ Thereby the second requirement for the upconverting system is a maximal overlap of triplet energy levels:

$$E(T^1_{\text{sensitizer}}) \approx E(T^1_{\text{emitter}}) \quad (2.7)$$

The third requirement refers to the TTA process and maintains that the sum-energy of two emitter triplet states must be larger or equal energy to populate first excited singlet state of the emitter molecule:⁹⁶

$$2 \times E(T^1_{\text{emitter}}) \geq E(S^1_{\text{emitter}}) \quad (2.8)$$

The last requirement is related to the absorption spectra of the sensitizer. For reducing the chance of upconverting photons reabsorption, the generated emission should occur in a region of the spectrum free from the sensitizer and emitter ground state absorption.⁹⁶

In the case of an organic upconverting system that satisfies all above mentioned conditions and requirements, the TTA-UC process will occur with high efficiency. These criteria allow providing an effective approach for selecting an energetically optimized sensitizer and emitter combination for working in different regions of the spectrum.

2.3 Energy losses in the TTA-UC process

The theoretical maximum of a quantum yield for the TTA-UC system is equal to 50%.⁹⁸ The quantum yield describes how efficiently fluorophore converts the excitation light into luminescence and is defined as the ratio between the number of emitted photons $N(lum)$ and the number of absorbed photons $N(abs)$,⁹⁹ in turn in the TTA-UC process two absorbed photons maximally produce one emitted photon:

$$\eta = \frac{N(lum)}{N(abs)} \quad (2.9)$$

where η is a quantum yield of luminescence.

The classical definition is applicable only to a single molecular system.¹⁰⁰ Since the TTA-UC process consists of a connected chain of processes such as ISC, TTT, TTA, and the consequent emitter fluorescence, the resulting quantum yield incorporates the individual efficiency of each process and can be represented as a multiplication of the efficiencies of all participating processes:¹⁰¹

$$\eta_{UC} = \Phi_{ISC} \times \Phi_{TTT} \times \Phi_{TTA} \times \Phi_{dEF}, \quad (2.10)$$

where η_{UC} is the resulting quantum yield of TTA-UC,

Φ_{ISC} – the efficiency of the ISC process;

Φ_{TTT} – the efficiency of the TTT process;

Φ_{TTA} – the efficiency of the TTA process;

Φ_{dEF} – the quantum yield of the dEF.

However, an ideally high efficient, low-power and in-air TTA-UC has not been realized yet. All the internal energy conversion processes of the TTA-UC are accompanied by noticeable losses of the absorbed energy, and consequently, the upconversion emission has a frequency lower than the doubled frequency of the excitation.¹⁰² In order to design efficient upconversion systems, all possible loss mechanisms must be minimized or prevented.

There is a multitude of energy dissipation ways during TTA-UC, the main of them are caused by the following processes:¹⁰¹

- the internal conversion and vibrational relaxation of the excited singlet and triplet states;
- energy losses during the S^1 -to- T^1 ISC process of a sensitizer: the energy of sensitizer singlet state $E(S^1_{\text{sensitizer}})$ is higher than the energy of its triplet state $E(T^1_{\text{sensitizer}})$:

$$E(S^1_{\text{sensitizer}}) - E(T^1_{\text{sensitizer}}) > 0 \quad (2.11)$$

- energy losses during TTT process: an energy difference between the triplet states of sensitizer and emitter:

$$E(T^1_{\text{sensitizer}}) - E(T^1_{\text{emitter}}) \neq 0 \quad (2.12)$$

- energy losses during TTA process: doubled emitter triplet energy is significantly higher than emitter singlet state:

$$2 \times E(T^1_{\text{emitter}}) - E(S^1_{\text{emitter}}) \geq 0 \quad (2.13)$$

The minimization of the energy losses in the photon conversion processes occurs by the optimization of the energy structures of used sensitizer and emitter molecules.¹⁰³ However, the total amount of the energy losses during the TTA-UC is close to 1 eV.¹⁰¹

2.4 The sensitivity of the TTA-UC to environmental parameters

All intermolecular energy transfer processes in the TTA-UC have a strong dependence on a variety of environmental parameters, such as temperature or contamination with molecular oxygen.^{5,104} This sensitivity of the TTA-UC can successfully be used for different applications such as the building of oxygen and temperature biosensing tool.

2.4.1 Oxygen effect on the TTA-UC process

There are three forms of molecular oxygen. The triplet ground state of molecular oxygen $^3\text{O}_2$ ($^3\Sigma_g^-$) has an open-shell electronic configuration with two unpaired electrons and is paramagnetic, while the other two have no unpaired electrons and are both diamagnetic.^{104,105} The lowest-energy singlet excited state of molecular oxygen $^1\text{O}_2$ ($^1\Delta_g$) lies 94.3 kJ mol⁻¹ above the ground state and the second singlet state O_2 ($^1\Sigma_g^+$) is located 156 kJ mol⁻¹ higher in energy than the $^1\text{O}_2$ (Figure 2.2).¹⁰⁴

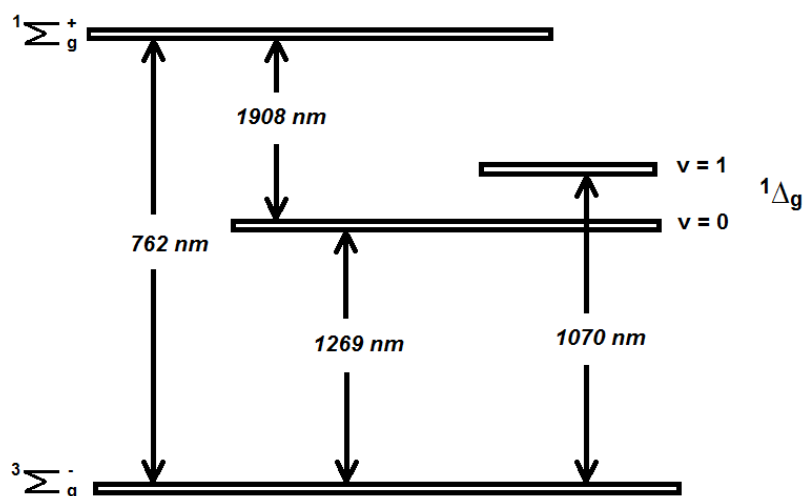


Figure 2.2 – Electronic states of molecular oxygen. Only two vibronic states $v = 0$ and $v = 1$ are mentioned.

With such a low excited state, $^3\text{O}_2$ can quench most triplet excited species through a Dexter mechanism energy transfer and populate the first singlet excited state $^1\text{O}_2$. Additionally, $^1\text{O}_2$ can easily interact with other species and affect the electronic structure resulting in the enhancement of the ISC from triplet excited state to singlet ground state.

In the TTA-UC practically all ongoing processes are associated with the triplet states of sensitizer and emitter molecules. A lifetime of the processes measures up tens or even hundreds of microseconds. This time is more than enough for the excited triplet states of sensitizer and emitter molecules to meet the molecular oxygen.¹⁰¹

It is well known that in the presence of molecular oxygen an active quenching process of the excited triplet states occurs. The quenching occurs by the transfer of excitation energy to the ground state of molecular oxygen. This is then followed by the generation of singlet oxygen ($^1\Delta_g$, Figure 2.2).^{5,105} The energy dissipation process also competes with emissive (phosphorescence) and non-emissive (triplet to triplet) energy transfer processes.¹⁰⁶ Singlet molecular oxygen has a long lifetime period since the return to its ground state is spin forbidden.

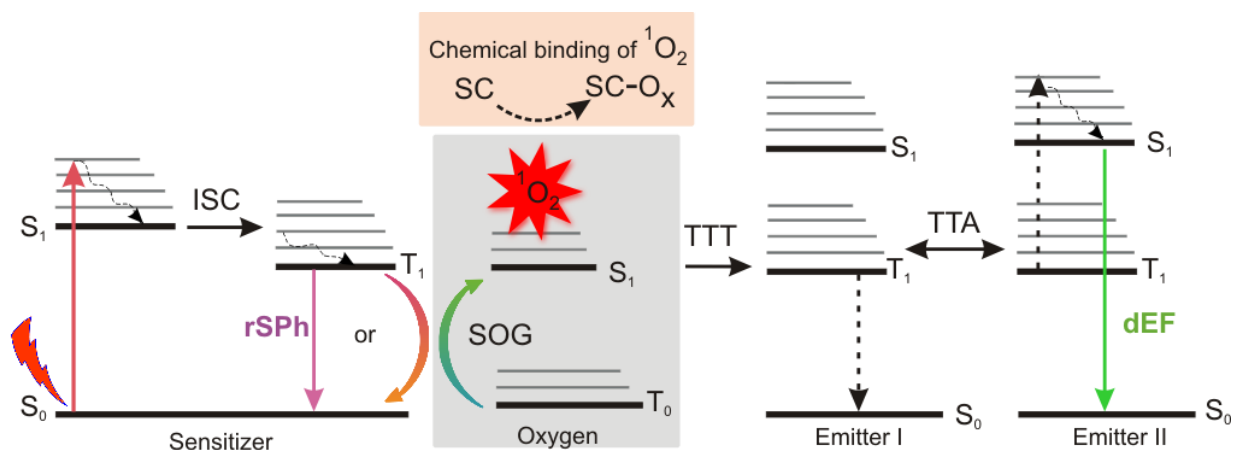


Figure 2.3 - Energetic scheme of the triplet-triplet annihilation upconversion process in an oxygen contaminated environment, containing singlet oxygen scavenging moieties (SC). SOG – singlet oxygen generation.

Singlet oxygen is a highly reactive species and a powerful oxidant, leading to the oxidation of the photoactive molecules and matrix, followed by dysfunction of UC systems or further loss of efficiency.¹⁰⁵ For the full exploitation of energy generated in the TTA-UC process, the oxygen protection is a crucial task because molecular oxygen readily quenches the triplet states of sensitizer and emitter. For the protection of organic ensembles, undergoing triplet-triplet annihilation, against oxygen deactivation various strategies such as reversible photoswitching, oxygen scavengers can be used. (Figure 2.3).^{5,105,107-108}

2.4.2 Temperature effect on the TTA-UC process

Electronic excited states of organic molecules are highly sensitive to their environment. Temperature changes strongly affect the luminescence characteristics of organic molecules. The changes are observed in the following optical parameters: an intensity of emission bands, band positions, shapes of spectra, or emission decays, lifetimes, and polarization.⁵³ The impact of temperature can modify one or many parameters of luminescence. These temperature-dependent influences arise from several processes, such as the changes in energy of electronic levels, the changes in refractive index, and other phenomena.⁵³

The most widely used scheme for the temperature measurements of luminescence in the actual practice, is one that is found for the determination of the ratio of emission intensities of different bands of luminescent material.⁵³ This temperature read-out scheme eliminates and compensates such measurement errors as an influence of measurement conditions on the emission intensity, fluctuations in excitation and instabilities in detection, concentration, or inhomogeneous distribution of the sensing material.

The TTA-UC process is one of the most suitable phenomena for the realization of luminescent thermometry applications. The emission intensity dependence of the dEF on temperature elevation shows a significant increase, while the rSPh shows a strong decrease. In contrast, reduction of the temperature drastically changes the behavior of the dEF and rSPh processes, the dEF- and rSPh-signals demonstrate decreasing and increasing emission intensities, respectively. This behavior allows us to create an unambiguous ratiometric temperature calibration curve.

The TTA-UC process demonstrates the temperature dependence because the TTT and TTA processes occur via molecular collisions. The processes are highly dependent on molecular diffusion, which in turn depends on the fluidity of the matrix containing the dyes.¹⁰⁹ For many materials, higher temperature leads to higher fluidity, and therefore to higher TTA-UC efficiency.¹¹⁰ However, the temperature-dependence of the TTA-UC could be also explained due to chemical phenomena such as dye aggregation. Counter-intuitively, it was recently shown that at lower temperatures, mixed aggregation of sensitizer and annihilator molecules in diluted conditions are resulted in higher TTA-UC efficiency.^{110, 111}

Upconverting dyes mostly attached or incorporated into organic or inorganic materials. The dyes, applicable for luminescent thermometry, should have the following properties: good thermal stability and photostability, an ability to undergo repeated excitation/emission cycles without luminescent efficiency losses.⁵³

Chapter 3: Stimuli-responsive protection of optically excited triplet ensembles against deactivation by molecular oxygen

The chapter is based on the paper N. V. Nazarova, Yu. S. Avlasevich, K. Landfester, S. Baluschev «Stimuli-responsive protection of optically excited triplet ensembles against deactivation by molecular oxygen» // Dalton Trans., 2018, 47, pp. 8605-8610.

This chapter provides detailed research of the sacrificial singlet oxygen scavenging ability of N-butyl-2-pyridone. N-butyl-2-pyridone ensures the effective external-stimuli responsive protection of excited triplet states against deactivation by singlet oxygen. The temperature is the acting external stimulus: lowering the temperature leads to a decrease in the concentration of singlet oxygen in the environment due to the activation of protection ability of N-butyl-2-pyridone. In contrast, at elevated temperatures singlet oxygen is not captured, and thus, the optically excited densely populated triplet ensembles are effectively depopulated. The singlet oxygen scavenging properties of the N-butyl-2-pyridone intensifies by the cooperative effect with a coordination solvent such as dimethylacetamide (DMAC). The cooperative effect of the components significantly enhances the long-term protection of the TTA-UC process against photooxidation.

3.1 Introduction

Many polycyclic aromatic hydrocarbons are able to bind singlet oxygen $^1\text{O}_2$ with the formation of the corresponding endoperoxides (EPs).¹¹² The discovery of reversible formation of organic EPs occurred in 1926 when Dufraisse and Moureu observed the reaction of covalent and reversible binding of oxygen by rubrene under light irradiation.¹¹³ The thermal decomposition of many EPs leads to the generation of molecular oxygen and the parent hydrocarbon.¹¹⁴ The ease of molecular oxygen release by EPs depends mainly on the nature of the polycyclic aromatic system and the type of substituents in the meso-positions.^{115,116} In 1967, Wasserman and Scheffer proved that a part of the evolved oxygen during thermolysis of 9, 10-diphenylanthracene endoperoxides is in the singlet excited state ($^1\Delta_g$) by the ability to transfer it to other photo-oxidizable substrates.¹¹⁵ Special attention is currently being paid to the formation of the organic EPs upon a reversible binding of oxygen with aromatic systems and to the development of highly

reversible photochromic systems as specific sources or traps of singlet oxygen for optical and photo-medical applications.¹¹⁷

In this study, the aromatic hydrocarbon N-alkyl-2-pyridone is considered as a potent strategy for stimuli-responsive protection of the excited triplet state ensembles against the deactivation by singlet oxygen. 2-Pyridone derivatives are especially interesting because the 2-pyridone structure is present in many compounds of natural origin. These structures are widely used for biomedical applications due to their facile synthesis and inherent polarity that enhances water solubility. The aromatic hydrocarbon easily bonds singlet oxygen to form EPs. The EPs formation process is strongly temperature dependent and thereby allows for keeping the singlet oxygen concentration in the upconverting ensemble at a certain level, co-regulated by the sample temperature.⁵

The integration of an upconversion system with EPO-forming moieties may allow us to create a new oxygen sensing technology.⁵ The sensing approach can be used as real-time control of the concentration of singlet oxygen, generated during the post-illumination period for the purpose of fractional photodynamic therapy.¹¹⁸ Since the TTA-UC process demonstrates the necessary sensitivity to oxygen and after the corresponding calibration, the TTA-UC can be used as such a sensing tool.

In the TTA-UC process, practically all ongoing processes are correlated with triplet states of sensitizer and emitter molecules. A lifetime of the processes is up to tens or even hundreds of microseconds. The analysis of molecular movement reveals that this time is enough for excited state deactivations by molecular oxygen, resulting in a loss of the carried energy and singlet oxygen generation.¹⁰¹ Contamination of an environment with molecular oxygen even on the ppm level dramatically influences the efficiency and aging properties of UC-samples. The effective oxygen protection strategies of organic ensembles, undergoing triplet-triplet annihilation, has been recently published in an extensive review.¹¹⁹

The development of highly sensitive tools for detecting physiologically relevant oxygen concentrations (ranging from nM – 200 μ M) has gained special attention for biosensing and medicine. The TTA-UC process represents a thorough solution to the problem of oxygen sensing: instead of a single material response on the acting parameter (variation of the oxygen concentration), the TTA-UC provides a ratiometric material response.⁵ The

use of the mutual dependence of the rSPh and dEF on the acting parameter ensures compensation of unwanted local changes in the sample parameters.^{120,121} Other advantages of the TTA-UC as a sensing technique are described in detail in Chapter 2. The application potential of the TTA-UC process ranges from the fields of molecular sensing¹²² and bioimaging,^{67,111,123-127} solid state optical technologies¹²⁸⁻¹³⁰ up to renewable energy sources.¹³¹⁻¹³⁵

3.2 Reversible binding of oxygen to aromatic compounds

The mechanism of the [4+2] cycloaddition of singlet oxygen to the electron-rich aromatic compounds is very similar to the classical Diels-Alder type reactions.⁵ The reactivity of aromatic hydrocarbons toward ¹O₂ increases with the electron density of the aromatic substrate, reflecting the electrophilic nature of ¹O₂.¹¹² Solvatochromic parameters of solvents such as dipolarity, polarizability, and Hildebrand solubility parameters, as well as steric effects, have a substantial effect on the kinetics of cycloaddition of singlet oxygen.^{112,136,137}

N-butyl-2-pyridone is capable to bind singlet oxygen dissolved in an organic solvent in a temperature dependent manner.⁵ 2-Pyridones have two tautomers: a lactam form for 2-pyridone and a lactim form for 2-hydroxypyridine.¹³⁸ 2-Pyridone tautomerizes by a proton transfer between the nitrogen and oxygen atoms.¹³⁹ The lactim form is mostly present in the solid phase and polar solvents, whereas lactim and lactam forms coexist in apolar solvents.^{138,140} The 2-pyridone can be stabilized by N-alkylation; a long alkyl chain in such compounds facilitates their miscibility with nonpolar organic solvents.⁵ N-Alkyl-2-pyridones represent a stable diene structure, which can undergo [4 + 2]-cycloaddition with different dienophiles, like alkenes¹⁴¹ or molecular oxygen in the singlet excited state.^{142,143} It is known that 2-pyridones bind singlet oxygen efficiently at lower temperatures and release it upon heating.^{5,142} Therefore, 2-pyridones were used for catalytic purposes,^{142,143} as well they exhibit pharmacological activities like anti-inflammatory, antimicrobial and antiviral agents.¹⁴⁴

The light irradiation of the toluene solution of porphyrin and N-butyl-2-pyridone leads to the simultaneous generation and trapping of singlet oxygen with the consequence of N-

butyl-2-pyridone EPOs formation. The reaction scheme is shown in Figure 3.1. This reaction is strongly temperature dependent; therefore, the endoperoxides decompose thermally and regenerate oxygen and the parent hydrocarbon. The lifetime of the EPO depends strongly on the temperature.¹¹⁵ At low temperature singlet oxygen can be stored for prolonged periods and can then be released by decomposition upon heating; thus the binding–release cycle can be repeated.⁵

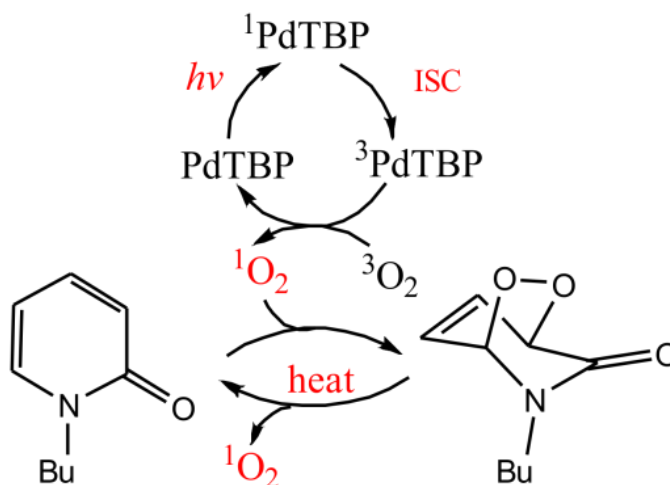


Figure 3.1 - Reversible addition of singlet oxygen to N-butyl-2-pyridone. PdTBP represents the ground state of the sensitizer; ¹PdTBP – the first excited singlet state of the sensitizer; ³PdTBP – the first excited triplet state of the sensitizer; *hν* – frequency of excitation light; ISC – Intersystem Crossing; ³O₂ – triplet ground state of molecular oxygen; ¹O₂ – singlet excited state of molecular oxygen. The figure is reproduced from ref. [7].

3.3 Experimental part

3.3.1 Materials

The sensitizer – meso-tetraphenyl-tetrabenzo[2,3]porphyrin palladium (II) (PdTBP)¹⁴⁴ and the emitter – 3,10-bis(3,3-dimethylbutyn-1-yl)perylene (BDP)¹⁴⁴ were synthesized as described elsewhere (Figure 3.2, 3.3). N-butyl-2-pyridone (Figure 3.4 (b)) was synthesized by alkylation of 2-hydroxypyridine with 1-bromobutane and purified *via* vacuum distillation.¹⁴⁵ All dyes employed in the experiment and N-butyl-2-pyridone were synthesized by Dr. Yuri Avlasevich. Commercially available DMAC (Figure 3.4 (a)) and toluene were purchased from Sigma-Aldrich.

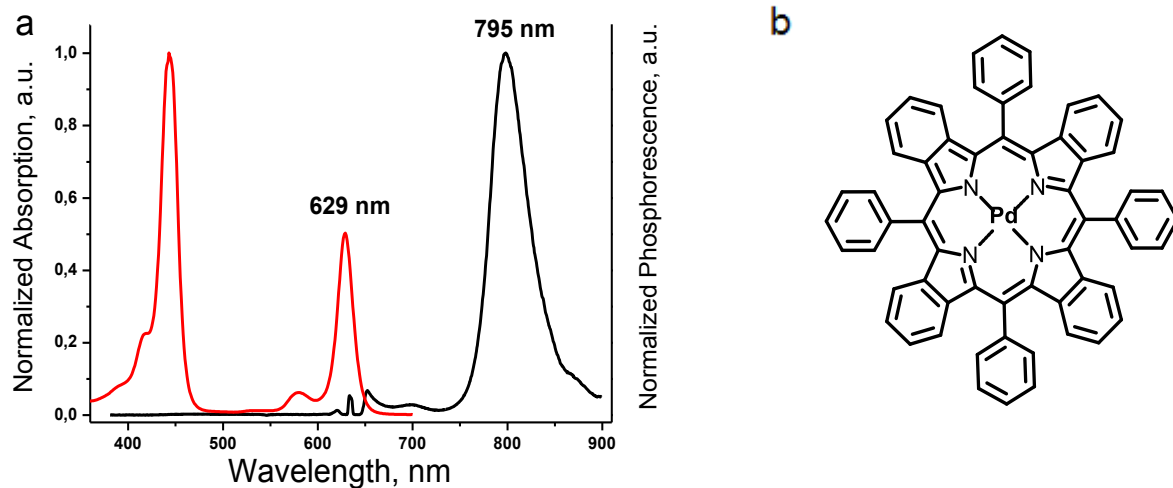


Figure 3.2 – (a) Absorption (red line) and phosphorescence (black line) spectra of PdTBP; (b) chemical structure of PdTBP.

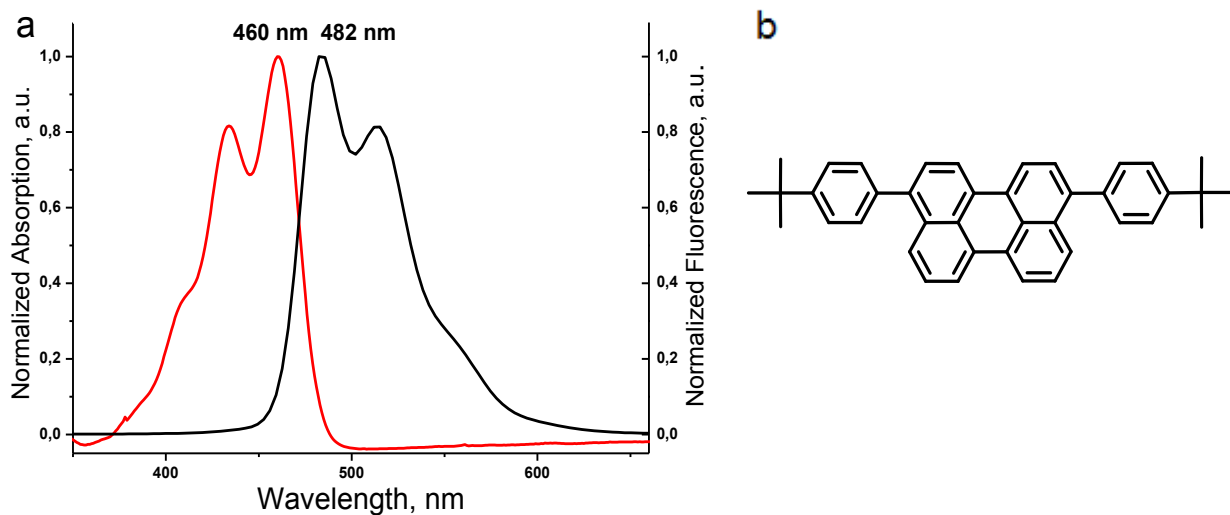


Figure 3.3 – (a) Absorption (red line) and fluorescence (black line) spectra of BDP; (b) chemical structure of BDP.



Figure 3.4 – Chemical structures of dimethylacetamide (a) and N-butyl-2-pyridone (b).

For oxygen-free measurements, the samples were prepared and sealed in an inert atmosphere glove-box. All solvents were purchased from commercial sources and were used as received. N-butyl-2-pyridone solution and DMAC were placed into glove-box atmosphere (4 ppm of O₂) and stirred in an open bottle for two hours; thus, the residual oxygen contamination at these solutions corresponds to the glove-box oxygen content. For all optical measurements, the molar concentrations of the sensitizer (PdTBP) and emitter (BDP) were the same, 1×10^{-5} M and 2×10^{-4} M, respectively.

3.3.2 Method

Luminescence spectra and kinetic data were recorded by created setup (Figure 3.5). The samples were excited with light beam of a wavelength of $\lambda_{\text{exc}} = 633$ nm using a HeNe laser. By using the system of dielectric mirrors (E02, Thorlabs Inc.), the excitation beam was directed to the sample and focused by an achromatic lens (focal distance 100 mm, the numerical aperture NA = 0.24).

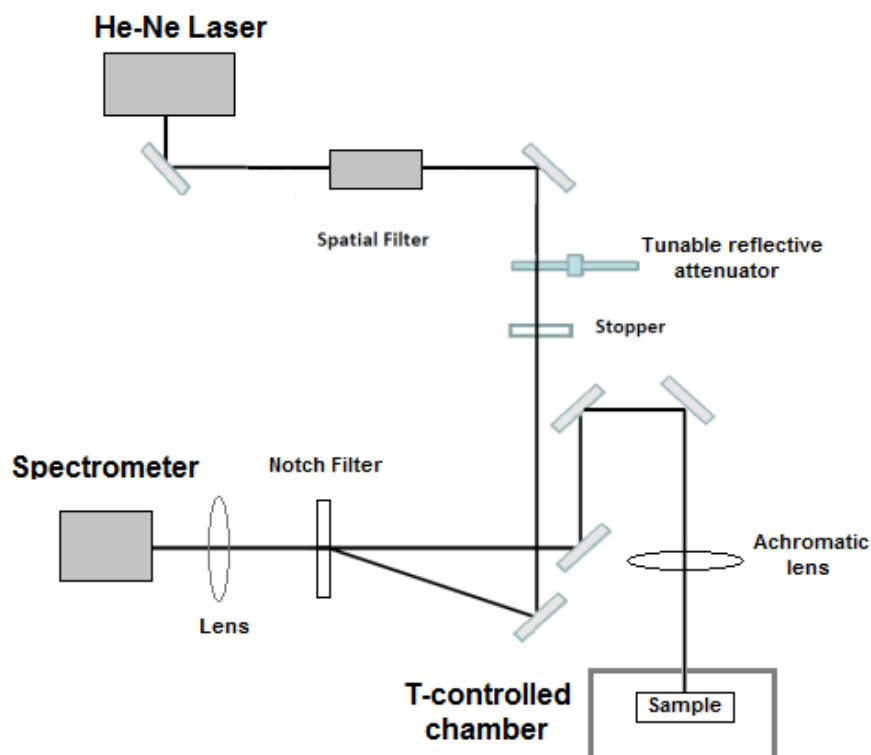


Figure 3.5 – Scheme of the experimental setup with a temperature controlled chamber.

Emission spectra were registered by a spectrometer (Hamamatsu Inc.). The excitation power was controlled by a power meter PM 100D (Thorlabs, USA). For regular measurements, the excitation intensity was set to 12 mW cm^{-2} , and the laser spot diameter was $d = 2 \times 10^{-3} \text{ m}$. The sample was located in the temperature-controlled chamber. The chamber temperature was controlled with the Peltier element by using the computer program from Electron Dynamics Ltd. (Southampton, UK). The sample temperature was additionally measured by the thermistor (PT100) attached on the top of the cuvette.

3.4 Results and discussion

3.4.1 N-butyl-2-pyridone effect on the TTA-UC process

As it was mentioned above, one of the methods of active protection of the densely populated triplet ensembles against deactivation by molecular oxygen is based on the use of so-called oxygen scavenging species. The scavenging species chemically reacts with singlet oxygen and trapped $^1\text{O}_2$. A distinct drawback of the deoxygenating method is the possible unwanted reactions between the singlet oxygen scavenging species and the UC-active moieties, and also an influence of the scavenging compounds on the UC-system overall. Therefore, the influence of N-butyl-2-pyridone on the efficiency of the TTA-UC process was studied primarily. The luminescence spectra of the studied UC-couple PdTBP / BDP in pure toluene and N-butyl-2-pyridone 20 vol.% / toluene 80 vol.% solution under glovebox conditions were compared (Figure 3.6). The temporal dependence of the dEF-signal at the fluorescence maximum ($\lambda = 521 \text{ nm}$) for pure toluene sample shows the typical behavior (Figure 3.6 (b), black line) for the UC-samples in an environment with residual oxygen contamination (4 ppm of O_2). The dEF-signal rises during the first 10 s of optical excitation, until the complete oxygen content is consumed (for instance, by oxidation of the BDP emitter molecule).⁵ In contrast, the UC-sample containing 20 vol.% N-butyl-2-pyridone demonstrates fast growth of UC-fluorescence because the concentration of the oxygen dissolved in the UC-sample is low (4 ppm of O_2), and oxygen can be effectively trapped by N-butyl-2-pyridone. As shown in Figure 3.6

(a), the dEF-signal in the solvent mixture containing 20 vol.% N-butyl-2-pyridone is slightly lower (about 15% less efficiency) than the dEF-signal of UC-sample in pure toluene.

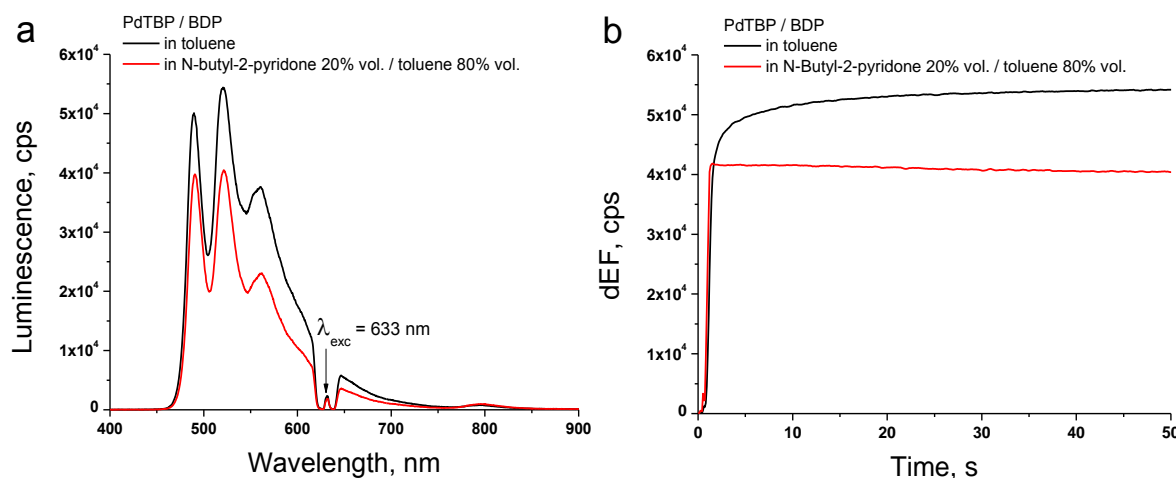


Figure 3.6 - (a) Luminescence spectra for the samples containing the UC-couple PdTBP / BDP, dissolved in pure toluene (black line) and in a mixture of N-butyl-2-pyridone 20 vol.% / toluene 80 vol.% (red line). (b) Temporal dependences of the dEF-signals at the fluorescence maximum ($\lambda = 521 \text{ nm}$). Experimental conditions: the samples were prepared and sealed in a nitrogen filled glovebox; $T = 25 \text{ }^\circ\text{C}$.

At glove box conditions, an increase of the concentration of N-butyl-2-pyridone in the UC-sample leads to a decrease of the dEF-signal (Figure 3.7). It can be explained by the reduction of the UC-sample fluidity. N-butyl-2-pyridone is a highly viscous liquid and has a significant effect on the rotational diffusion coefficient of UC-active moieties in the UC-sample. A change of viscosity even on a micro-level within the UC-system essentially influences the velocity of dye molecules rotation diffusion. In addition, a modification of the solvation shell of the interacting UC-compounds considerably influences the efficiency of the TTA-UC process. Thus, the efficiency of the TTA-UC process reflects any changes in the UC-system.

At ambient conditions, increasing the N-butyl-2-pyridone concentration in the UC-sample leads to a notable growth of the dEF efficiency (Figure 3.8). This means, that N-butyl-2-pyridone acts as a singlet oxygen scavenger with moderate characteristics. The significant decrease of the dEF-signal in the temporal kinetics can be explained as follows: the velocity of a generation of singlet oxygen is much higher, than the ability of the pyridone to attach oxygen.

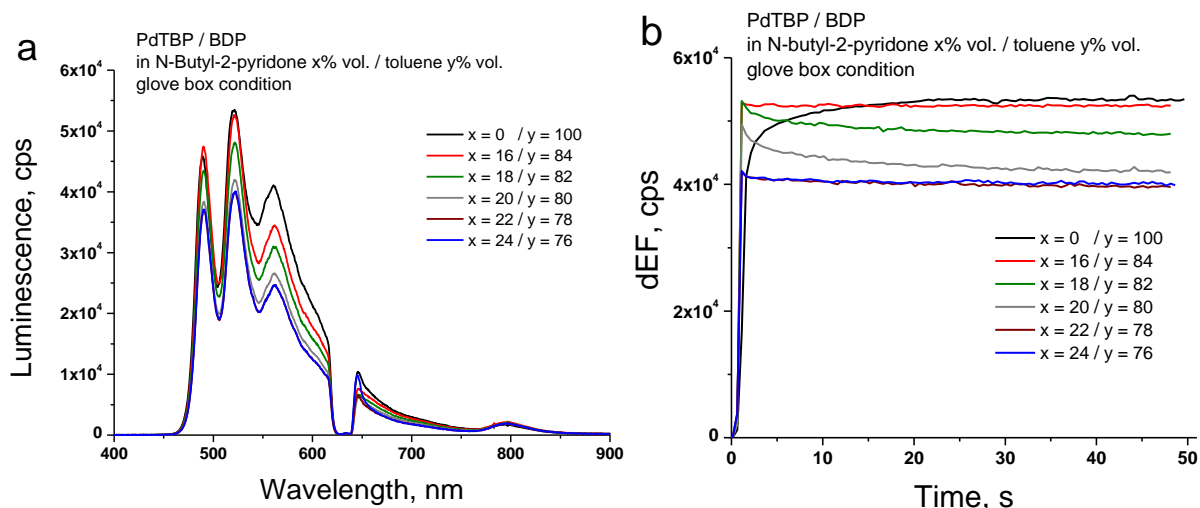


Figure 3.7 - (a) Luminescence spectra for the samples containing the UC-couple PdTBP / BDP, dissolved in pure toluene and in a mixture of N-butyl-2-pyridone / toluene in different ratio at glovebox conditions. The spectra were obtained at the moment $t = 50$ s. (b) Temporal dependences of the dEF-signal at the fluorescence maximum ($\lambda = 521$ nm). Experimental conditions: the samples were prepared and sealed in a nitrogen filled glovebox; $T = 25$ °C.

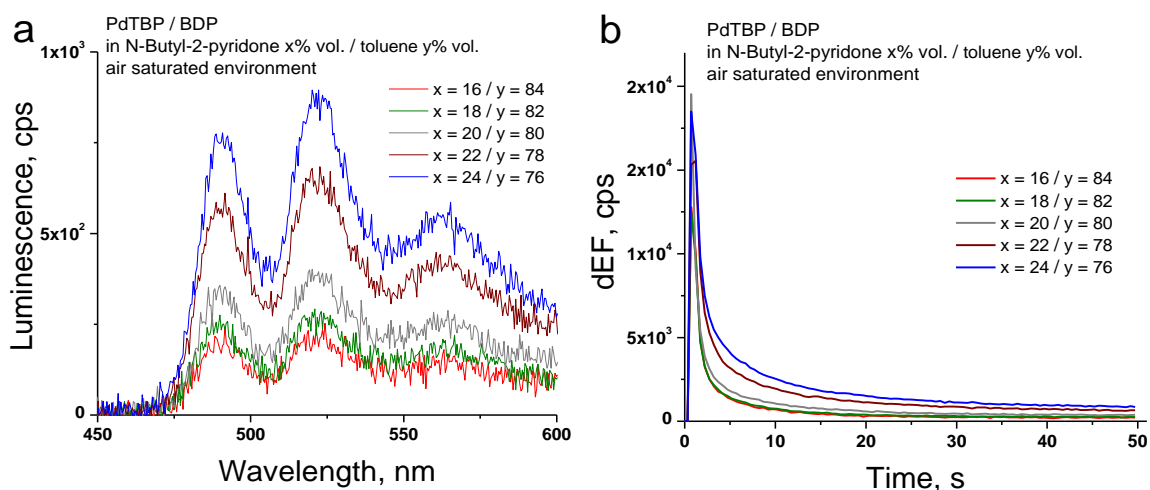


Figure 3.8 - (a) Luminescence spectra for the samples containing the UC-couple PdTBP / BDP, dissolved in a mixture of N-butyl-2-pyridone / toluene in the different ratio in an air saturated environment. The spectra were obtained at the moment $t = 50$ s. (b) Temporal dependences of the dEF-signal at the fluorescence maximum ($\lambda = 521$ nm). Experimental conditions: the samples were prepared and sealed in an air saturated environment; $T = 25$ °C.

3.4.2 Solvation shell tuning

The singlet oxygen scavenging ability of N-butyl-2-pyridone can be moderately enhanced by a cooperative effect with coordination solvents. DMAC is one of the coordination solvents that demonstrates a notable gain of long-term protection of excited triplet states against deactivation by singlet oxygen in combination with N-butyl-2-pyridone. A cooperative effect of the N-butyl-2-pyridone and DMAC visibly manifests the singlet oxygen scavenging properties in an air saturated environment (Figure 3.10). However, the cooperative effect of the components has no considerable influence on the efficiency of the TTA-UC process at glove box conditions (Figure 3.9). In turn, the addition of the coordination solvent DMAC to the UC-system dissolved in pure toluene at glove box conditions does not affect the strength of the dEF- (central peak, $\lambda = 521$ nm) and rSPh-signals (Figure 3.11) significantly.

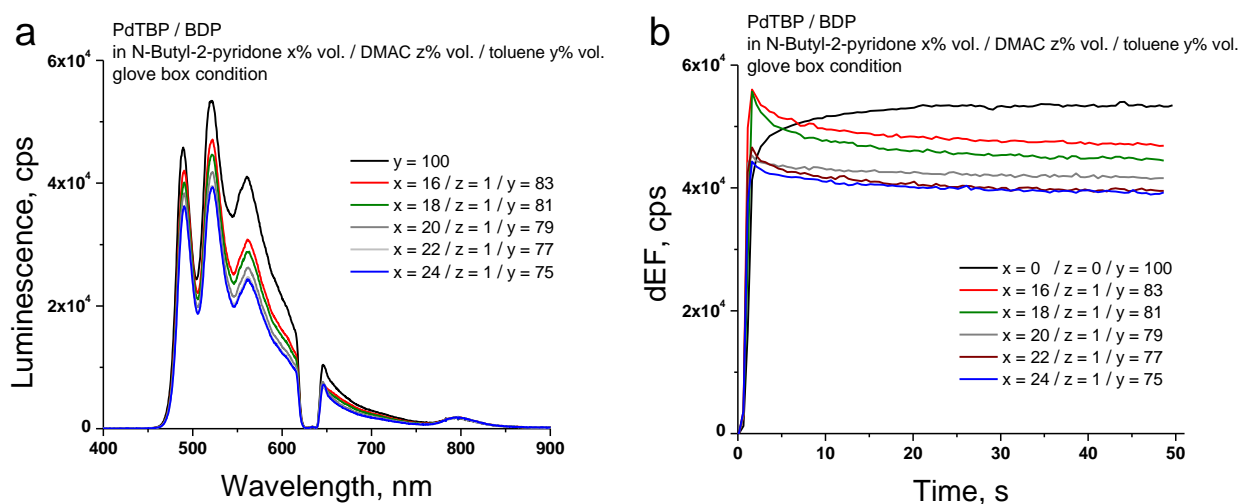


Figure 3.9 - (a) Luminescence spectra for the samples containing the UC-couple PdTBP / BDP, dissolved in a mixture of N-butyl-2-pyridone / DMAC / toluene in the different ratio in glovebox conditions. The spectra were obtained at the moment $t = 50$ s. (b) Temporal dependences of the dEF-signal at the fluorescence maximum ($\lambda = 521$ nm). Experimental conditions: the samples were prepared and sealed in a nitrogen filled glovebox; $T = 25$ °C.

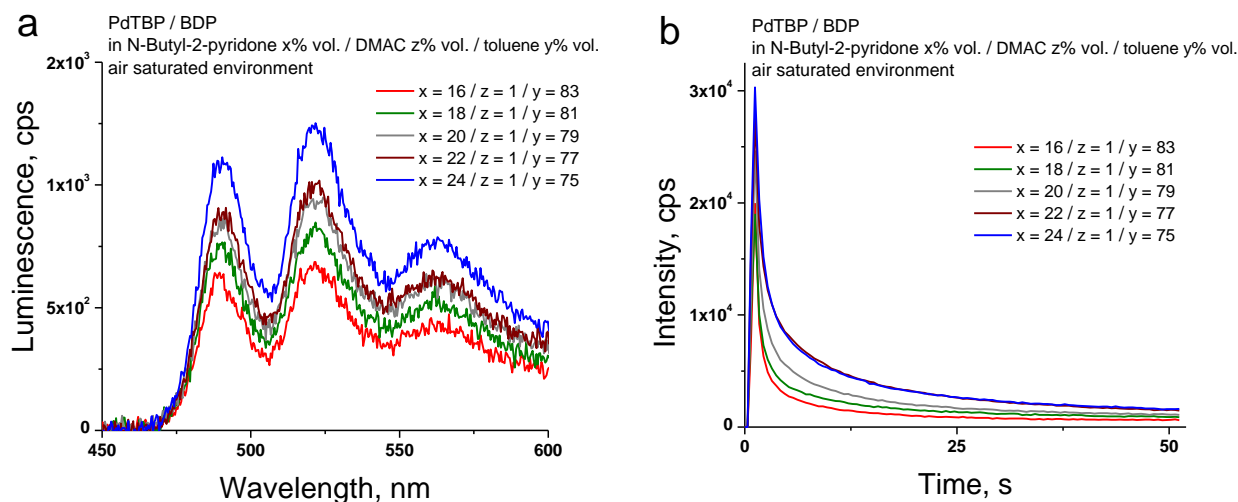


Figure 3.10 - (a) Luminescence spectra for the samples containing the UC-couple PdTBP / BDP, dissolved in a mixture of N-butyl-2-pyridone / DMAC / toluene in the different ratio in air saturated environment. The spectra were obtained at the moment $t = 50$ s. (b) Temporal dependences of the dEF-signal at the fluorescence maximum (at $\lambda = 521$ nm). Experimental conditions: the samples were prepared and sealed in an air saturated environment; $T = 25$ °C.

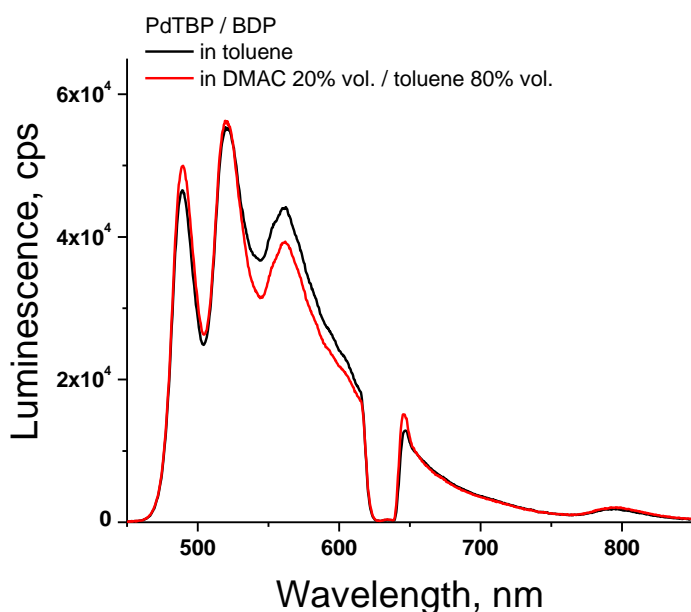


Figure 3.11 - Luminescence spectra for the samples containing the UC-couple PdTBP / BDP, dissolved in toluene and in a mixture of DMAC 20 vol.% / toluene 80 vol.% The spectra were obtained at the moment $t = 50$ s. Experimental conditions: the samples were prepared and sealed in a nitrogen filled glovebox; $T = 25$ °C.

The peak intensity dependence (at $\lambda = 521$ nm) of the generated dEF-signal on the amount of N-butyl-2-pyridone or N-butyl-2-pyridone in combination with DMAC clearly

shows the difference in the efficiency of the TTA-UC process in the presence or absence of the coordination solvent in the UC-sample (Figure 3.12). At an air saturated environment, the addition of the coordination solvent leads to a rise of the dEF efficiency; in contrary - at glove box conditions, the presence of DMAC leads to a decrease of the dEF-signal level.

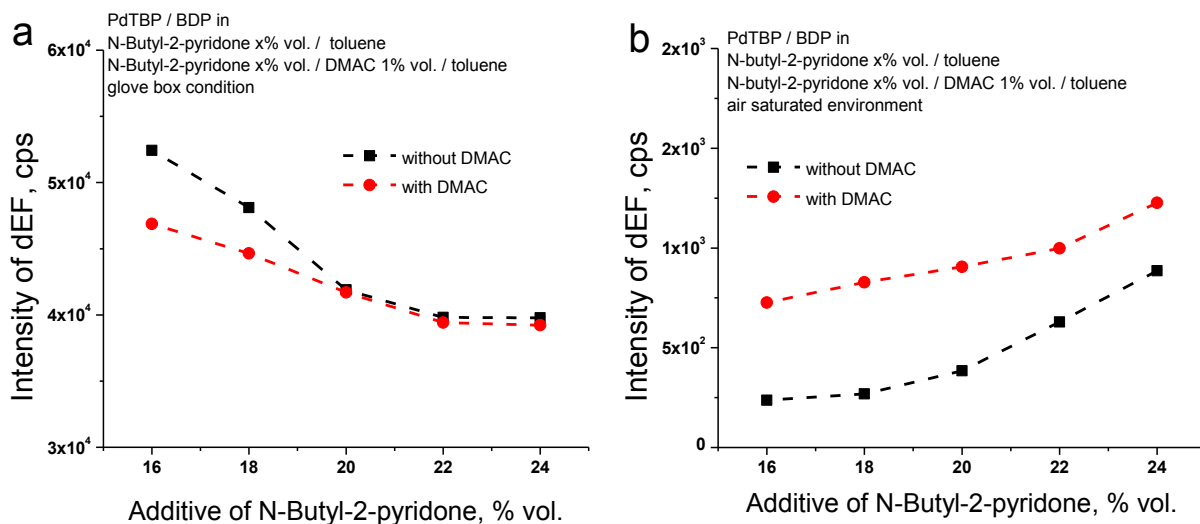


Figure 3.12 - Peak intensity (at $\lambda = 521$ nm) dependence of the generated dEF-signal on the amount of additive of N-butyl-2-pyridone or combination of N-butyl-2-pyridone with DMAC to the UC-sample in a glove box condition (a) and in an air saturated environment (b).

The efficiency of the TTA-UC process vastly depends on the microenvironmental conditions, that affects the mobility of the UC-compounds and the properties of their excited electronic states. DMAC is a dipolar aprotic solvent that does not act as a hydrogen-bond donor since C-H bonds are not sufficiently polarized.¹⁴⁶ However, DMAC is a good cation solvator due to the presence of lone electron pairs.¹⁴⁶ Perhaps, the positive effect of the combination of DMAC with N-butyl-2-pyridone on the efficiency of the TTA-UC process at ambient conditions is observed due to the improvement of the trapping mechanism of singlet oxygen by scavenging compound N-butyl-2-pyridone.

3.4.3 Temperature effect

The densely populated organic triplet ensemble participating in the TTA-UC process is created by optical excitation performed in the continuous-wave regime. In the

environment contaminated with molecular oxygen, an additional lost channel is present – it is the generation of singlet oxygen. The singlet oxygen generation leads to the loss of efficiency of both optical signals – the dEF (the emission with a central wavelength around 521 nm) as well the rSPh (the emission with a central wavelength around 796 nm) signal. The presence of N-butyl-2-pyridone in an UC-system leads to the appearance of the temperature dependence of the UC-system. The temperature-dependent manner of the system is caused by the temperature dependence of the photooxidation process of N-butyl-2-pyridone. The temperature dependences of the dEF and the rSPh for the UC-samples protected by N-butyl-2-pyridone are demonstrated in Figure 3.13. EPOs of N-butyl-2-pyridone are the chemical sources of singlet oxygen. The thermal decomposition of these EPOs leads to the regeneration of the parent N-butyl-2-pyridone and oxygen in a singlet state, with good chemical yields. The capacity of N-butyl-2-pyridone to bind singlet oxygen decreases with a rise in temperature of the sample. Even insignificant variations of the sample temperature are reflected in the intensity of dEF- and rSPh-signals.

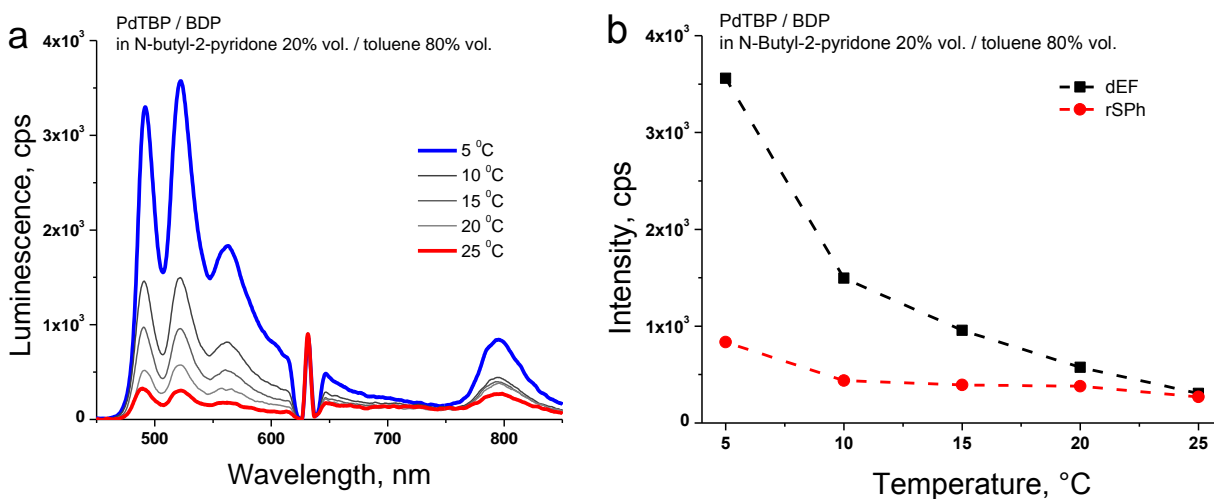


Figure 3.13 – (a) Dependence of the dEF and rSPh on the sample temperature. The UC-couple PdTBP / BDP, dissolved in a mixture of N-butyl-2-pyridone 20 vol.% / toluene 80 vol.% (b) Peak intensity dependence of generated dEF-signal (at $\lambda = 521$ nm) and rSPh-signal (at $\lambda = 796$ nm) on temperature. Experimental conditions: the sample was continuously illuminated; the luminescence spectra were obtained at the 100th second after the start. For each temperature measurement, a new sample point with a large lateral displacement was chosen.

Considerable changes were noticed in the UC-samples with the addition of N-butyl-2-pyridone (Figure 3.13) and N-butyl-2-pyridone combined with DMAC (Figure 3.14) upon the increase of the temperature from 5 °C to 25 °C. The intensity of the delayed fluorescence was increased by 12 and 34 times, and phosphorescence by 3.5 and 4 times, respectively.

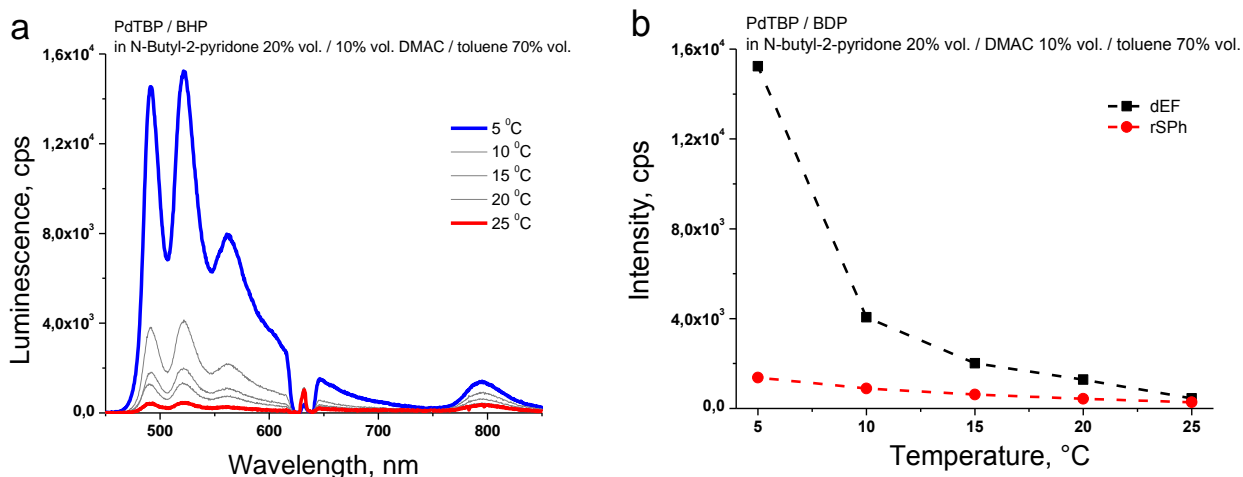


Figure 3.14 – (a) Dependence of the dEF and rSPh on the sample temperature. (b) Peak intensity dependence of generated dEF-signal (at $\lambda = 521$ nm) and rSPh-signal (at $\lambda = 796$ nm) on temperature. UC-couple PdTBP / BDP, dissolved in mixture of N-butyl-2-pyridone 20 vol.% / DMAC 10 vol.% / toluene 70 vol.% Experimental conditions: the same as in Figure 3.13.

The temporal dependences of the dEF- and rSPh-signals in an ambient environment for UC-samples protected by N-butyl-2-pyridone and N-butyl-2-pyridone combined with DMAC at different sample temperatures are shown in Figure 3.15 and 3.16. The results demonstrate that the ability of N-butyl-2-pyridone to bind singlet oxygen decreases with a rise in the sample temperature. It is also evident that the dEF is much more sensitive to the local oxygen concentration changes than the residual phosphorescence.

Figure 3.16 demonstrates that the singlet oxygen protection ability of N-butyl-2-pyridone is greatly intensified by the cooperative effect with DMAC. The temporal kinetics of dEF- and rSPh-signals initially shows the declined efficiency of the processes. Then the signals are gradually stabilized.

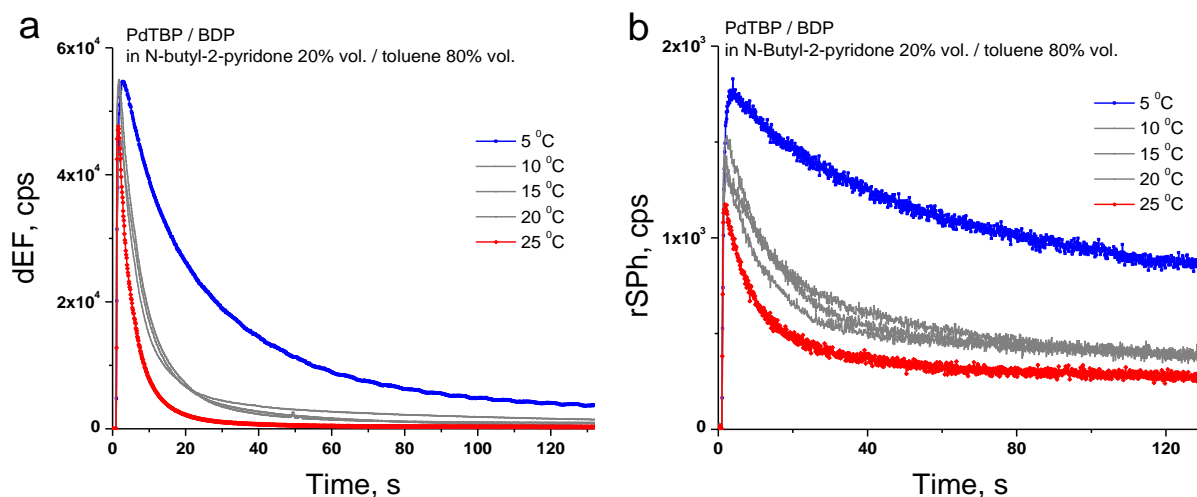


Figure 3.15 - (a) Temporal dependence of the dEF at the fluorescence maximum (at $\lambda = 521$ nm) for different sample temperatures. (b) Temporal dependence of the rSPH at the maximum (at $\lambda = 796$ nm) for different sample temperatures. UC-couple PdTBP / BDP, dissolved in mixture of N-butyl-2-pyridone 20 vol.% / toluene 80 vol.% Experimental conditions: the same as in Figure 3.13.

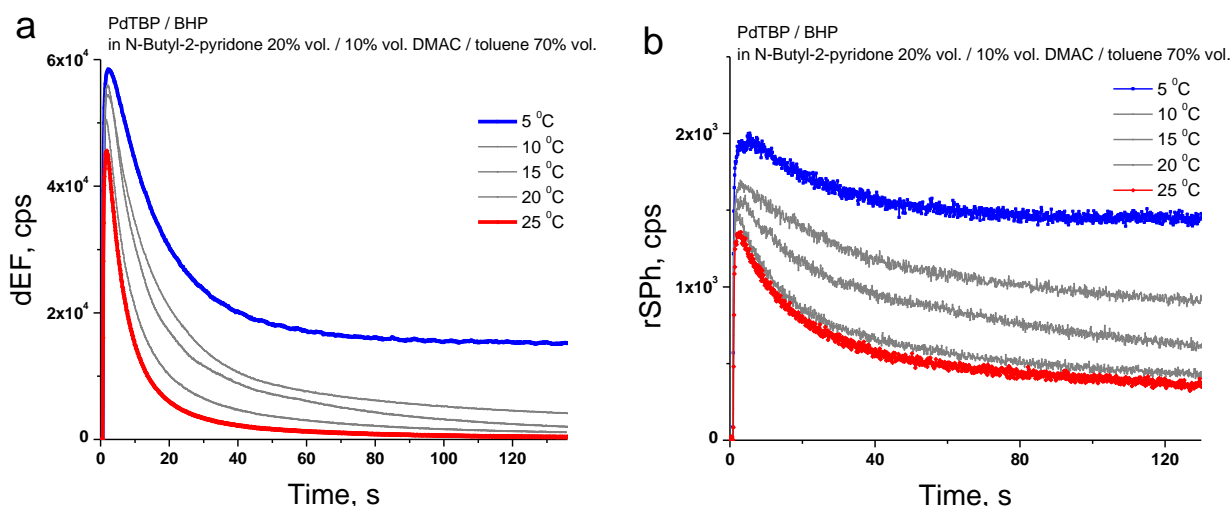


Figure 3.16 - (a) Temporal dependence of the dEF at the fluorescence maximum (at $\lambda = 521$ nm) for different sample temperatures. (b) Temporal dependence of the rSPH at the maximum (at $\lambda = 796$ nm) for different sample temperatures. UC-couple PdTBP / BDP, dissolved in mixture of N-butyl-2-pyridone 20 vol.% / DMAC 10 vol.% / toluene 70 vol.%. Experimental conditions are the same as in Figure 3.13.

N-butyl-2-pyridone demonstrates the constraint potential to bind large amounts of singlet oxygen. Figure 3.15 reveals the efficiency limitations of the N-butyl-2-pyridone as a sacrificial singlet oxygen scavenger. The total amount of bounded molecular oxygen can be estimated at least to 200 μM (saturation concentration of the oxygen in toluene), even

at a relatively large concentration (20 vol.%). Substantial increase of the UC-fluorescence is observed in the bulk sample after binding the present local amount of molecular oxygen (coinciding with an optically accessed spot). The optically accessed spot is an area of increased molecular oxygen diffusion (from the not excited regions). The newly arrived molecular oxygen will be non-binding. A gradual loss of efficiency is observed first for the UC-fluorescence then for the sensitizer residual phosphorescence.

3.5 Conclusions

For the first time the external-stimuli responsive sacrificial singlet oxygen scavenging properties of N-butyl-2-pyridone were demonstrated in this chapter. These properties ensure efficient temperature-dependent protection of densely populated excited triplet state ensembles against deactivation by singlet oxygen. N-butyl-2-pyridone is capable of binding $^1\text{O}_2$ dissolved in an organic solvent in a temperature-dependent manner: the lowering of the temperature leads to a decrease in the concentration of singlet oxygen in the environment, due to the activation of a protection ability of N-butyl-2-pyridone. In contrast, singlet oxygen will not be captured at elevated temperatures. Thus the optically excited densely populated triplet ensembles will be effectively depopulated. The use of N-butyl-2-pyridone also allows to regulate an additional acting parameter – the rate of bounding and releasing of molecular oxygen. Since the EPOs formation process is temperature dependent, the rate of molecular oxygen bounding or releasing is also temperature dependent. However, N-butyl-2-pyridone demonstrates the limited potential to bind large amounts of singlet oxygen.

Additionally, the singlet oxygen scavenging ability of N-butyl-2-pyridone was enhanced by the cooperative effect with a coordination solvent DMAC. The cooperative effect considerably promotes the long-term protection of the TTA-UC process against photooxidation.

Chapter 4: Optical temperature sensing in organogel matrices via annihilation upconversion

The chapter is based on the paper N. V. Nazarova, Yu. S. Avlasevich, K. Landfester, S. Balushev «All-optical Temperature Sensing in Organogel Matrices *via* Annihilation Upconversion», ChemPhotoChem, 2019, 1020-1026.

4.1 Introduction

Organogels are a great platform for constructing smart materials with a controlled response to external stimuli, e.g., such as temperature. The organogels are bicontinuous colloidal systems that form a three-dimensional network, where the compounds, sensitive to microenvironment changes, are well-dispersed. Upconverting organic dyes can be used as sensitive compounds. The temperature sensitivity of organogel is stimulated by high responsivity to stimuli of the TTA-UC process. The organogel represents a fully biocompatible soft matter matrix, namely a mixture of vegetable oil and organic wax in an appropriate ratio. The materials used for biosensing should be fully biocompatible, biodegradable, and should not have any toxic effects, including their waste compounds and intermediates.^{147,148}

A number of critical reviews have summarized the progress in biocompatible temperature (T) measurements. There is a broad consensus^{149,150} that optical methods for T -sensing are less invasive and able to provide the time-resolved and 2-dimensional spatial evolution of the T – distribution.¹⁵¹⁻¹⁵³ As an example of the vast amount of the works dealing with T -sensing in life-science objects, one can mention the systems using nanogels,¹⁵⁴ luminescent CdSe-CdS quantum dots as donors and cyanine dyes as acceptors,¹⁵⁵ dual-emitting nanoparticles,¹⁵⁶ and the fluorescence polarization anisotropy of green fluorescent proteins.¹⁵⁷ A common characteristic for these systems is that the ratiometric T -response is achieved, where the luminescence of one of the species does not depend on temperature, but the other strongly does.

The mostly used phenomenon for all-optical T -sensing is the phosphorescence decrease (or phosphorescence lifetime decrease) as a consequence of the increased temperature. Temperature is known to affect the phosphorescence quantum yield of a used dye, the

quenching constants, the solubility of oxygen, the diffusion of oxygen and finally, the temperature change facilitates singlet-triplet and triplet-singlet transitions.¹⁵¹

The molecular oxygen is a highly reactive species, that leads to quenching of the excited triplet states by the transfer of excitation energy to the ground state of molecular oxygen, followed by the generation of singlet oxygen. Thus the creation of an effective protection strategy against the quenching by molecular oxygen and protection against the subsequent production of highly reactive singlet oxygen is an imperative condition for the development of a T-sensing all-optical tool.^{105,158}

All these requirements are fulfilled when the TTA-UC process is performed in hydrophobic matrices such as blends of natural waxes and vegetable oils with pronounced singlet oxygen scavenging properties. Natural waxes are considered to be the most effective gelators for vegetable oils.¹⁵⁹ This approach ensures simultaneously the ability to tune the T-sensitivity towards biologically relevant temperature window (centered at $T = 36\text{ }^{\circ}\text{C}$), to use effectively singlet oxygen scavenging properties of the natural components and last, but not least to apply biocompatible materials (all used waxes and oils are approved as food additives). Moreover, the gels formed by the use of waxes have demonstrated very high thermal reversibility, i.e., no spontaneous phase separation was observed.

Singlet oxygen is generated continuously in the presence of molecular oxygen dissolved at the wax/oil sample during the optical excitation. The phytochemical compounds of the vegetable oils (for example, tocopherol, tocotrienol, and γ -oryzanol) demonstrate the remarkable activity of bounding all present amounts of singlet oxygen.¹⁶⁰⁻¹⁶³ Since the oxygen permeation rate through the surface of the sample is much lower than the rate of chemical binding of singlet oxygen, after a short initial period, the whole oxygen content is consumed.

4.2 Vegetable oils as singlet oxygen scavengers

Two types of oxygen can react with oils: triplet oxygen $^3\text{O}_2$ and singlet oxygen $^1\text{O}_2$. $^3\text{O}_2$ reacts with lipid radicals and causes autoxidation, which is a free radical chain reaction. Photosensitized oxidation of oils occurs in the presence of light, sensitizers, and atmospheric oxygen, in which $^1\text{O}_2$ is produced. The singlet oxygen readily reacts with the

compounds with high electron densities, such as the double bonds of unsaturated fatty acids.¹⁶² The reaction rate of singlet oxygen with lipids is much higher than that of triplet oxygen because $^1\text{O}_2$ can directly react with lipids, while $^3\text{O}_2$ reacts with the radical state of lipids. Oil oxidation is accelerated by temperature and light irradiation.

The free radical scavenging effect of oils depends on the type and concentration of antioxidants. Singlet oxygen quenching may occur by both physical and chemical quenching. The physical quenching mechanism involves the transfer of excitation energy of the singlet oxygen to ground state oxygen via a spin-orbit coupling or triplet energy transfer, herewith there is no oxidation of antioxidants. Amines, phenols, iodide, sulfides, and azides are physical quenchers. Antioxidant donates an electron to singlet oxygen in the chemical quenching. The reaction is involving the oxidation of an antioxidant. The quenchers of this type are ascorbic acid, amino acids such as histidine, cysteine, tryptophan and methionine, peptides, tocopherols.¹⁶³ Many of the antioxidants are able to quench singlet oxygen by both types of quenching.

Vegetable oils are rich sources of natural antioxidants that can be used as free radical scavengers. Argan oil (AO), peanut (PO) and rice bran oils (RBO) are antioxidant-rich natural products, now applied both in cosmetics and food grades. These vegetable oils show antiproliferative, antidiabetic, and cardiovascular risk-preventive effects.¹⁶⁴ Their effective antioxidative components include tocopherols (AO: 0.637;¹⁶⁵ PO: 0.226;¹⁶⁶ RBO: 0.297 $\text{mg}\cdot\text{g}^{-1}$;¹⁶⁷), phenolic compounds (AO: 3269.00;¹⁶⁵ PO: no phenolic compounds were detected in cold-pressed peanut oil;¹⁶⁸ RBO: 3.59 $\text{mg}\cdot\text{g}^{-1}$; ¹⁶⁹), plant sterols (AO: 2.95;¹⁶⁵ PO: 4.34;¹⁶⁸ RBO: 8.58 $\text{mg}\cdot\text{g}^{-1}$;¹⁷⁰), γ -oryzanol (only RBO: 3.0 $\text{mg}\cdot\text{g}^{-1}$;¹⁷⁰) and squalene (AO: 3.17; ¹⁷¹ PO: 0.13;¹⁷² RBO: 8.33 $\text{mg}\cdot\text{g}^{-1}$;¹⁷³).

The absolute viscosity of the vegetable oils is decreased by increasing temperature.¹⁶⁵ The RBO (0.0593 Pa·s at 26 °C) is the most viscous oil followed closely by PO (0.0593 Pa·s at 26 °C) and AO among the vegetable oils.¹⁷⁴ The same trend is also observed at other temperatures.

Antioxidant components of vegetable oils in UC-samples ensure stable protection of the excited triplet state against the deactivation by singlet oxygen (Figure 4.1). The luminescence spectra of PdTBP / BDP in a mixture of vegetable oils and toluene in the equal ratio (50 wt.% vegetable oil / 50 wt.% toluene) show a slight difference in the

efficiency of the TTA-UC process. The level of dEF-signal for the UC-sample with PO in the composition by 6% and 13% is higher than for UC-samples with RBO and AO, respectively. The efficiency of the TTA-UC process accrues the first 10 to 15 s and then stabilizes. The dEF-signals of the UC-samples with PO and AO demonstrate stable temporal kinetics, whereas the stability of the UC-sample with RBO shows a slight decrease of efficiency by 6% in the first 4 min of kinetic registration, then the dEF-signal also stabilizes (Figure 4.1(b)).

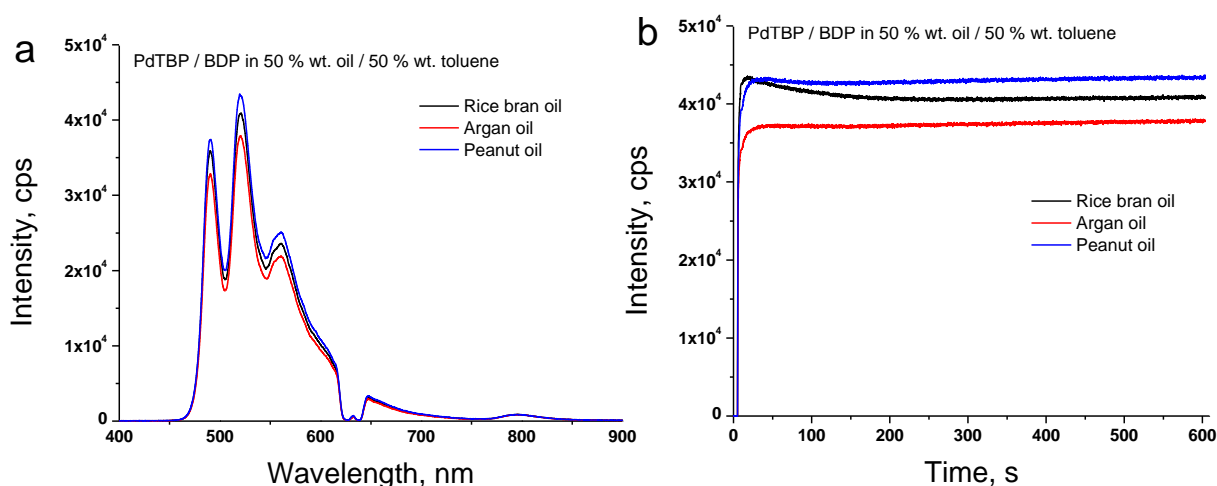


Figure 4.1 - (a) Luminescence spectra for the UC-Systems: PdTBP / BDP in 50 wt.% vegetable oil / 50 wt.% toluene. Oils: RBO, AO, and PO. The spectra are obtained at the $t = 600$ s. (b) Temporal dependence at the maximum of dEF-signal (at $\lambda = 521$ nm). An air saturated environment.

4.3 Natural waxes as a temperature dependent matrix

Waxes are complex mixtures of several nonpolar and polar components. The majority of components are hydrocarbons, wax esters, fatty acids, and fatty alcohols with varying carbon chain lengths (Figure 4.2).¹⁵⁹ Natural waxes are considered to be the most promising ones among the various gelators explored for gelling vegetable oils because of their excellent oil binding properties.¹⁶⁵ Moreover, the gels formed by using waxes have thermo-reversibility property.

Beeswax is an insect wax and a composition of esters. Beeswax consists mainly of myricyl palmitate plus saturated and unsaturated hydrocarbons and organic acids. Carnauba wax is a plant origin wax and composed of a mixture of straight-chain esters, alcohols, acids, and hydrocarbons.¹⁷⁵ Beeswax has a lower carbon chain length than carnauba wax. Beeswax is characterized by lower melting temperature ($T = 61 - 63\text{ }^{\circ}\text{C}$) and lower viscosity compared to carnauba wax ($T = 80 - 82\text{ }^{\circ}\text{C}$).¹⁷⁵ The softening of beeswax starts already at about $35\text{ }^{\circ}\text{C}$. Carnauba wax shows the beginning of softening only at about $55\text{ }^{\circ}\text{C}$ in contrast to beeswax. But most of the composition melts even at much higher temperatures.¹⁷²

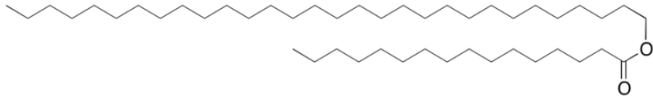
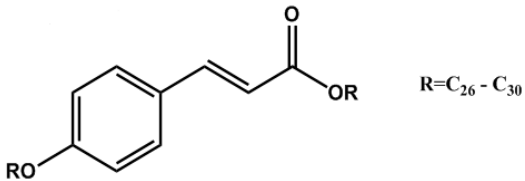
	Composition	Main ingredient structure
Beeswax	Monoesters 35% Hydrocarbons 14% Diesters 14% Triesters 3% Hydroxy monoesters 4% Hydroxy polyesters 8% Acid esters 1% Acid polyesters 2% Free fatty acids 12% Free fatty alcohols 1%	
Carnauba wax	Aliphatic esters 40% Diesters of 4-hydroxy-cinnamic acid 21.0% ω -Hydroxycarboxylic acids 13.0% Fatty alcohols 12% Predominantly derived from acids and alcohols in the C26-C30 range	

Figure 4.2 - Composition of the natural waxes and chemical structure of main ingredients.

Like other materials, waxes expand when subjected to a rise in temperature and contract as the temperature is decreased. Carnauba wax has a linear thermal expansion between

22 °C and 52 °C, while beeswax has at least two rates of expansion over this temperature range. The coefficient of thermal expansion of carnauba wax ($k = 156 \pm 10 \times 10^{-6} / ^\circ\text{C}$ between 22 °C and 52 °C) is smaller, than for beeswax ($k = 344 \pm 31 \times 10^{-6} / ^\circ\text{C}$ between 22 °C and 41.2 ± 1.2 °C and $k = 1048 \pm 170 \times 10^{-6} / ^\circ\text{C}$ between 41.2 and 50 ± 1.2 °C).¹⁶³ It is interesting to note that beeswax has shown an increase in the rate of expansion at 37.5 °C and a decreased rate of expansion at 45 °C.¹⁷⁵

Hydrogen bonding between molecules in a wax-oil network is weakened by heating. It leads to the changes in the intermolecular interactions between the upconverting dyes and matrix environment in the organogel. As a result, the efficiency of the TTA-UC strongly depends on the organogel temperature.

4.4 Ratiometric temperature sensing

The most commonly used temperature sensing scheme in luminescence thermometry is based on the determination of the ratio of intensities of different emission bands of luminescent material. The temperature sensing method, performed in a bio-compatible organogel matrix, is elucidated in Figure 4.3. This ratiometric-type sensing technique is based on a dual-signal response of the TTA-UC system embedded in the organogel matrix: the dEF (Figure 4.3 (a), emission spectra around central wavelength of $\lambda = 521$ nm) and rSPh (Figure 4.3 (a), emission spectra around central wavelength of $\lambda = 796$ nm). The ratio between the maximal intensity of dEF $I_{\text{max}}(\text{dEF})$ and the maximal intensity of rSPh $I_{\text{max}}(\text{rSPh})$ signals (Figure 4.3 (c)) is used for the ratiometric temperature sensitivity of UC-organogel matrix measurements. This technique is called the ratiometric intensity method. Then the ratio is normalized regarding to the ratio $I_{\text{max}}(\text{dEF}) / I_{\text{max}}(\text{rSPh})$ at the starting temperature (Figure 4.3 (d)). In this way, it is possible to create a non-ambiguous calibration curve, that connects the ratio of the integral dEF / rSPh and the sample temperature.

With an increase in the temperature of the hydrophobic matrix containing the TTA-UC system, the maximum emission of the dEF decreases and simultaneously the maximum emission of the rSPh increases (Figure 4.3 (a)). This optical behavior of the emission

intensities ensures a stable and simple registration system because no additional filters are necessary.

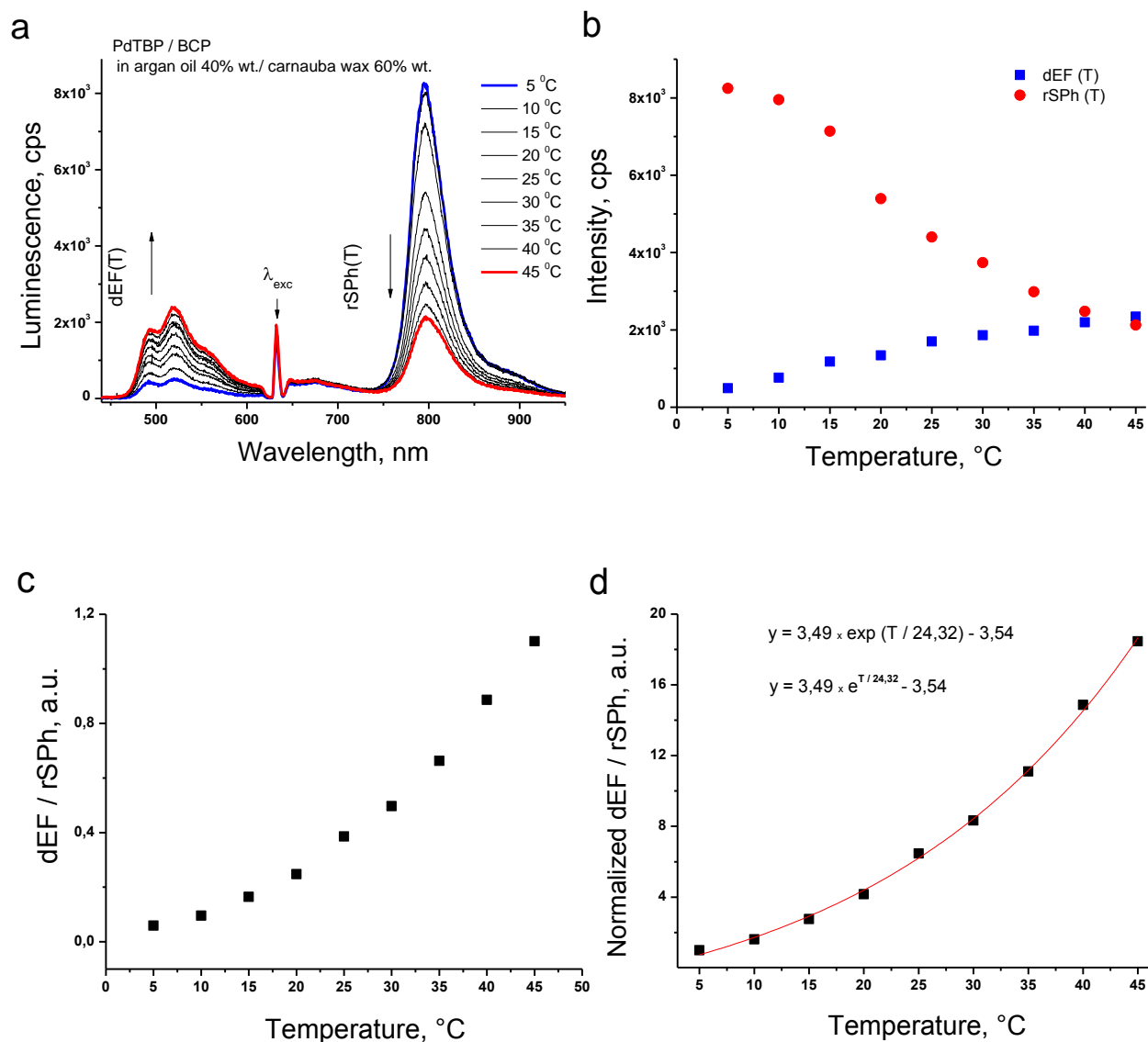


Figure 4.3 - Procedure allowing all-optical and ratiometric local temperature sensing via biocompatible organogel-based TTA-UC system. (a) Luminescence spectra of the studied TTA-UC system consisting of PdTBP (1×10^{-5} M) / BCP (2×10^{-4} M) in argan oil 40 wt.% / carnauba wax 60 wt.% (b) Temperature dependence of the signals of $I_{max}(dEF)$ (blue squares) and $I_{max}(rSPh)$ (red circles). (c) Dependence of the ratio $I_{max}(dEF) / I_{max}(rSPh)$ on local temperature. (d) Normalization of the ratio $I_{max}(dEF) / I_{max}(rSPh)$ regarding the value for $T = 5$ °C. The red curve is the exponential fit of the experimental points.

The spectral shape of the dEF-signal and the spectral shape of the rSPh-signal is not changed with the change of the sample temperature. Therefore, the maximal fluorescence intensity at a certain wavelength instead of the integral delayed fluorescence of the emitter was used in this study. The maximal phosphorescence intensity at a certain wavelength was used instead of the integral residual phosphorescence of the sensitizer.

An quasi oxygen-free operation of the TTA-UC system could be achieved even if the sample is placed and kept in an ambient environment (oxygen content > 20 vol.% O₂). This condition is met if the diffusion rate of the molecular oxygen, dissolved at the hydrophobic matrix throughout the borders of the optically assessed spot, is much slower than the rate of chemical bonding of the singlet oxygen inside this optical spot. The temporal dependences of the intensity of the optical signals of dEF (blue line) and rSPh (red line) for constant excitation intensity of $I_{exc} = 20 \text{ mW cm}^{-2}$ are demonstrated in Figure 4.4. The optical excitation begins at $t_1 = 5 \text{ s}$. It is evident, that at $t_2 = 20 \text{ s}$ the signals of dEF and rSPh are stable enough. The concentration of unbounded molecular oxygen is very low across the excitation spot. Therefore, the signals of dEF and rSPh are not significantly changed and can be used further as a measure for the local temperature.

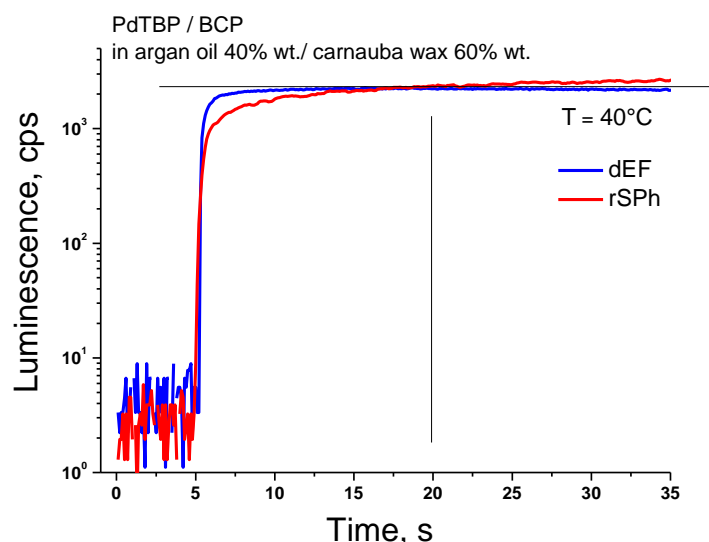


Figure 4.4 - Temporal dependences of dEF (blue line) and rSPh (red line) signals intensities for the TTA-UC system, presented in Figure 4.3. The experimental conditions for all the measurements: constant intensity of $I_{exc} = 20 \text{ mW cm}^{-2}$; excitation wavelength $\lambda = 633 \text{ nm}$; an ambient environment; $T = 40 \text{ }^\circ\text{C}$.

4.5 Experimental part

4.5.1 Materials

The sensitizer meso-tetraphenyl-tetrabenzoporphyrin palladium (II) (PdTBP) and the emitters - 3,10-bis(3,3-dimethylbutyn1-yl) perylene (BDP), 3,9(10)-bis(3,5-dimethoxyphenyl) perylene (BMP) and 3,4,9,10-tetra(butoxycarbonyl) perylene (BCP) were used as energetically optimized upconversion dye pairs. All employed in this experiment dyes were synthesized by Dr. Yuri Avlasevich. The chemical structures, absorption and emission spectra of all molecules are shown in Figure 4.5, 3.2, and 3.3 (Chapter 3). The chosen emitter molecules demonstrate almost identical fluorescence maxima ($\lambda = 482$ nm for BDP; $\lambda = 486$ nm for BMP, and $\lambda = 489$ nm for BCP). This fact minimizes the dependence of the process of TTA-UC on the energy position of the emitter singlet state. The molar concentration of sensitizer is fixed to 1×10^{-5} M and the emitters - 2×10^{-4} M, kept the same for the entire optimization process. As seen in Figure 4.5, 3.2, and 3.3 (Chapter 3), the absorption and emission spectra of the chosen emitter molecules are slightly different. Therefore, it is expected that also the corresponding excited triplet states will have small differences.

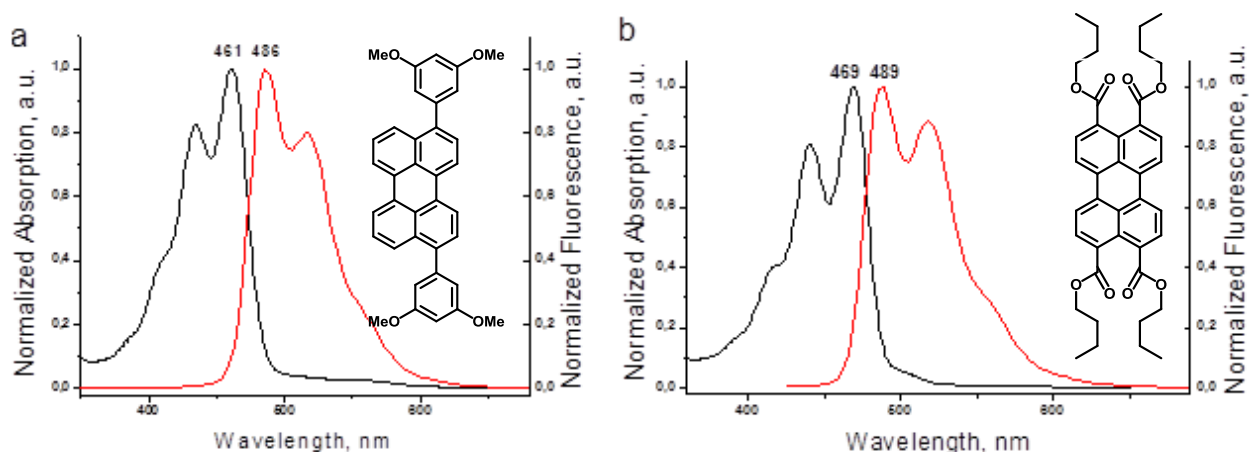


Figure 4.5 - Absorption (black line) and fluorescence (red line) spectra of emitters BMP and BCP. Insets: chemical structures of the emitters (a) BMP and (b) BCP.

Two natural waxes – beeswax and carnauba wax were chosen as matrix materials that allows a significant increase of the molecular rotational diffusion of the optically active molecules for a temperature interval centered at 36 °C (Figure 4.2). Both waxes are biocompatible and defined as food additives: E901 and E903, correspondingly. Carnauba

wax was purchased from Acros Organics (USA), and beeswax – from Carl Roth (Carl Roth GmbH, Germany).

Natural oils – rice bran oil, argan seed oil and peanut oil were applied as emollients. The main reason for using the emollients is a controllable lowering of the melting point of the mixture of natural wax / vegetable oil. Additionally, the organic oils are reported as an excellent sacrificial scavenger of singlet oxygen. RBO was purchased from TEA Natura (TEA Prodotti Naturali di Manzotti P., Italy), AO – from Primavera (Alnatura, Germany) and PO – from Braendle (P. Braendle GmbH, Germany).

Amphiphilic substances poly(ethylene glycol) methyl ether (OMe-PEG₃₅₀), polyethylene glycol p-(1,1,3,3-tetramethylbutyl)-phenyl ether (TX-100), L- α -Lecithin (lecithin), and glycerol were tested as promoters of the sensitivity of the TTA-UC process to small sample temperature changes. Their chemical structures are shown in Figure 4.6.

OMe-PEG ₃₅₀	
TX-100	
Glycerol	
Lecithin	

Figure 4.6 – Chemical structures of the amphiphilic additives OMe-PEG₃₅₀, TX-100, glycerol and lecithin.

4.5.2 Method

Luminescence spectra and kinetics were recorded by the experimental setup (Figure 3.5, Chapter 3). The setup is comprised of light source - HeNe laser ($\lambda_{\text{exc}} = 633 \text{ nm}$), optical components (filters, mirrors, lenses), sample chamber with controlled temperature, sample holder, temperature controller, reference thermometer, and detector. The excitation power was controlled by using power meter PM 100D (Thorlabs, USA). The excitation intensity was set to 10 mW cm^{-2} , laser spot diameter was $d = 1 \times 10^{-3} \text{ m}$.

A photograph of the sample chamber with controlled temperature is shown in Figure 4.7. The temperature in chamber is controlled with the Peltier element using computer program from Electron Dynamics Ltd. (Southampton, UK) and recirculation chiller. The sample temperature additionally is controlled by the thermistor (PT100) attached on the top of the sample.

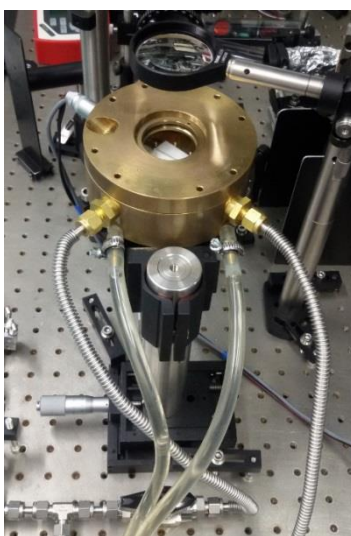


Figure 4.7 – Sample chamber with controlled temperature.

4.5.3 Sample preparation

Toluene solutions of the sensitizer (10^{-4} M , $100 \mu\text{L}$) and emitter (10^{-3} M , $200 \mu\text{L}$) were mixed at room temperature in a 25 mL round-bottom flask, and the solvent was evaporated to dryness under vacuum ($40 \text{ }^\circ\text{C}$, 74 mbar). The residue was dissolved in vegetable oil ($200 / 400 / 500 / 600 / 800 \text{ mg}$) and added to molten wax ($800 / 600 / 500 /$

400 / 200 mg) in appropriate ratio, mixed at 100 °C to form a homogeneous mixture. The samples were placed in the glass tubes (VITROTUBES™, Hollow Rectangle Capillaries - N2540-50) with the thickness of 400±10 µm and sealed with epoxy.

A controlled amount of additives was added to an UC-dyes solution in oil for the preparation of organogels containing the amphiphilic additives. It was carefully stirred and natural wax was added. The resulting mixture was mixed at 100 °C to form a homogeneous mixture. The samples were placed in the glass tubes for further measurements.

4.6 Results and discussion

4.6.1 Organogel matrices containing emitter molecules with different amphiphilicity

The mobility of the dye molecules, that are dispersed in the organogel matrix, depends significantly on viscosity of the matrix environment and the dye-matrix interactions (the rotational diffusion of the dye molecules). The amphiphilicity of the emitter molecules was altered as the first optimization parameter of the organogel matrix. The series of emitter molecules with different amphiphilicity was tested. The modifications of dyes structures substantially influence on the interplay between dye molecules and wax-oil matrix environment. The optical response of the UC-pairs containing the next emitter molecules BDP, BMP, and BCP (Figure 4.8) was studied. The emitters had different hydrophobicity, and they were posted in the order of hydrophobicity decreasing.

The temperature dependences of the normalized ratio of dEF / rSPh for investigating the UC-systems with different compositions are shown in Figure 4.8. Two parameters, namely the amphiphilicity of emitter molecules together with the wax-type, were varied simultaneously. The emitter BCP with the lowest hydrophobicity demonstrated the highest sensitivity to small temperature changes of the organogel matrix temperature for both of the wax-types. All other parameters such as the excitation intensity, the mass ratio between natural wax / vegetable oil (40 wt.% / 60 wt.%), the type of the oil (RBO) and molar concentration of a sensitizer/emitter couple were kept constant. Figure 4.9 reveals

that the TTA-UC system, that is embedded in the organogel matrix material based on carnauba wax, demonstrates higher optical signals (especially for the rSPh) and monotonic increase of the dEF signal. This fact explains the higher temperature sensitivity for carnauba-based samples. It is worth mentioning that a similar behavior was also observed for other emitter molecules.

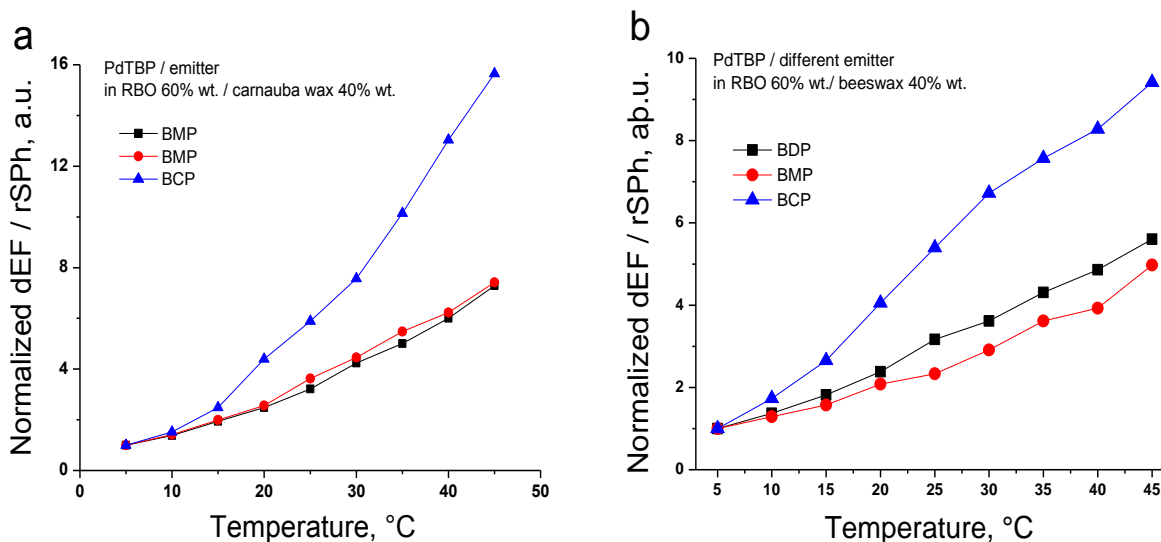


Figure 4.8 - Temperature dependences of the normalized ratio of dEF / rSPh for sensing TTA-UC systems, with varying composition, as follow: the matrix consisting of RBO 60 wt.% / carnauba wax (a) or beeswax (b) 40 wt.% and different emitters - BDP (black squares), BMP (red circles) or BCP (blue triangle). For all the measurements – the same sensitizer PdTBP was used. The spectra are obtained at the $t = 15$ s after the start of the optical excitation.

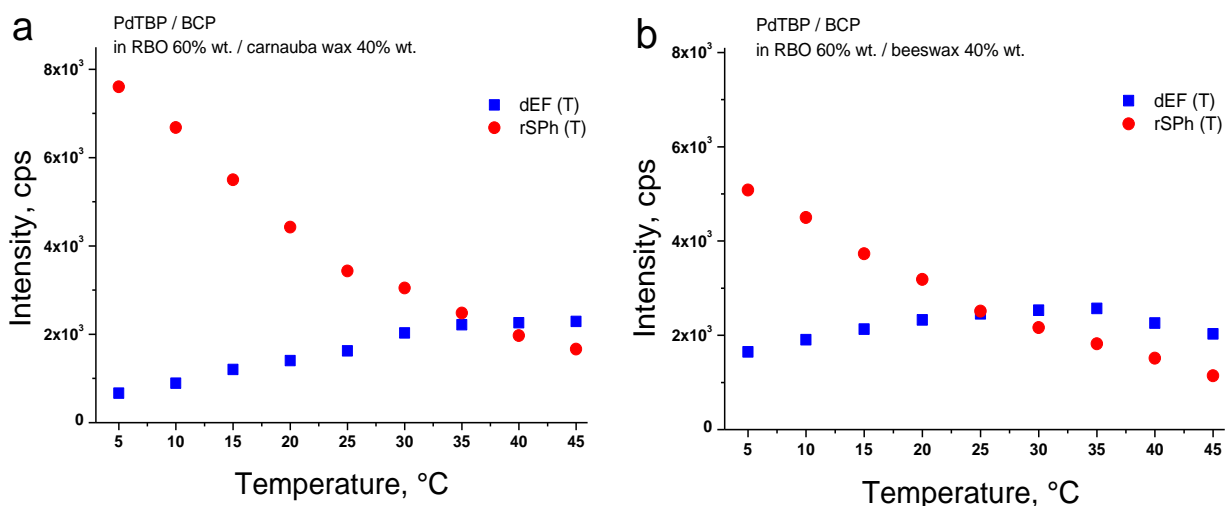


Figure 4.9 - Temperature dependence of the signals of dEF (blue squares) and rSPh (red circles): (a) – for TTA-UC systems based on carnauba wax; (b) – for the TTA-UC systems based on beeswax.

4.6.2 Temperature dependence of composition-tunable organogel matrices

Luminescence efficiency of UC-dyes in organogel highly depends on matrix composition. Physicochemical properties of used ingredients for organogel formation play an essential role in a temperature behavior of obtained organogel matrixes. Density and viscosity of the organogel matrices can be regulated by a proportion of wax and oil. The ratiometric optical response of the UC-dyes incorporated in organogel was used as an indicator for searching the optimal wax-oil matrix composition with maximum temperature sensitivity (Figure 4.10). Increasing the oil content in the matrix composition leads to a rising temperature sensitivity of the organogel. This fact can be explained by the increasing mobility of dye molecules in the wax-oil environment. The rotational diffusion coefficient of dyes strongly depends on the viscosity of the matrix according to Stokes–Einstein–Debye equation.¹⁶² Consequently, the decrease of the viscosity of dye’s environment facilitates the re-orientation of dye molecules and cardinally enhances the efficiency of the TTA-UC process in the environment.

Experimental results confirm the statement for wax-based organogels with PO (Figure 4.10 (c), (d)). Slightly different behaviors are observed for organogels with RBO and AO. The organogels follow the same trends of viscosity dependence as the organogel matrix with PO. However, a maximum of temperature sensitivity is achieved at 60 wt.% of oil content. The subsequent increase of the oil’s portion leads to the decrease of the temperature sensitivity of the matrix. In this way the optimal wax-oil content for the organogel formation was determined.

It has to be noted, that carnauba wax-based organogels show better temperature sensitivities compared to beeswax-based organogels at the same conditions (Figure 4.10). The results can be explained by the difference in melting points of these organogel matrices. Carnauba wax-based organogels form a stronger network with a higher melting point compared to beeswax-based organogels. Carnauba wax-based organogel shows a strongly monotonic increase of the dEF-signal by increasing the sample temperature, simultaneously with the strongly monotonic decrease of the rSPh-signal by rising of sample temperature (Figure 4. 11 (a)). At the same conditions, beeswax-based organogel shows an increase of dEF-signal only till 30-35 °C and then the level of the signal falls (Figure 4.11 (b)).

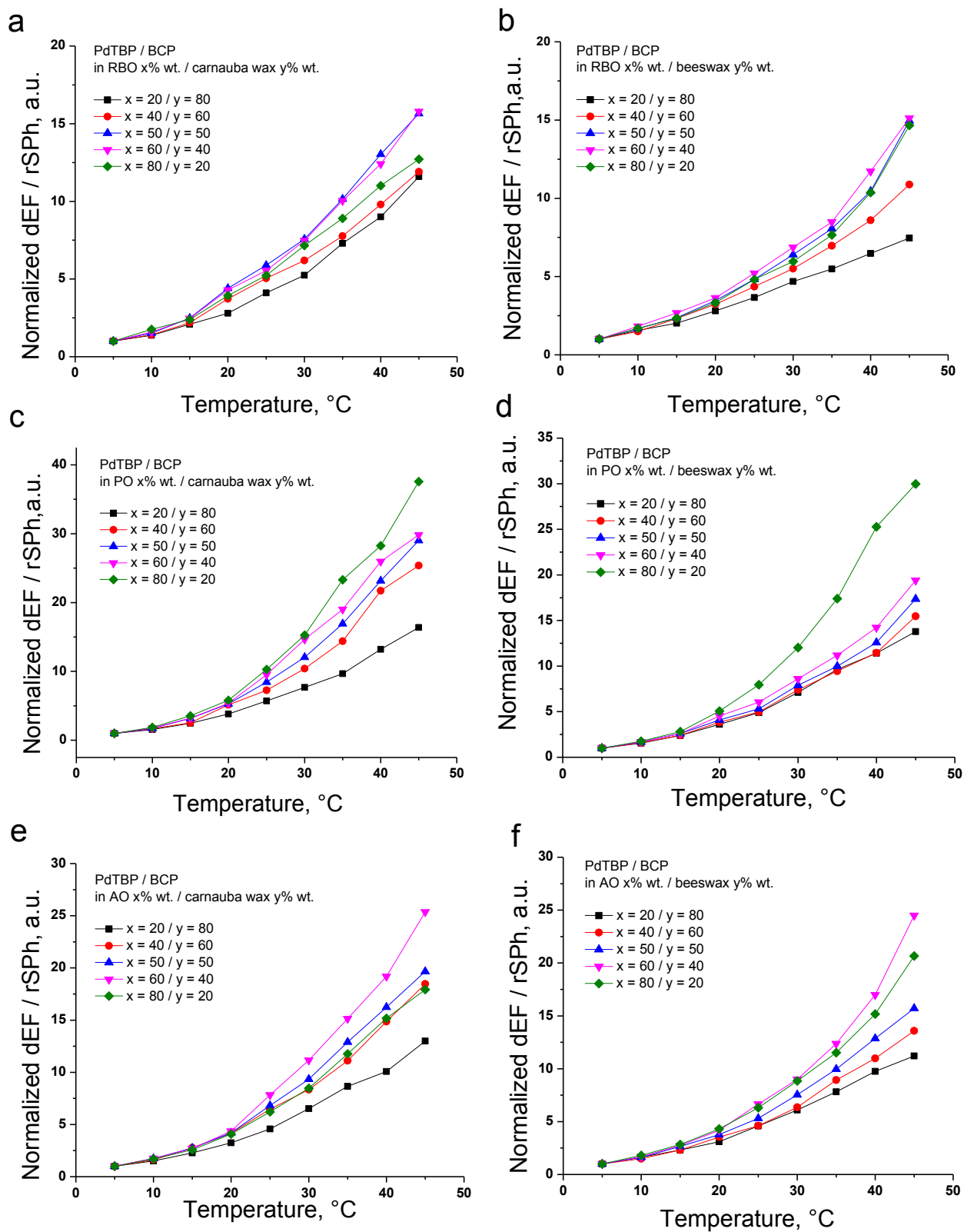


Figure 4.10 - Temperature dependencies of the normalized relations of maximal intensity of UC-fluorescence signal to maximal intensity of phosphorescence signal for organogels with the next composition PdTBP / BCP in (a) RBO / carnauba wax, (b) RBO / beeswax, (c) PO / carnauba wax, (d) PO / beeswax, (e) AO / carnauba wax, (f) AO / beeswax.

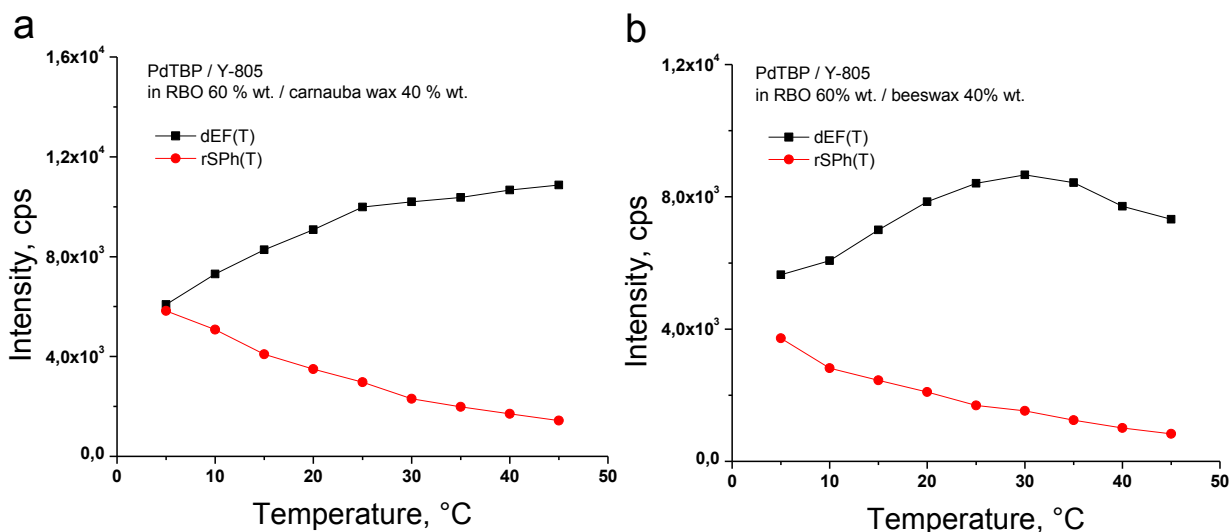


Figure 4.11 - Temperature dependences of the normalized relations of maximal intensity of dEF-signal to maximal intensity of rSPh-signal for PdTBP / BDP in RBO 60 wt.% / beeswax (a) and carnauba wax (b) 40 wt.%

4.6.3 Organogel matrices containing different vegetable oils

The type of vegetable oil incorporated in a UC-organogel matrix has a strong effect on the temperature response of the UC-organogel. Since vegetable oils contain chemically different antioxidant compounds, they differ in viscosity and other characteristics. The next optimization step of the UC-organogel matrix composition is shown in Figure 4.12: only the type of vegetable oil has been optimized here. As evident from the results, the sample, containing PO, demonstrates the highest temperature sensitivity than the organogels containing AO or RBO.

Temperature responses carnauba-based organogel matrices at 35 °C and 45 °C, respectively, are 10.15 and 15.65 for RBO; 12.19 and 18.97 for AO, 16.91 and 29.01 for PO. These values have the following magnitudes for beeswax-based organogel matrices at 35 °C and 45 °C, respectively: 8.06 and 14.95 for RBO; 9.95 and 15.70 for AO, 10.07 and 17.36 for PO. The temperature response is more pronounced in carnauba wax-based organogels. The best temperature response was observed for the UC-organogels with PO. This phenomenon can be explained by more effective singlet oxygen scavenging ability of PO compared to other vegetable oils.

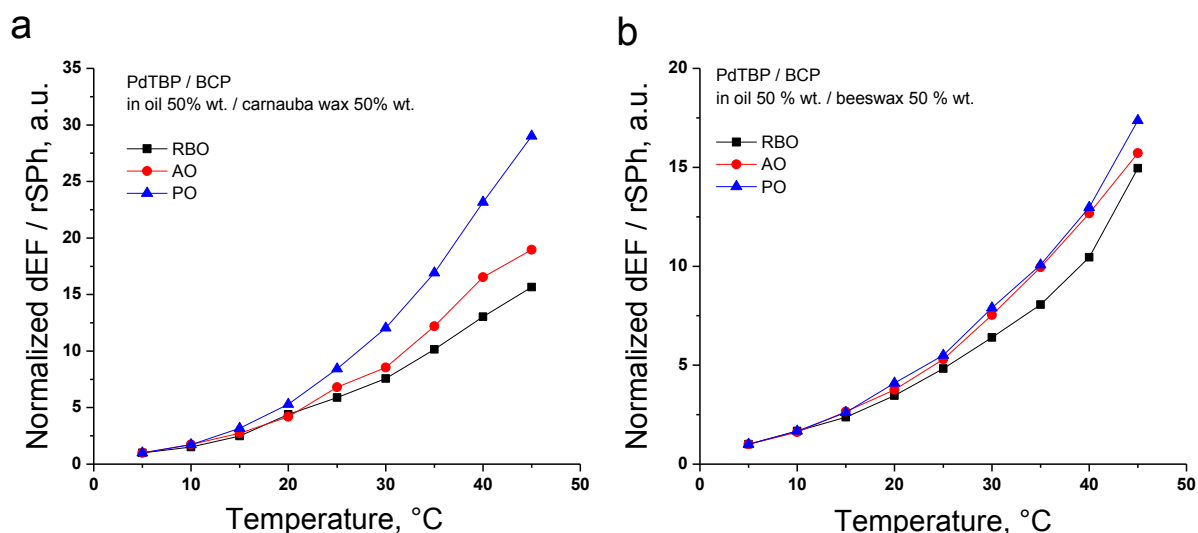


Figure 4.12 - Temperature dependence of the normalized relation of maximal intensity of dEF signal to maximal intensity of rSPh signal for organogels with next composition PdTBP / BCP in (a) oil 50 wt.% / carnauba wax 50 wt.% and (b) oil 50 wt.% / beeswax 50 wt.%

4.6.4 UC-organogel matrix composition with maximal temperature sensitivity

The next optimization step for a search of the optimal UC-organogel matrix composition with maximal temperature sensitivity is an evaluation of the temperature responses of the UC-organogels with a different in percentage proportion of natural wax and vegetable oil. For this aim the UC-organogels consisting PO and carnauba wax were prepared in the following ratio: 20 – 80 wt.% PO / 80 – 20 wt.% carnauba wax, respectively.

The increase of a solid lipid percentage part in the matrix composition impacted the temperature response. The experimental results are shown in Figure 4.13 (a). It has been demonstrated that the UC-organogel composition PdTBP / BCP in PO 80 wt.% / carnauba wax 20 wt.% it (the violet triangles) with the highest sensitivity to the temperature changes inside the biologically relevant interval around 36 °C. This composition has shown a strongly monotonic increase of the dEF signal by increasing of the sample temperature (Figure 4.13 (b), the blue squares). The rSPh signal has a strongly monotonic decrease by rising of sample temperature (Figure 4.13 (b), the red circles).

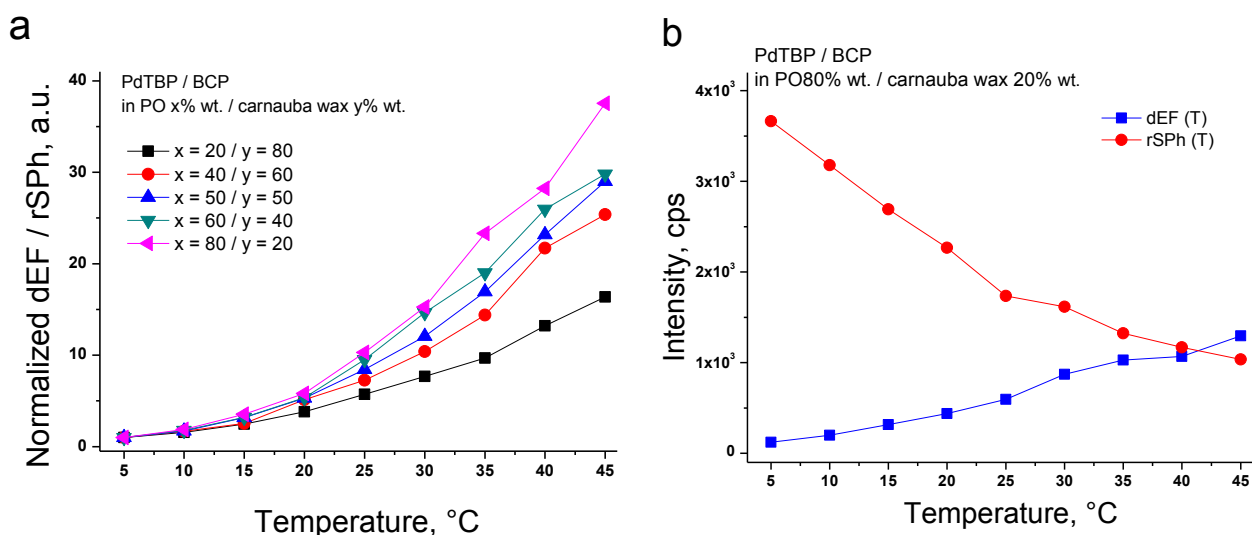


Figure 4.13 - (a) Calibration curve based on temperature dependences of the normalized ratio of dEF / rSPH for UC-organogels, based on PdTBP / BCP in varying composition of carnauba wax / PO. (b) Temperature dependence of the signals of dEF (blue squares) and rSPH (red circles) for the optimal UC-organogel composition PdTBP / BCP in PO 80 wt.% / carnauba wax 20 wt %.

This experimental fact ensures the creation of a non-ambiguous calibration curve. This calibration curve connects the measured ratio of the dEF / rSPH signals and local sample temperature (across the optically excited laser spot). For the identified optimal material composition (Figure 4.13 (a), the violet triangles) the ratio dEF / rSPH is changed more than in 15 times for the temperature interval of $\Delta T = 15\text{ }^{\circ}\text{C} - 45\text{ }^{\circ}\text{C}$. This allows us to achieve of temperature sensitivity up to 100 mK. The temperature sensitivity was achieved in the ambient environment, around the life-science relevant temperature.

4.6.5 Amphiphilic additives effect on ratiometric temperature response of UC-organogel matrices

As the next optimization step, mixtures of natural oil (RBO, fixed amount close to 60 wt.%), natural waxes (beeswax, carnauba wax, fixed amount 40 wt.%) and different amphiphilic moieties such as lecithin, glycerol, TX-100 and OMe-PEG₃₅₀ were compared as the matrices providing the influence on the temperature sensitivity of the TTA-UC process. The influence of the amphiphilic additive lecithin is reported in Figure 4.14. It is evident that lecithin decreases (Figure 4.14, the black line) the sensitivity of the TTA-UC

process to the temperature changes. Therefore lecithin was excluded from further optimization steps.

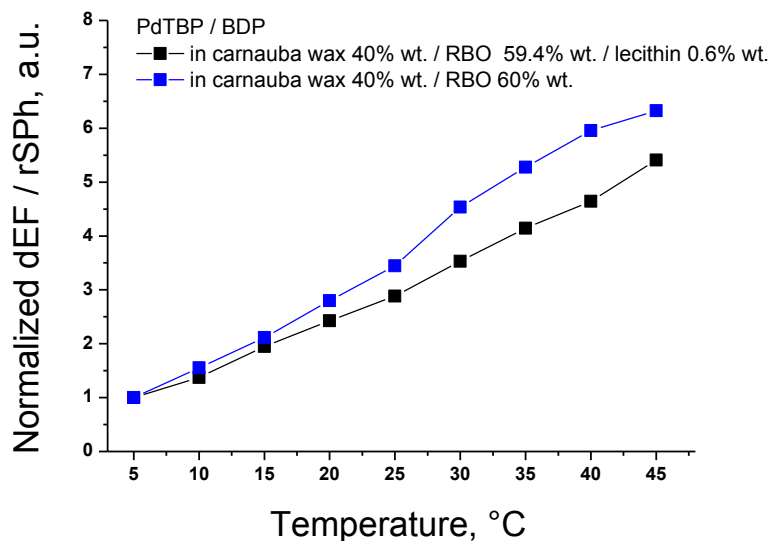


Figure 4.14 - Temperature dependence of the normalized ratio of maximal intensity of dEF signal to maximal intensity of rSPh signal for the same TTA-UC systems - PdTBP/BDP, embedded in the matrix, as follows: blue line – containing carnauba wax 40 wt.% / RBO 60 wt.%; black line - lecithin 0.6 wt.%/ RBO 59.4 wt.% / carnauba wax 40 wt.%.

The experimental results reported in Figures 4.15 (b), 4.16 (b) and 4.17 (b) are summarized and elucidated in Figure 4.19. The experimental results reported in Figures 4.17 (b) and 4.18 (b) are summarized and elucidated in Figure 4.20. The presence of amphiphilic moieties causes a heterogeneous response of the sensitivity to a sample temperature change for the UC-system containing of PdTBP / BMP in RBO 59.6 wt.% / beeswax 40 wt.% / amphiphilic moiety 0.6 wt.% (Figure 4.19).

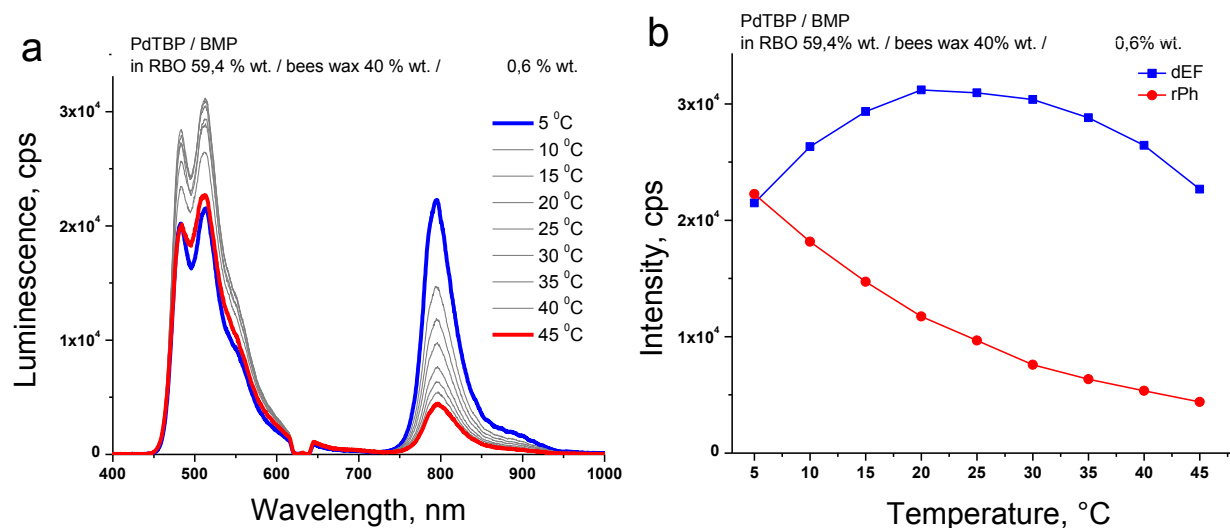


Figure 4.15 - (a) Luminescence spectra for the UC-organogel containing of PdTBP / BMP in RBO 59.4 wt.% / beeswax 40 wt.% / TX-100 0.6 wt.% upon different temperatures; an air saturated environment. The spectra are obtained at $t = 200$ s after start of the optical excitation. (b) Temperature dependence of the signals of dEF (at $\lambda_{max} = 521$ nm) and rSPh (at $\lambda_{max} = 796$ nm) on the sample temperature.

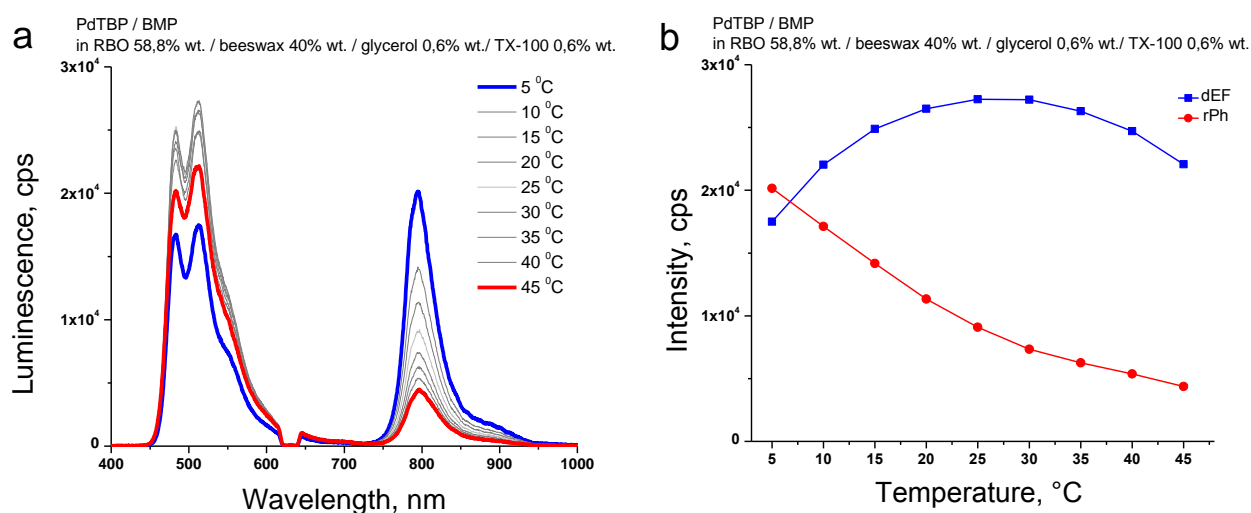


Figure 4.16 - (a) Luminescence spectra for the UC-organogel containing PdTBP / BMP in RBO 58.8 wt.% / beeswax 40 wt.% / TX-100 0.6 wt.% / glycerol 0.6 wt.% upon different temperatures. (b) Temperature dependence of the signals of dEF (at $\lambda_{max} = 521$ nm) and rSPh (at $\lambda_{max} = 795$ nm) on the sample temperature. Experimental conditions are the same as in Figure 4.15.

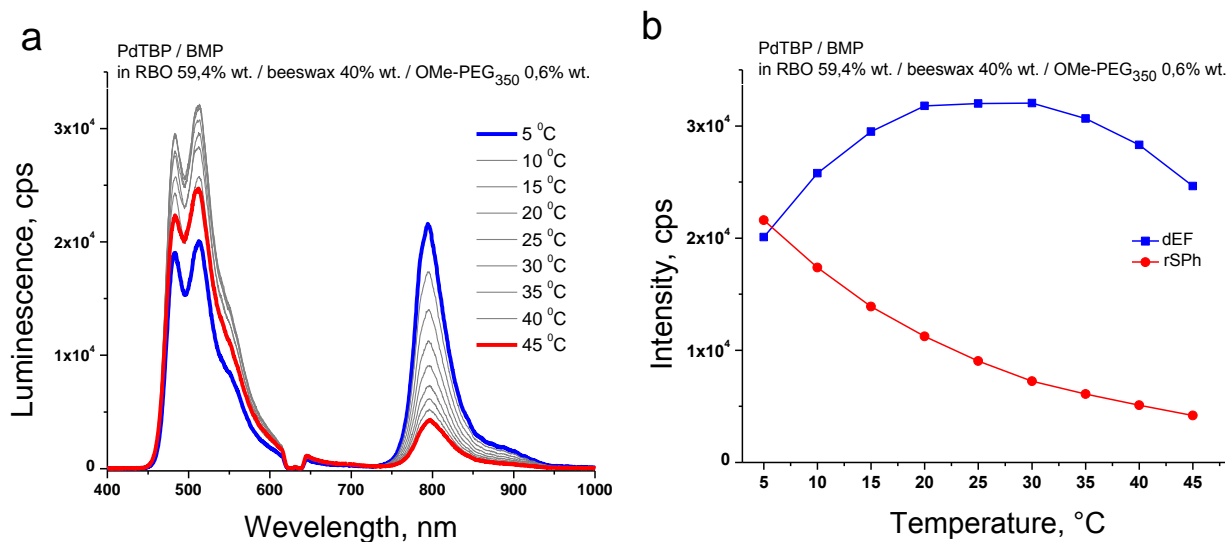


Figure 4.17 – (a) Luminescence spectra for the UC-organogel containing PdTBP / BMP in RBO 59.4 wt.% / beeswax 40 wt.% / OMe-PEG₃₅₀ 0.6 wt.% upon different temperatures. (b) Temperature dependence of the signals of dEF (at $\lambda_{max} = 521$ nm) and rSPh (at $\lambda_{max} = 796$ nm) on the sample temperature. Experimental conditions are the same as in Figure 4.15.

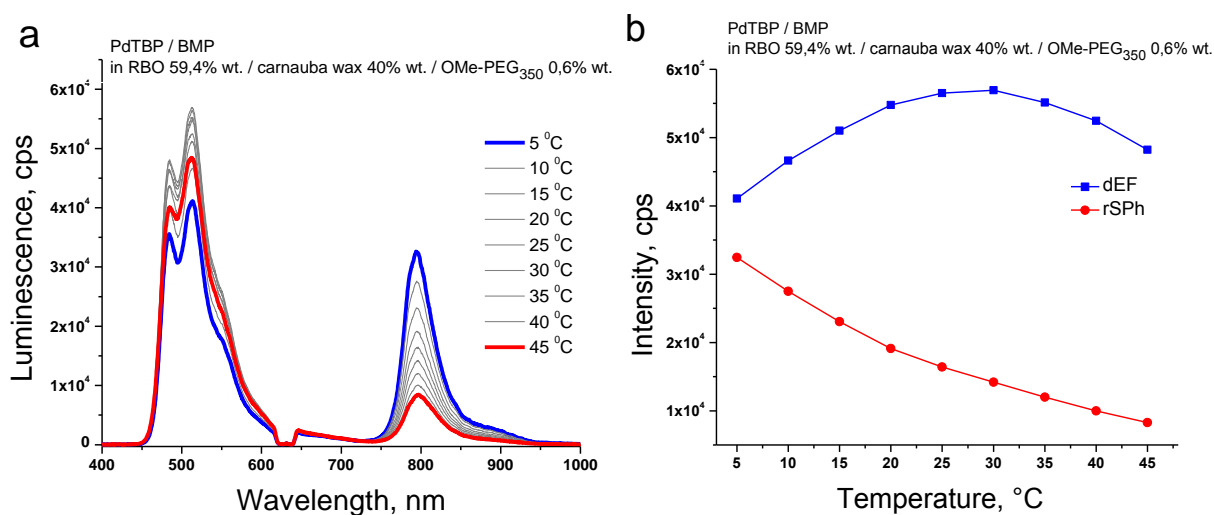


Figure 4.18 – (a) Luminescence spectra for the UC-organogel containing PdTBP / BMP in RBO 59.4 wt.% / carnauba wax 40 wt.% / OMe-PEG₃₅₀ 0.6 wt.% upon different temperatures. (b) Temperature dependence of the signals of dEF (at $\lambda_{max} = 521$ nm) and rSPh (at $\lambda_{max} = 796$ nm) on the sample temperature. Experimental conditions are the same as in Figure 4.15.

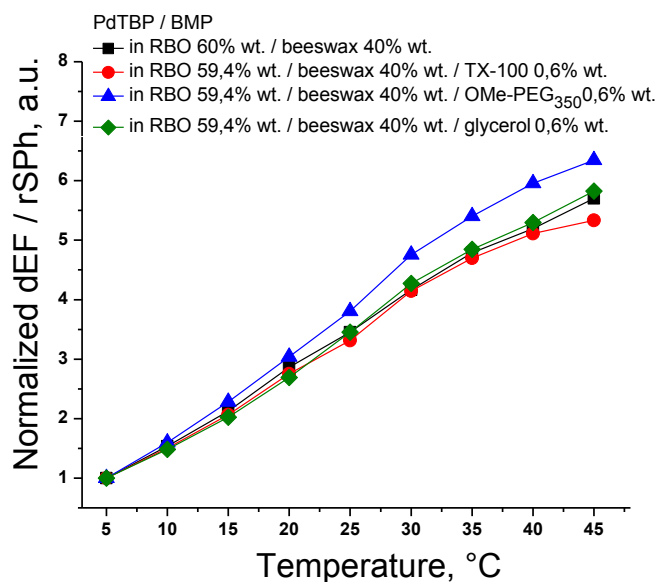


Figure 4.19 - Temperature dependence of the normalized ratio of the maximal intensity of dEF to maximal intensity of rSPh for UC-organogels containing PdTBP / BCP in RBO 59.6 wt.% / beeswax 40 wt.% / amphiphilic moiety 0.6 wt.% (fixed amount), as follows: red line – TX100; green line – glycerol; blue line – OME-PEG₃₅₀; black line – a control sample.

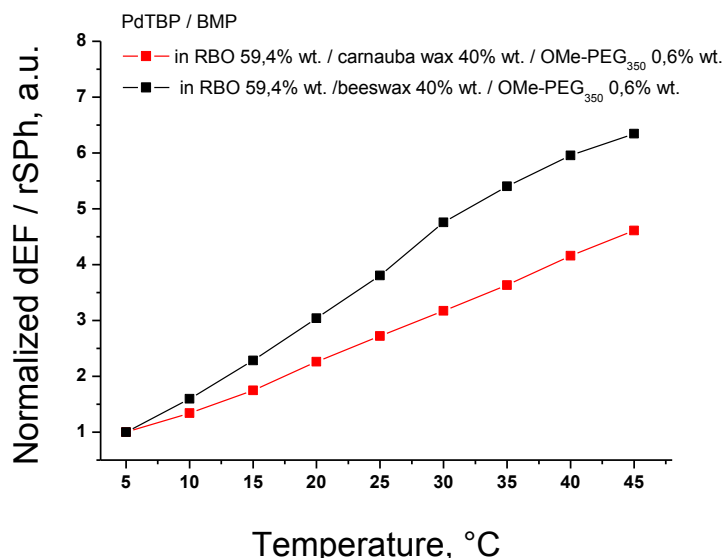


Figure 4.20 - Temperature dependences of the normalized ratio of the maximal intensity of dEF signal to maximal intensity of rSPh for UC-organogels containing PdTBP / BCP in RBO 59.6 wt.% / natural wax 40 wt.% / OME-PEG₃₅₀ 0.6 wt.% as follows: black line – beeswax; red line – carnauba wax.

The best results obtained for the temperature sensitivity of the process of the TTA-UC embedded in the soft mater matrix are shown in Figure 4.21. The best working UC-system is based on the matrix composition, including PdTBP / BCP in RBO 59.6 wt.% / carnauba wax 40 wt.% / OMe-PEG₃₅₀ 0.6 wt %.

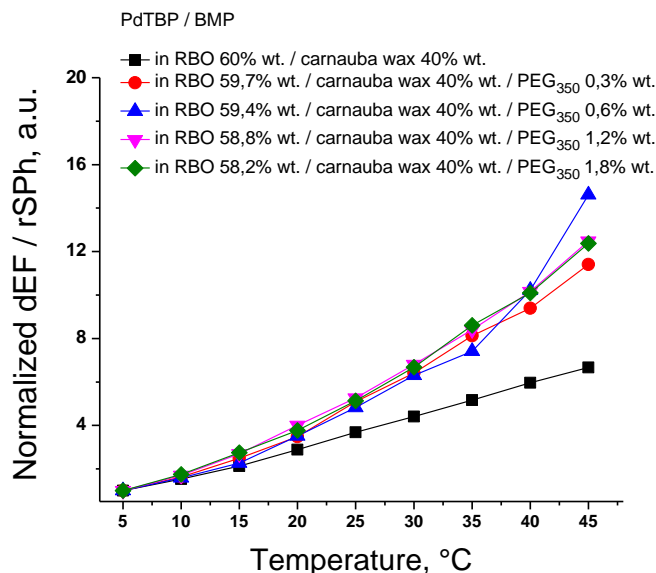


Figure 4.21 - Temperature dependence of the normalized ratio of the maximal intensity of dEF signal to maximal intensity of rSPh for UC-organogel matrices with different wt.% concentration OMe-PEG₃₅₀.

The ratio dEF / rSPh is changed more than in 15 times for a temperature interval of $\Delta T = 15 \text{ }^\circ\text{C} - 45 \text{ }^\circ\text{C}$ centered around the temperature of interest $\sim 36 \text{ }^\circ\text{C}$ for concentration of 0.6 wt.% OMe-PEG₃₅₀ (Figure 4.21, Figure 4.22 (a)). The completely monotonic change for both signals (for the dEF-signal as well as for the rSPh-signal) with a temperature increase was observed for this UC-organogel composition.

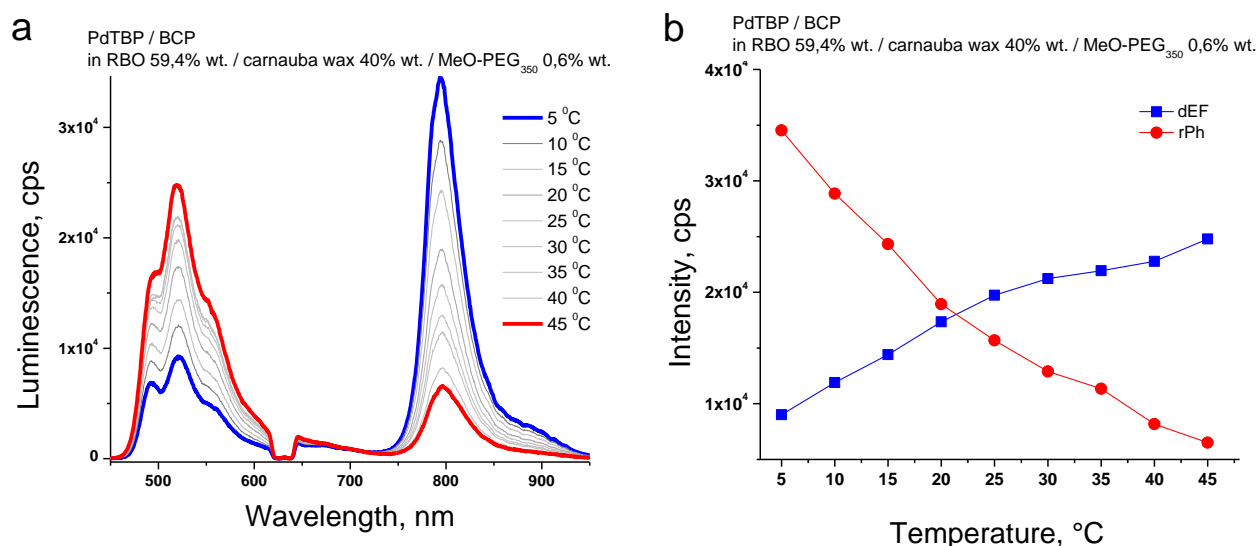


Figure 4.22 - Luminescence spectra for the UC-organogel based on PdTBP / BCP embedded in the matrix containing RBO 59.4 wt.% / carnauba wax 40 wt.% / OMe-PEG₃₅₀ 0.6 wt.% upon different temperatures; $\lambda_{exc} = 635$ nm; an air saturated environment. The spectra are obtained at $t = 200$ s after the start of the optical excitation. (b) – Temperature dependence of the signals of dEF (at $\lambda = 521$ nm) and rSPh (at $\lambda = 796$ nm) on the sample temperature.

4.7 Conclusions

The optical temperature sensing in natural wax and vegetable oil based organogel matrices via annihilation upconversion was realized in this study for the first time. The sensing technique is based on the ratiometric type signal registration. That ensures significant independence of the obtained data on excitation intensity instabilities, local molecular concentration fluctuations, and field-of-view variations. This type of organogels can be used as a great platform for constructing a temperature-sensing system due to their composition of biocompatible and pharmaceutically acceptable components.

During the experimental part the complex optimization procedure of the UC-organogel matrix composition served as T-sensor was performed. The selected UC-organogel matrix composition is entirely biocompatible and mostly consists of natural waxes and vegetable oils. The matrix material is exclusively hydrophobic and is a suitable solvent of the hydrophobic optically active molecules. The UC-organogel matrix composition demonstrates sacrificial singlet oxygen scavenging properties allowing long-term operation of the T-sensors in the ambient environment (more than 200 s continuous laser

excitation). The UC-organogel matrix material ensures the significant increase of the rotational diffusion of the optically active molecules for a temperature interval centered at 36 °C. The ratio of the dEF to rSPh changes more than in 15 times.

Chapter 5: Sensing technique based on solid lipid upconverting nanoparticles

5.1 Introduction

The health status of an organism can be defined by a complex of various biochemical and physiological parameters and processes that ensures its normal functionality. Cells regulate the physiological values within certain ranges for normal vital activity and metabolism. These intrinsic cellular parameters deviate from their physiological limits in case of any disturbances in cells and can serve as indicators for the diagnostics of a number of diseases, for instance, various types of cancer.

The immune system is a powerful controlling system for the identification and destruction of abnormal cells. For example, some cells of the immune system, such as T-cells and natural killer cells, are mediators of anti-tumor immunity. Unfortunately, in some cases, cancer cells can acquire mutations or other changes that allow escaping the detection by the immune system, and the tumor is progressing.²⁹ In this way, effective differentiation between normal and abnormal cells is an essential challenge for timely detection of the diseases, it prevents its further progression and successful treatment.

The development of a nanoscale biosensors possessing pronounced sensitivity and ability of independent quantitative measurements of small changes of physiological parameters (oxygenation and local temperature) at a cellular level is a critically important step on the way to the creation of a new powerful diagnostic tool. There are no non-invasive techniques for simultaneous and independent cellular thermometry and oxygenation at the moment. The current employing tools for measuring tissue oxygenation (pO_2) and the internal temperature of living cells are described in Chapter 1, paragraph 1.2.

The organic material-based nanoparticles are one of the most promising candidates as the intracellular probes for biosensing and imaging due to their composition of biocompatible components among the available colloidal systems. The solid lipid nanoparticles (SLNPs) are capable to provide the real-time monitoring of physiological parameters of living cells in the upconversion regime (Figure 5.1). The nanocarriers

consist of a mixture of a solid and a liquid lipid. The solid-liquid lipid matrix forms a temperature-dependent and radical scavenging matrix with a well-dispersed energetically optimized sensitizer and emitter dyes. The nanocarriers are stabilized with pharmaceutically acceptable surfactants.

The TTA-UC process demonstrates pronounced sensitivity to oxygen and also to temperature due to a viscosity-dependent motion of dyes in a solid-liquid lipid matrix. The association of these processes represents a possible approach for local temperature and oxygen sensing in bio-objects. Upconversion-based solid lipid nanoparticles (UC-SLNPs) have many advantages such as high chemical stability and large excitation light-penetration depth compared with the traditional fluorescent probes (organic dyes, metal complexes, or inorganic quantum dots).⁵⁵

5.2 Optical properties of tissue and requirements to sensing tool

The optical properties of a biological tissue (absorption, scattering, penetration) have a significant effect on therapeutic and diagnostic applications of light.¹⁷⁶ The total optical losses of the human skin compose of the absorption spectra of hemoglobin and melanin, proportional to the volume fractions of eumelanin/pheomelanin and oxygenating status of the hemoglobin combined with the relative contributions of Mie and Rayleigh scattering properties of collagen and keratin fibers.¹⁷⁷ The optical properties of skin are fairly variable not only in the scattering properties but also in the degree of melanin pigmentation and the amount and distribution of blood perfusion.¹⁷⁸

Nanoconfined sensing UC-systems should convert deep-red light (660 - 700 nm) into visible red light ($\Delta\lambda = 610 - 640$ nm) under low-intensity excitation (less than 100 mW cm^{-2}) for effective applications in life-science. This specific requirement arises from the absorption spectra of the main tissue components of the human skin close to the breast sentinel lymph nodes. It is composed of many optically active moieties: hemoglobin (oxygenated and deoxygenated), eumelanin and pheomelanin, white adipose tissue (WAT), etc.

The optimized UC-systems should demonstrate pronounced sensitivity to small changes in the sample temperature. The UC-signal depends on the local mobility of the

participating sensitizer and emitter molecules. The dEF ($\Delta\lambda = 610 - 640 \text{ nm}$) increases, and the rSPh decreases ($\Delta\lambda = 800 - 900 \text{ nm}$), when the sample temperature increases. It is of crucial importance that the increase of the molecular rotational diffusion of the optically active materials is observed for a temperature interval centered at 36° C . It allows the TTA-UC to be used as a T – sensing process for life-science applications. The matrix material, where the TTA-UC is carried out, must demonstrate sacrificial singlet oxygen scavenging properties in order to ensure a long-term operation of the T-sensors in ambient environment.

5.3 Sensing procedure

Modern biomedical optical sensing technologies make it possible to measure practically all of the physical measures of interest and a large number of chemical quantities.¹⁷⁹ Many of these methods have allowed more in-depth exploring and understanding the mechanisms of cell functionalization. That opens perspectives for monitoring of vital cellular activity and detection pathologies in the cell development.

We propose a new optical sensing technique based on TTA-UC for real-time monitoring of important physiological parameters such as temperature and oxygen content at the cellular level. The optical sensing involves UCNPs excitation and ratiometric registration of dEF- and rSPh-signals as a function of local temperature in an oxygen environment. This sensing procedure includes two divided in time stages: oxygen sensing (detection of the delay time of rSPh) and temperature sensing (measurement of the maximal intensity of dEF- and rSPh-signals) (Figure 5.1). The measurement starts with oxygen sensing. Excitation of UC-SLPs in the upconversion regime is accompanied by energy transfer to ground-state oxygen. The oxygen is excited to the singlet state. The singlet oxygen is instantly captured by antioxidant compounds of the solid-liquid lipid matrix. The maximal rSPh-signal can be detected only after the complete elimination of oxygen within a local environment. The initial oxygen concentration can be determined on the base of the excitation intensity and the delay time of rSPh. The temperature sensing is realized by measuring the maximal intensity of dEF- and rSPh-signals in this optically created a local

oxygen-free environment. The normalized mutual dependence of these parameters reports the local temperature in a ratiometric-type optical response.

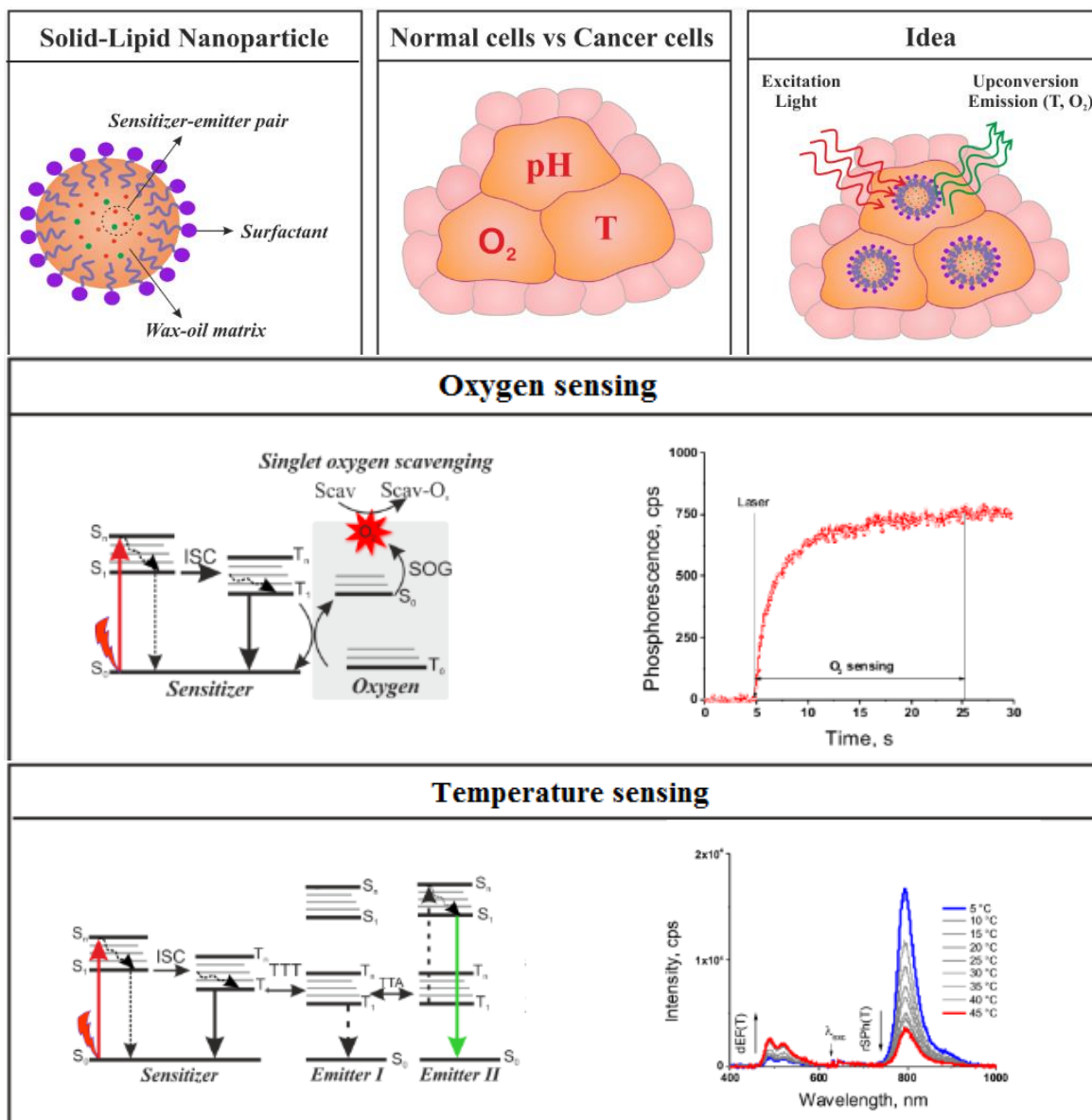


Figure 5.1 - Simplified optical oxygen and temperature sensing procedure for monitoring physiological parameters at the cellular level. SOG – Singlet Oxygen Generation, Scav – singlet oxygen scavenging compounds.

5.4 Experimental part

5.4.1 Materials

The sensitizer molecules PdTBP, Pd(II) mixture of benzo / naphto porphyrin (Y-894) and the emitter molecules – BCP, dibenzo[hi,st]ovalene¹⁸⁰ (DBOV-Mes) were used as

energetically optimized sensitizer and emitter pairs. PdTBP, Y-894 and BCP were synthesized by Dr. Yuri Avlasevich. The molar concentration of sensitizer is 1×10^{-5} M, the emitters - 2×10^{-4} M. All the information about the molar concentration changes will be indicated for the entire optimization process. The chemical structures, absorption and emission spectra of all molecules are shown in Figure 5.2, 5.3, 4.5 (Chapter 4) and 3.2 (Chapter 3).

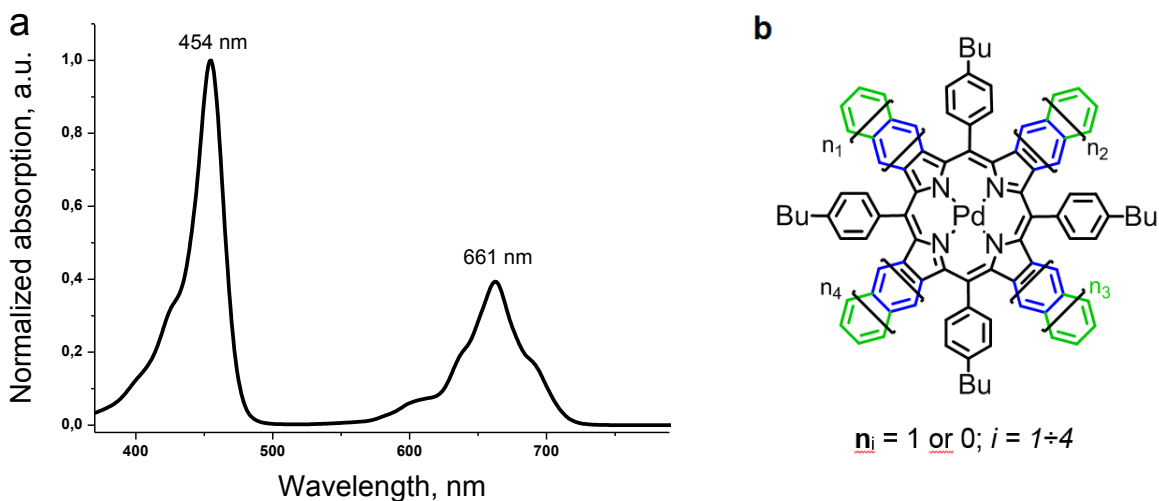


Figure 5.2 - (a) Absorption spectrum of mixed benzo / naphtho porphyrin; (b) chemical structure of mixed benzo / naphtho porphyrin.

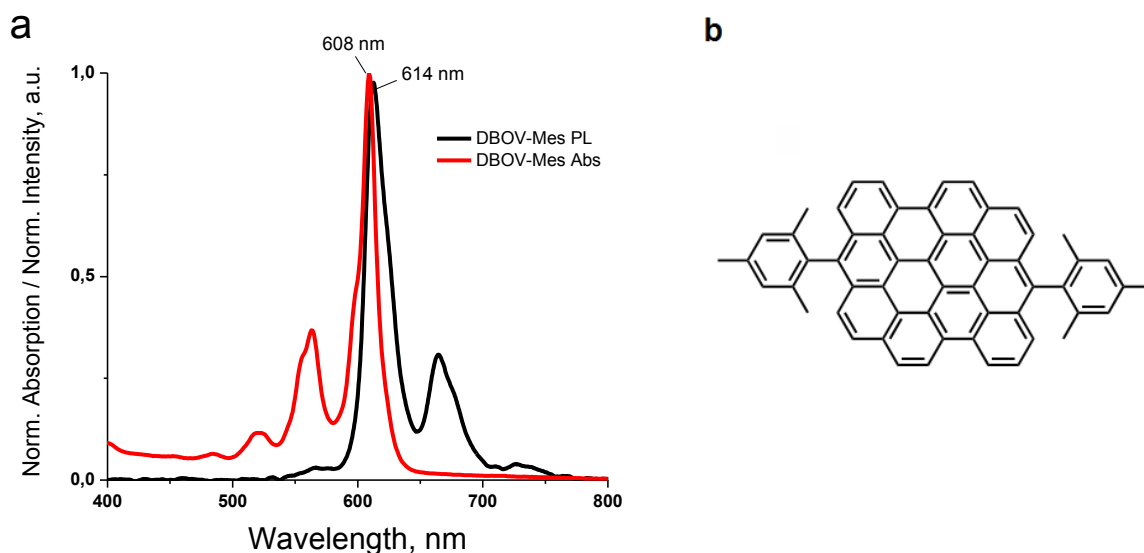


Figure 5.3 - (a) Absorption and luminescence spectra of Dibenzo[hi,st]ovalene; (b) chemical structure of dibenzo[hi,st]ovalene.

Polysorbate 20 (Tween-20, hydrophilic-lipophilic balance (HLB) =16.7), Polysorbate 80 (Tween-80, HLB=15.0), polyethylene glycol octadecyl ether (Brij-78, HLB=15.3), TX-100 (HLB=13.5) and glycolic acid ethoxylate 4-nonylphenyl ether (GAET) were used as surfactants. The structures are shown in Figure 5.4 and 4.6 (Chapter 4).

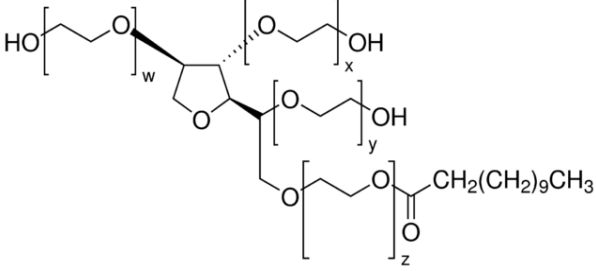
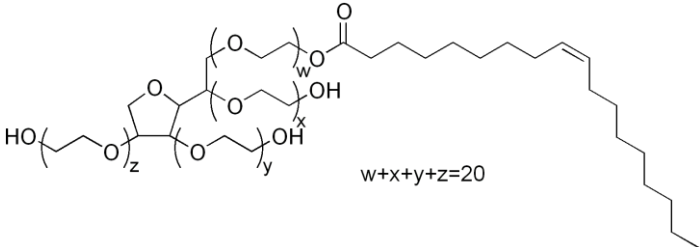
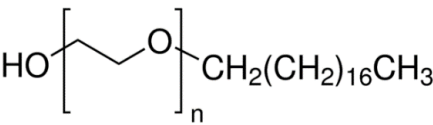
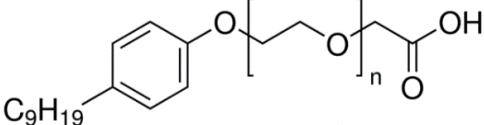
Tween-20	
Tween-80	
Brij-78	
GAET	

Figure 5.4 – Chemical structures of Tween-20, Tween-80, Brij-78 and GAET.

Carnauba wax (Acros Organics, USA) was chosen as matrix material because it allows the significant increase of the molecular rotational diffusion of the optically active molecules for the temperature interval centered at 36 °C. Carnauba wax is biocompatible and defined as a food additive. The composition and chemical structure of the main wax ingredient are shown in Figure 4.2.

RBO and squalene (Merck, Germany) were applied as emollients. The main reason to use emollients is the ability of a controllable lowering of the melting point of the mixture of natural wax/emollient. The macroscopic melting point of the wax/oil mixture cannot be used as the only optimization criterion.

The following chemicals were obtained from commercial sources and used as received: toluene and ethyl acetate from VMR (France), Tween-20, Tween-80, Brij-78 and GAET from Merck (Germany).

5.4.2 UC solid lipid nanoparticles synthesis

The UC-SLNPs were prepared by an emulsion solvent evaporation method (Figure 5.5).

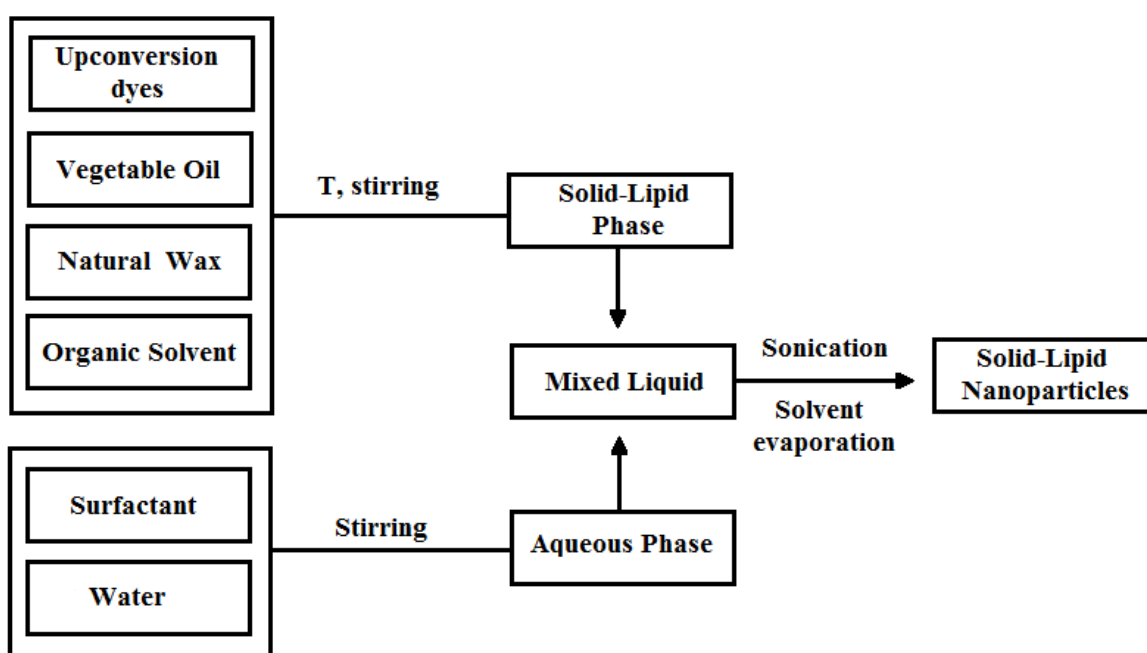


Figure 5.5 - Schematic representation a procedure of UC-SLNPs preparation by the emulsion solvent evaporation method.

Toluene solutions of sensitizer (10^{-4} M, 150 μ L) and emitter (10^{-3} M, 300 μ L) were mixed at room temperature, and the solvent was evaporated to dryness under vacuum (40 $^{\circ}$ C, 74 mbar). The residue was dissolved in a mixture of RBO (180 mg), ethyl acetate (1 mL) or mixture of RBO (90 mg), squalene (90 mg), ethyl acetate (1 mL) and added to molten

wax (120 mg) at 86 °C, mixed at room temperature for forming a homogeneous solution. Then 5 mL of 1% aqueous solution of surfactant was added at room temperature, and the sample was ultrasonicated (Branson W-450D Digital Sonifier, amplitude 90%, 1/2 inch tip) for 4 min (15 s pulse / 5 s pause).

The organic solvent was removed from the formed emulsion by the evaporation under reduced pressure at 20 - 25 °C. The absence of ethyl acetate in the particles was confirmed by NMR spectroscopy. Free surfactant was removed by dialysis in 4L distilled water in a low-speed stirring beaker for 15 h.

5.4.3 Methods

5.4.3.1 Luminescence measurements

Luminescence spectra and kinetic measurements were performed by using the experimental setup (Figure 5.7). The samples were excited at $\lambda_{exc} = 633$ nm ($I_{exc} = 20$ mW cm⁻²) or $\lambda_{exc} = 658$ ($I_{exc} = 40$ mW cm⁻²) for PdTBP / BCP or Y-894 / DBOV-Mes energetically optimized sensitizer and emitter pairs, correspondingly. By using a system of dielectric mirrors (E02, Thorlabs Inc.), the excitation beam was directed to the sample and focused by an achromatic lens (focal distance 100 mm, numerical aperture NA=0.24). Emission spectra were registered by a spectrometer (Hamamatsu Inc., Japan). The excitation power was controlled by the power meter PM 100D (Thorlabs, USA). The laser spot diameter was $d = 1$ μ m and 0.890 μ m for $\lambda_{exc} = 633$ nm and $\lambda_{exc} = 658$, correspondingly.

UC-SLNPs were stirred in glove-box (4 ppm of O₂) for ~15 h for measurements of a sample at an oxygen-free environment. Then samples were placed in the glass tubes (VITROTUBES™, Hollow Rectangle Capillaries - N2540-50) with the thickness of 400±10 μ m and sealed with an epoxy adhesive. Then the sample was placed in the temperature-controlled chamber for upconversion measurements. The temperature in the chamber was controlled with the Peltier element using computer program from Electron Dynamics Ltd. (Southampton, UK) and recirculation chiller. The sample temperature additionally was controlled by the thermistor (PT100) attached on the top of the sample. The

upconversion measurements of the samples were recorded in the temperature range $\Delta T = 5\text{ }^{\circ}\text{C} - 45\text{ }^{\circ}\text{C}$ with temperature step $5\text{ }^{\circ}\text{C}$.

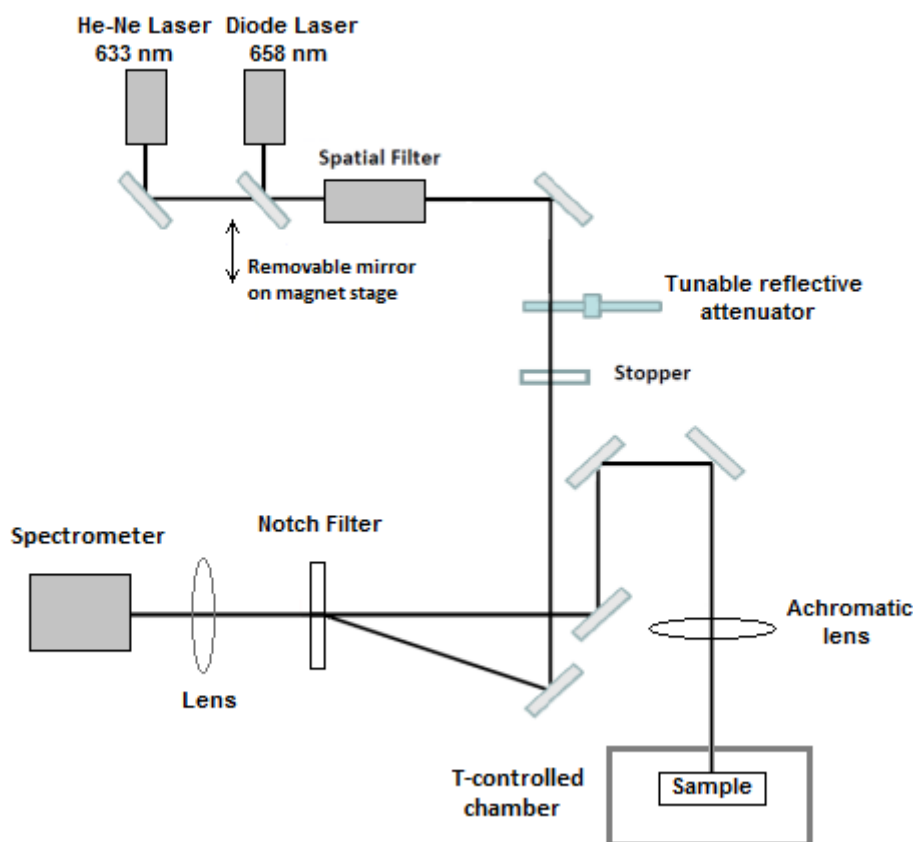


Figure 5.7 – Scheme of the experimental setup.

5.4.3.2 Scanning electron microscopy

Scanning Electron Microscopy (SEM) was performed by using LEO Gemini 1530 (Zeiss, Germany) equipped with the Schottky field emission gun. Best results were obtained by using an in-lens detector at 2.1 mm working distance, 30 μm aperture, and 0.121 keV acceleration voltage.

5.4.3.3 Particle size analysis

Particle size analysis of the UC-SLNPs was performed by dynamic light scattering using a particle size analyzer Zetasizer Nano-S90 (Malvern Instruments, the United Kingdom).

The sample was diluted with distilled water to yield an appropriate scattering intensity and then placed in a cuvette. Dynamic light scattering measurements were carried out at 20 °C. The particle size of the investigated samples was obtained by calculating the average of 10 measurements at an angle of 90°. The method was also allowed evaluating the temporal stability of a colloidal system.

5.4.3.4 Fluorescence microscopy

Live cell images were taken with a commercial setup (LSM SP5 STED Leica Laser Scanning Confocal Microscope, Leica, Germany), consisting of an inverse fluorescence microscope DMI 6000 CS, equipped with a multi-laser combination, five detectors operating in the range of 400-800 nm. A HCX PL APO CS 63 x 1.4 oil objective was used in this study. HeLa cells were seeded at a density of 2×10^4 cells per well in μ -Slide 8 well with a glass coverslip bottom (Ibidi, Germany) and cultured for 24 h in DMEM complete medium (Phenol red free) for confirmation of cellular uptake. After removing of old medium, the cells were incubated for 6 h with UC-SLNPs resuspended in DMEM at a concentration of $2 \text{ mg} \cdot \text{mL}^{-1}$. Subsequently, the cells were washed 5 times with 200 μL of DMEM to remove the remaining nanoparticles outside of the cells, stained subcellular organs with fluorescent dyes and finally suspended in DMEM. The excitation and detection conditions in a sequential mode were described as follows: UC-SLNPs were excited with the Ar laser (488 nm), detected at 510-540 nm and pseudo-colored in green. The cell membrane was stained with CellMask™ Orange ($5 \text{ } \mu\text{g} \cdot \text{mL}^{-1}$, Life technologies, USA), excited with the DPSS laser (561 nm), detected at 570-600 nm, and pseudo-colored in red. Nucleus was stained with Draq@5, excited with a HeNe laser (633 nm), detected at 650-710 nm, and pseudo-colored in blue.

5.5 Results and discussion

5.5.1 Particle characterization

Particle size and their size distribution are important parameters that affect cellular uptake efficiency and biodistribution of NPs.¹⁸¹ These characteristics vary according to the

particle preparation method and composition. The optimal size of NPs also depends on the specific location and the type of targeted tissue in order to realize the desired function. Micrometer-scale particles remain in the body much longer than nanometer-scale particles.¹⁸²

The beeswax and carnauba wax based UC-SLNPs are prepared by the emulsion solvent evaporation technique. The average diameters of the nanoparticles were 343.5 nm and 322.7 nm with a polydispersity index (PDI) 0.342 and 0.250, respectively. The UC-SLNPs stored at refrigerated conditions ($T = 4\text{ }^{\circ}\text{C}$) were stable for over a month. However, a particle growth was observed after five days of the storage, when the UC-SLNPs were stored at a room temperature ($\Delta T = 22\text{ }^{\circ}\text{C} - 25\text{ }^{\circ}\text{C}$). The mean particle size 322.7 nm (a freshly prepared sample) of carnauba wax based UC-SLNPs increased to about 453.8 nm in 5 days because of aggregation of the NPs.

Basic information on particle morphology was obtained by examining UC-SLNPs in the SEM (Figure 5.7). The majority of the NPs are spherical, also among the UC-SLNPs open capsules were observed.

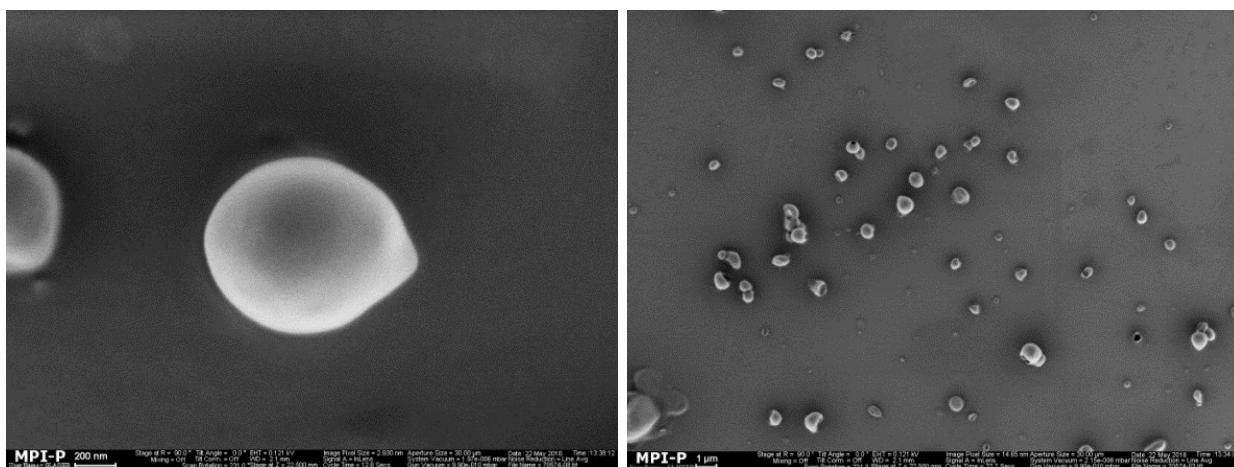


Figure 5.7 – Scanning electron microscopy of UC-SLNPs consisting of PdTBP / BCP in RBO 60 wt.% / carnauba wax 40 wt.% / Tween-20.

5.5.2 Efficiency of dEF and rSPh as a function of solid-liquid lipid ratio in a matrix core of UC-SLNPs

The efficiency of the TTA-UC process strongly depends on the viscosity of a solid-liquid lipid matrix, where dyes have been distributed. For a detailed investigation of the dependence a series of the measurements was conducted with the next ratio solid/liquid lipid part in the UC-SLNPs matrix core composition: 0 wt.% solid / 100 wt.% liquid lipid, 20 wt.% solid / 80 wt.% liquid lipid, 40 wt.% solid / 60 wt.% liquid lipid, 50 wt.% solid / 50 wt.% liquid lipid, 60 wt.% solid / 40 wt.% liquid lipid, 80 wt.% solid / 20 wt.% liquid lipid, 100 wt.% solid / 0 wt.% liquid lipid, stabilized by Tween-20. Carnauba wax was chosen as a solid lipid, and RBO as a liquid lipid. Ratiometric optical response of UC-dyes incorporated in the nanoparticle composition was used as a marker for determining optimal solid-liquid lipid ratio (Figure 5.8).

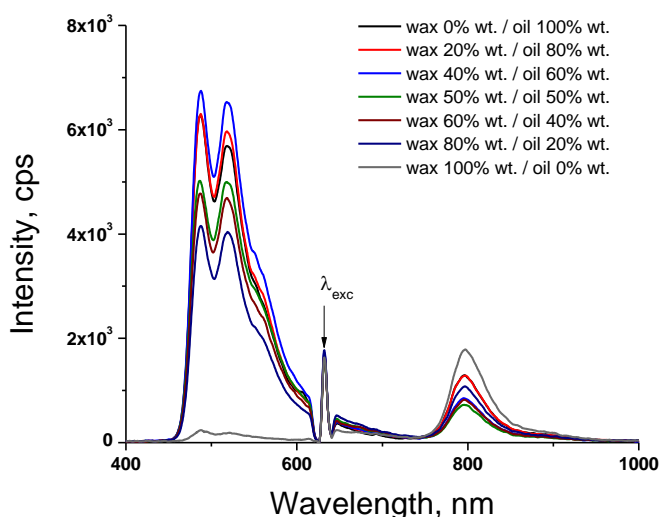


Figure 5.8 - Luminescence spectra of UC-SLNPs with the next ratio solid/liquid lipid part in matrix core composition: PdTBP / BCP in 0 wt.% solid / 100 wt.% liquid lipid, 20 wt.% solid / 80 wt.% liquid lipid, 40 wt.% solid / 60 wt.% liquid lipid, 50 wt.% solid / 50 wt.% liquid lipid, 60 wt.% solid / 40 wt.% liquid lipid, 80 wt.% solid / 20 wt.% liquid lipid, 100 wt.% solid / 0 wt.% liquid lipid, stabilized by Tween-20. Solid lipid - carnauba wax, liquid lipid – RBO. Experimental conditions: $\lambda_{exc} = 635$ nm; an air saturated environment, room T .

In this study a trend is observed: dEF efficiency increases, when the wax part is raised up to 40 wt.% of the matrix core composition. A further increase of the wax content leads to a decrease in the dEF efficiency (Figure 5.8, 5.9). The declining amount of singlet

oxygen scavenging ability of the matrix core composition leads to the decreasing of the dEF-signal, when the solid part is increased. The singlet oxygen scavenging ability of the matrix declines when the liquid lipid part is decreased.

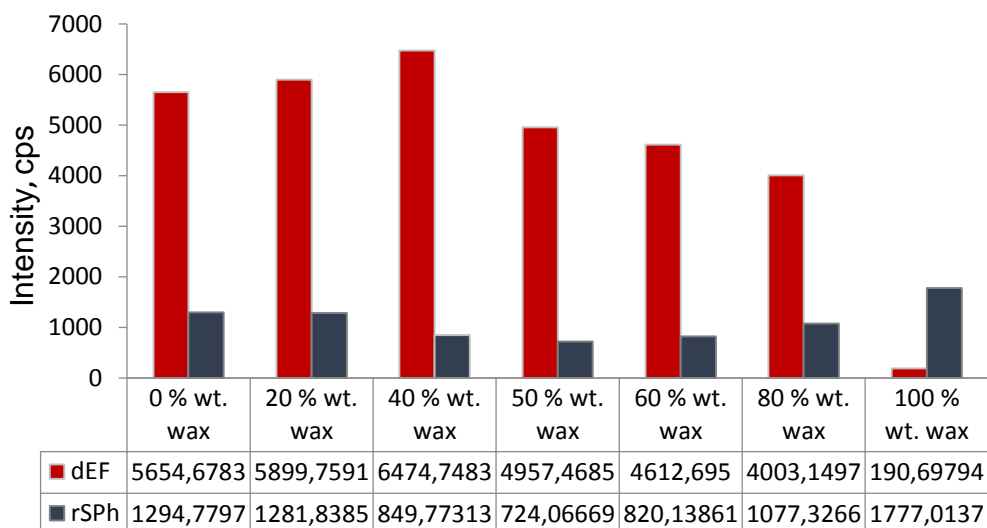


Figure 5.9 - The efficiency of dEF- and rSPh-signals in dependence on solid-liquid lipid ratio in the matrix core composition of UC-SLNPs. Experimental conditions are the same as in Figure 5.8.

The rSPh process shows the opposite trend. An increase of the wax content up to 50 wt.% of matrix core composition causes a decrease in the efficiency of the rSPh process. The subsequent increase of the solid lipid part in the matrix core composition induces an increase in the intensity of the rSPh process. The optimal matrix core composition was determined to be 40 wt.% solid / 60 wt.% liquid lipid.

5.5.3 Oxygen sensitivity of UC-SLNPs

The organic UC-SLNPs demonstrate a high sensitivity to the oxygen content in an environment. This phenomenon results from the dependence of the TTA-UC process on oxygen.¹⁸¹ Molecular oxygen readily quenches the triplet states of sensitizer and annihilator. It leads to a significantly reduced efficiency of the TTA-UC process and singlet oxygen generation. One of the effective ways to significantly reduce the quenching of the

triplet states by oxygen is the use of antioxidant activity of organic components in the UC-samples.

UC-SLNPs consisting of PdTBP / BCP in RBO 60 wt.% / carnauba wax 40 wt.% / Tween-20 were investigated for oxygen sensitivity evaluation. The UCNPs are kept at different relative oxygen content environments: at ambient conditions (21% of O₂) and oxygen-free environment (4 ppm of O₂). The oxygen sensitivity results of UCNPs clearly show, that the rSPh process in oxygen-free sample turns on instantly compared to the process with the oxygenated sample (Figure 5.10). The delay time of phosphorescence corresponds to an oxygen concentration in the sample environment. Delay time of rSPh for oxygenated UC-SLNPs is 18.53 s at intensity excitation $I_{exc} = 20 \text{ mW cm}^{-2}$. The decrease of the oxygen content in an UC-SLNPs environment leads to a decrease of the delay time of rSPh.

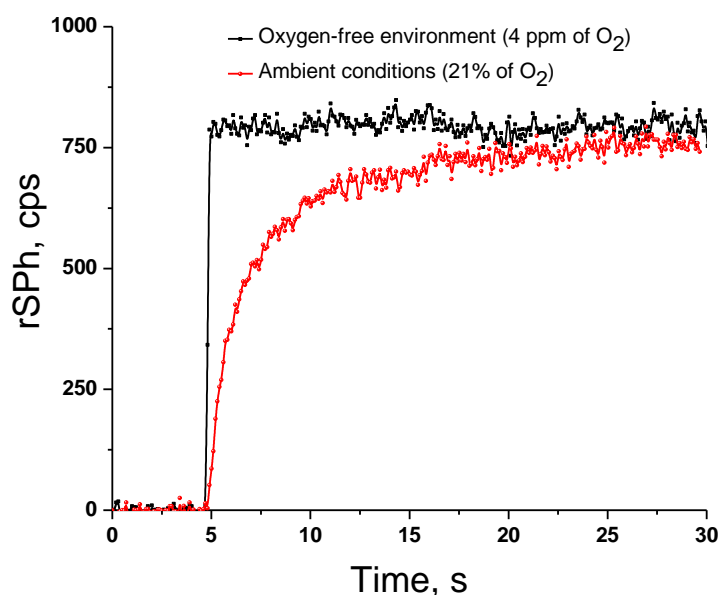


Figure 5.10 - Temporal dependence at maximum of rSPh-signal ($\lambda = 797 \text{ nm}$) for UC-SLNPs consisting PdTBP / BCP in RBO 60 wt.% / carnauba wax 40 wt.% / Tween-20 under ambient and oxygen-free environment (4 ppm).

The oxygen sensing technology relies on the diffusion of the molecular oxygen dissolved in the cell plasma/lymphatic liquid. The O₂-optical signal is created by optically-stimulated generation of singlet oxygen (dissolved now in the NPs) and consequent chemical binding of the singlet oxygen.

The equilibrium concentration between the oxygen dissolved in the continuous phase and the oxygen dissolved in the dispersed phase is reached only for very long interaction times. In order to ensure the applicability of the developed O₂-sensing technology, an example of continuous phase/dispersed phase oxygen diffusion was characterized. The UC-SLNPs consequently transferred from an ambient conditions to an engineered oxygen-containing environment. The core material composition consists of PdTBP / BCP in RBO 60 wt.% / carnauba wax 39.4 wt.% / OME-PEG₃₅₀ 0.6 wt.% / Tween-80.

The dynamical properties of the dEF- and rSPh-signals are shown in Figure 5.11 and Figure 5.12. The UC-SLNPs composition demonstrates a strongly monotonic decrease of the dEF rise time by the decrease of the oxygen concentration among the continuous phase. This allows us to create a non-ambitious calibration curve for the oxygen content at the continuous phase using as a measurable value the rise time of the rSPh-signal, excited in the TTA-UC regime. The calibration curve is shown in Figure 5.13.

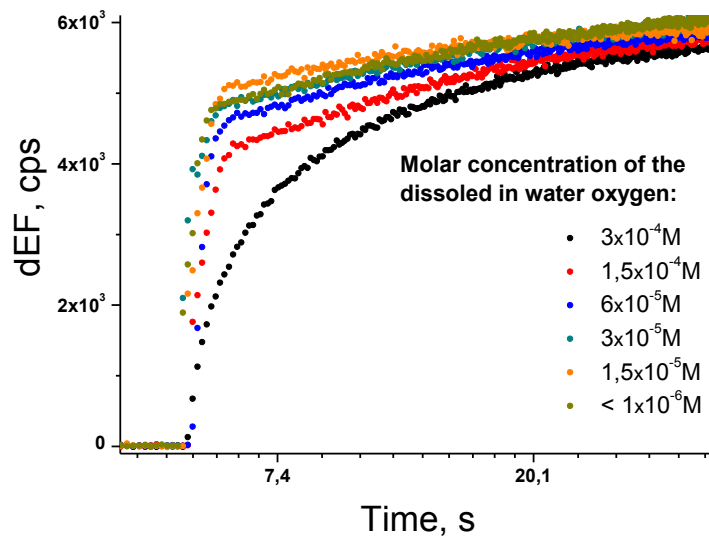


Figure 5.11 - Dynamical properties of the dEF-signal (at $\lambda_{\max}=521$ nm) for different oxygen concentrations at the continuous phase (indicated at the Figure). Conditions: water suspension (5 wt.% disperse phase); neat NC-batch, used 1 h after preparation; equilibration time = 1 h; sample isolated from ambient atmosphere; room T ; acquisition time $t_{AQ} = 100$ ms; $\lambda_{exc} = 635$ nm; excitation spot diameter $d = 890$ μm ; excitation intensity = 8 mWcm^{-2} . Optical data are obtained only for the duration of the excitation pulse $t = 40$ s.

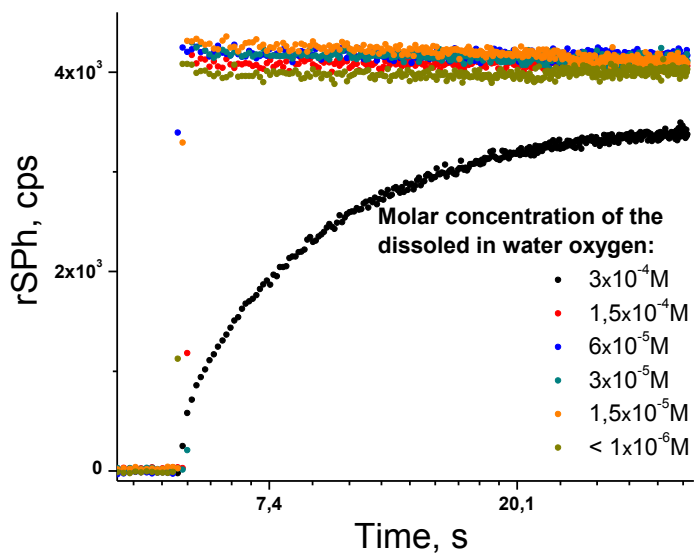


Figure 5.12 - Dynamical properties of the rSPH signal (at $\lambda_{max}=796$ nm) for different oxygen concentration at the continuous phase (indicated at the Figure). Experimental conditions are the same as in Figure 5.11.

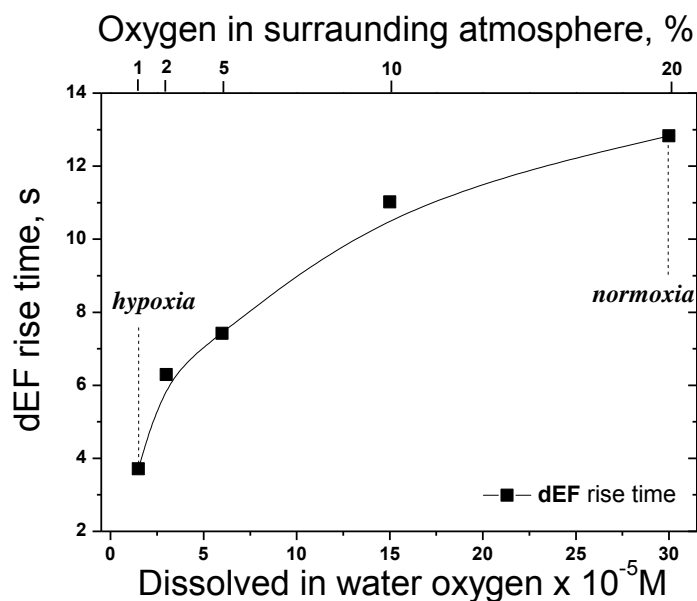


Figure 5.13 - The dependence of the rise time of dEF (at $\lambda_{max}=520$ nm) on the oxygen concentration in the continuous phase (indicated in the Figure) for the O_2 – sensing NC, described in Figure 5.11.

It is possible to measure the oxygen content in a water environment for biologically-relevant oxygen concentrations from the normoxia up to the hypoxia regime as shown in Figure 5.13.

5.5.4 Temperature sensitivity of UC-SLNPs

The temperature sensing method is carried out by the ratiometric type of signal registration. The study of the temperature sensitivity was conducted by using the UC-SLNPs with the optimal matrix composition of the solid-liquid lipid ratio.

The UC-SLNPs containing beeswax do not show an optimal T-sensing behavior as demonstrated in Figure 5.14 and 5.15. The dEF- and rSPh-signals decrease with increasing the sample temperature. That is why beeswax is not used for the next optimization steps of NP-matrix composition.

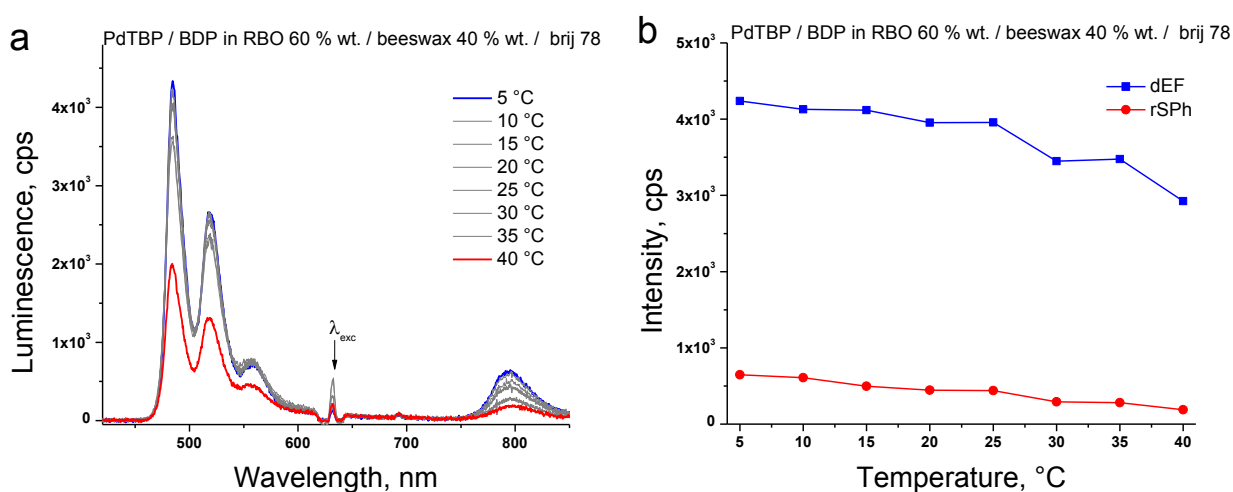


Figure 5.14 - (a) Luminescence spectra of UC-SLNPs consisting of PdTBP / BDP in RBO 60 wt.% / beeswax 40 wt.% / Brij-78 for different sample temperatures. (b) Temperature dependence of the signals of dEF (at $\lambda_{max} = 521$ nm) and rSPh (at $\lambda_{max} = 796$ nm) on the sample temperature, obtained at $t = 100$ s after the start of the continuous optical excitation. Experimental conditions: $\lambda_{exc} = 635$ nm; an air saturated environment; a temperature window: $\Delta T = 5$ °C – 45 °C; the spectra are obtained at $t = 100$ s after the start of the continuous optical excitation.

The beeswax was exchanged to the good working core-material – carnauba wax. All the other material parameters were kept unchanged. The T-sensing with the studied UC-SLNPs (PdTBP / BDP in RBO 60 wt.% / beeswax 40 wt.% / Brij-78) is shown in Figures 5.16, 5.17 and 5.18.

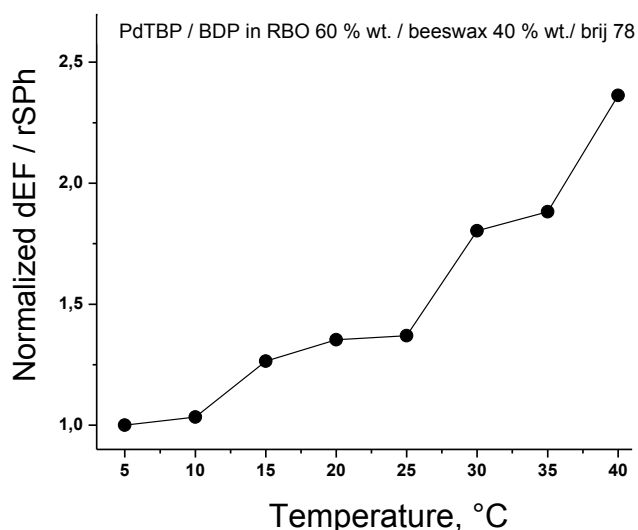


Figure 5.15 – The temperature dependence of the normalized ratio of maximal intensity of dEF-signal to maximal intensity of rSPh-signal of UC-SLNPs consisting of PdTBTP / BDP in RBO 60 wt.% / beeswax 40 wt.% / Brij-78 at observation time: $t = 100$ s.

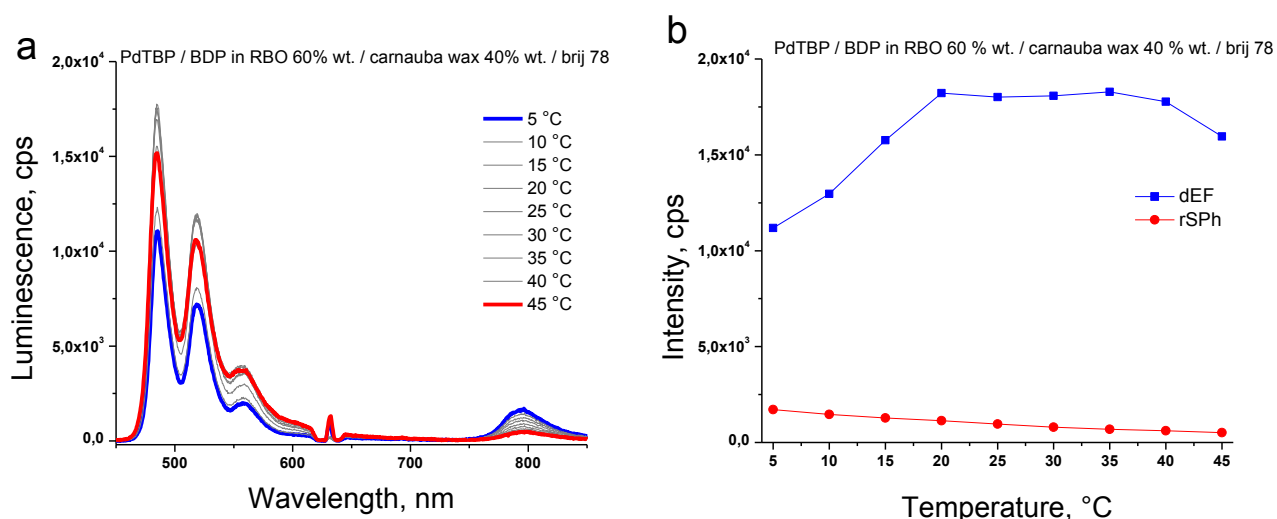


Figure 5.16 - (a) Luminescence spectra of UC-SLNPs consisting PdTBTP / BDP in RBO 60 wt.% / carnauba wax 40 wt.% / Brij-78 for different sample temperatures. (b) Temperature dependence of the signals of dEF (at $\lambda_{max} = 521$ nm) and rSPh (at $\lambda_{max} = 796$ nm) on the sample temperature, obtained at $t = 100$ s after the start of the continuous optical excitation. Experimental conditions are the same as in Figure 5.14.

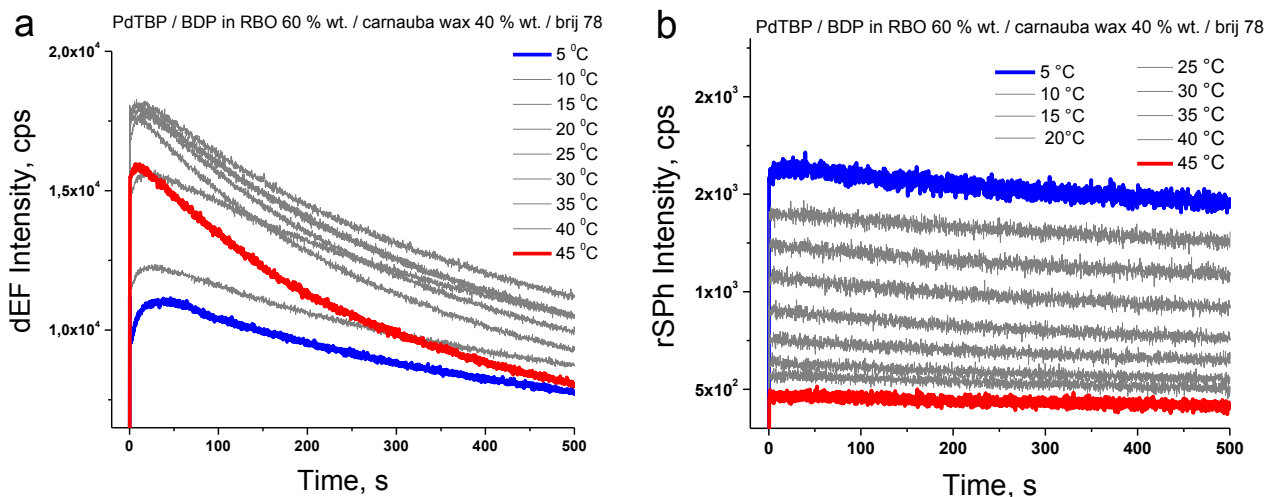


Figure 5.17 - Temporal evolution of the dependence of the dEF-signal (a) and rSPh-signal (b) on the sample temperature for UC-SLNPs consisting of PdTBP / BDP in RBO 60 wt.% / carnauba wax 40 wt.% / Brij-78. Experimental conditions are the same as in Figure 5.14.

Two negative characteristics are observed: low T-sensing performance and relative low sustainability of the dEF- and rSPh-kinetics. The experiments performed with fully hydrophobic emitter molecule BDP demonstrate low T-sensing behavior. It was decided to perform all the following experiments with the partially amphiphile emitter molecule – BCP.

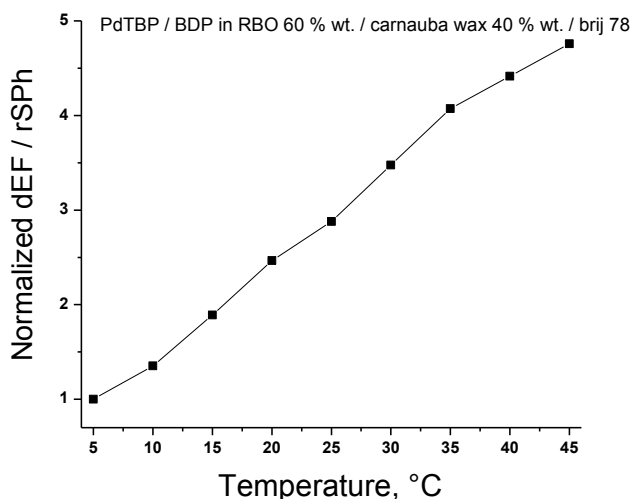


Figure 5.18 – The temperature dependence of the normalized ratio of maximal intensity of dEF-signal to maximal intensity of rSPh-signal of UC-SLNPs consisting of PdTBP / BDP in RBO 60 wt.% / carnauba wax 40 wt.% / Brij-78 at observation time: $t = 100$ s.

The UC-SLNPs composition PdTBP / BCP in RBO 60 wt.% / carnauba wax 40 wt.% / Tween-20 demonstrates high T-sensitivity, the ratio dEF / rSPh is changed 15 times within

the temperature window of interest $\Delta T = 5\text{ }^{\circ}\text{C} - 45\text{ }^{\circ}\text{C}$ (Figure 5.19). The specific behavior of the TTA-UC process was observed. The dEF-signal monotonically grows and the rSPH-signal monotonically decreases with increasing the sample temperature. The core composition was modified by the addition of small amounts ($\sim 0.6\text{ wt.}\%$) of the amphiphilic emollient OMe-PEG₃₅₀ (Figure 5.20).

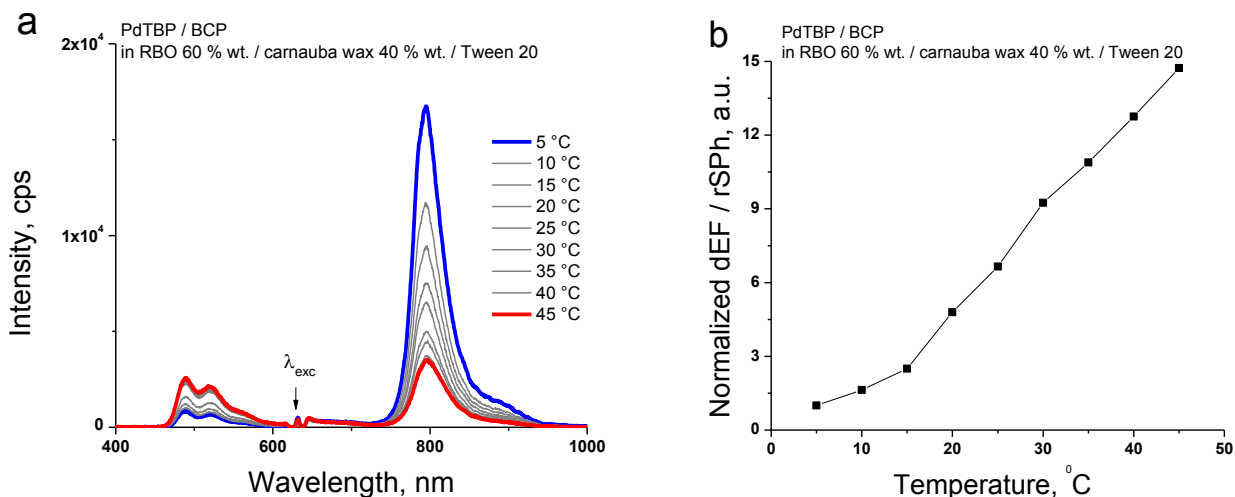


Figure 5.19 – (a) Luminescence spectra of UC-SLNPs consisting of PdTBP / BCP in RBO 60 wt.% / carnauba wax 40 wt.% / Tween-20 for different sample temperatures. (b) Normalization of dEF- and rSPH-parameters. Experimental conditions are the same as in Figure 5.14.

The UC-SLNPs consisting PdTBP / BCP in RBO 59.4 wt.% / carnauba wax 40 wt.% / OMe-PEG₃₅₀ 0.6 wt.% / Tween-20 demonstrate again a strongly monotonic increase of the dEF-signal by increasing the sample temperature. The T-sensitivity is significantly increased, the ratio dEF/rSPH is changed more than 20 times within the temperature window $\Delta T = 5\text{ }^{\circ}\text{C} - 45\text{ }^{\circ}\text{C}$ (Figure 5.20). This fact allows observing T-sensitivity up to 100 mK, optically achieved in ambient environment.

The same UC-SLNPs core composition (RBO 60 wt.% / carnauba wax 40 wt.% / Tween-20) in combination with a UC dye pair Y-894 / DBOV-Mes also demonstrates high T-sensitivity, the ratio dEF/rSPH is changed in 8.9 times within the temperature window of interest of $\Delta T = 5\text{ }^{\circ}\text{C} - 45\text{ }^{\circ}\text{C}$ (Figure 5.21). The dEF- and rSPH-signals of the UC-SLNPs (Y-894 / DBOV-Mes in RBO 60 wt.% / carnauba wax 40 wt.% / Tween-20) demonstrate high stability of dEF- and rSPH-kinetics due to singlet oxygen scavenging properties of the core material (Figure 5.22).

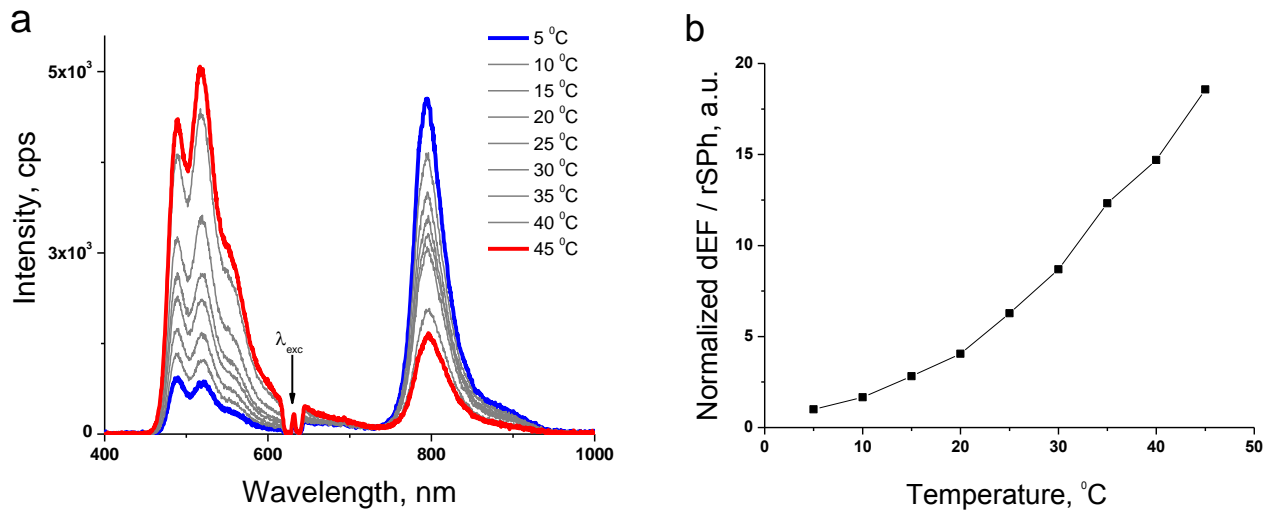


Figure 5.20 - Luminescence spectra of UC-SLNPs consisting of PdTBP / BCP in RBO 59.4 wt.% / carnauba wax 40 wt.% / OMe-PEG₃₅₀ 0.6 wt.% / Tween-20 for different sample temperatures. (b) Normalization of dEF- and rSPh-parameters. Experimental conditions are the same as in Figure 5.14.

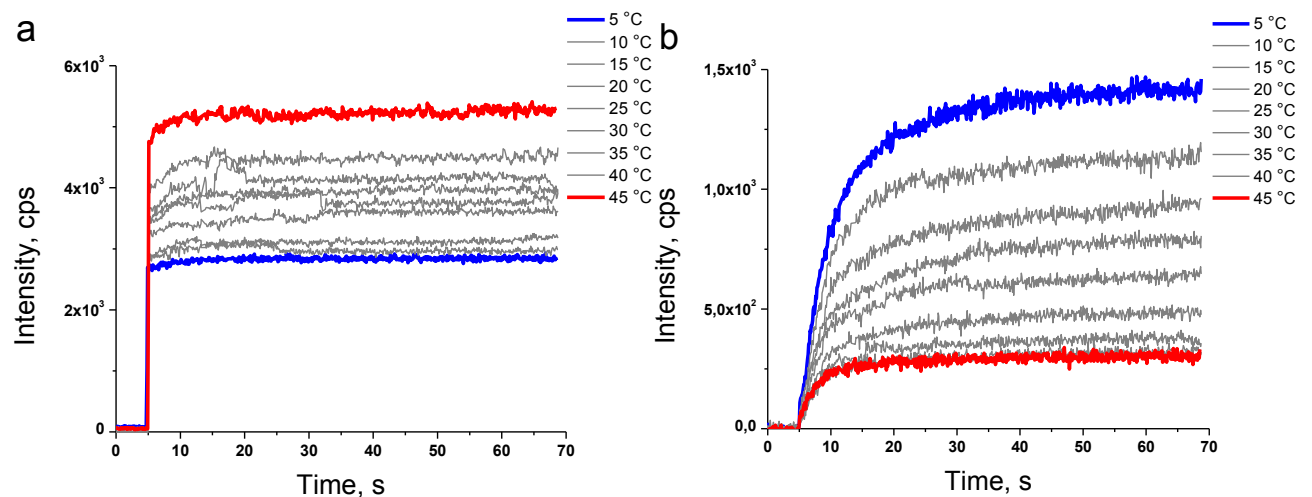


Figure 5.21 – (a) Luminescence spectra of UC-SLNPs. (b) Temperature dependence of the normalized ratio of maximal intensity of dEF signal to maximal intensity of residual rSPh of UC-SLNPs. Core material composition: Y-894 / DBOV-Mes in RBO 60 wt.% / carnauba wax 40 wt.% / Tween-20. Conditions: continuous optical excitation at $\lambda_{exc} = 658$ nm in air saturated environment; the other experimental conditions are the same as in Figure 5.14.

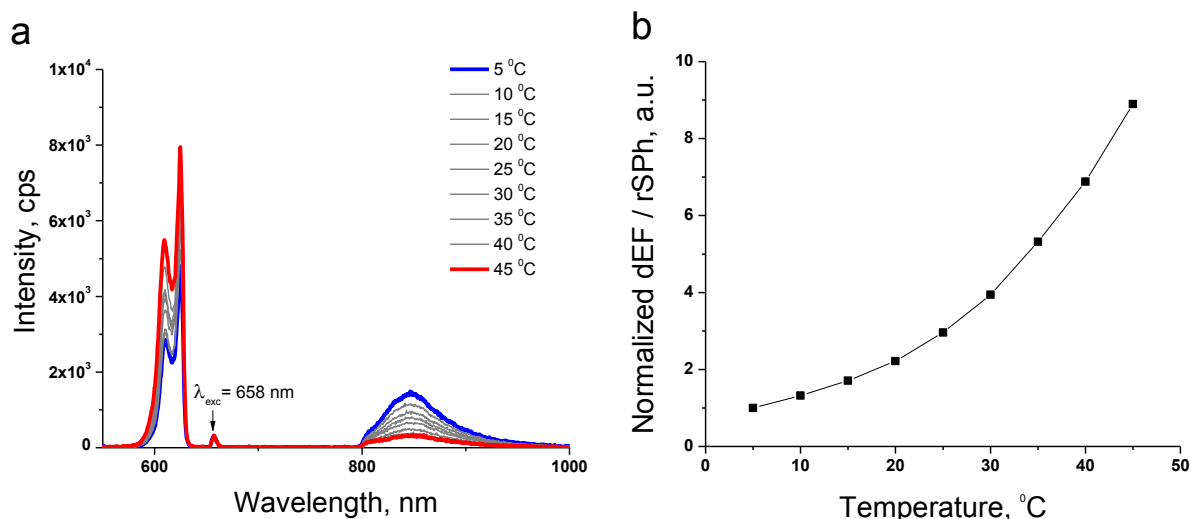


Figure 5.22 – Temporal evolution of the dependence of the dEF (at $\lambda_{max} = 609$ nm) (a) and rSPh (at $\lambda_{max} = 849$ nm) (b) signals on the sample temperature of UC-SLNPs. Experimental conditions are the same as in Figure 5.14.

The powerful antioxidant compound squalene was used for the next NP-core material optimization step. Squalene was included in the core matrix composition in the amount of 30 wt.%, RBO part was decreased from 60 wt.% to 30 wt.%, and carnauba wax part was kept constant (Figure 5.23).

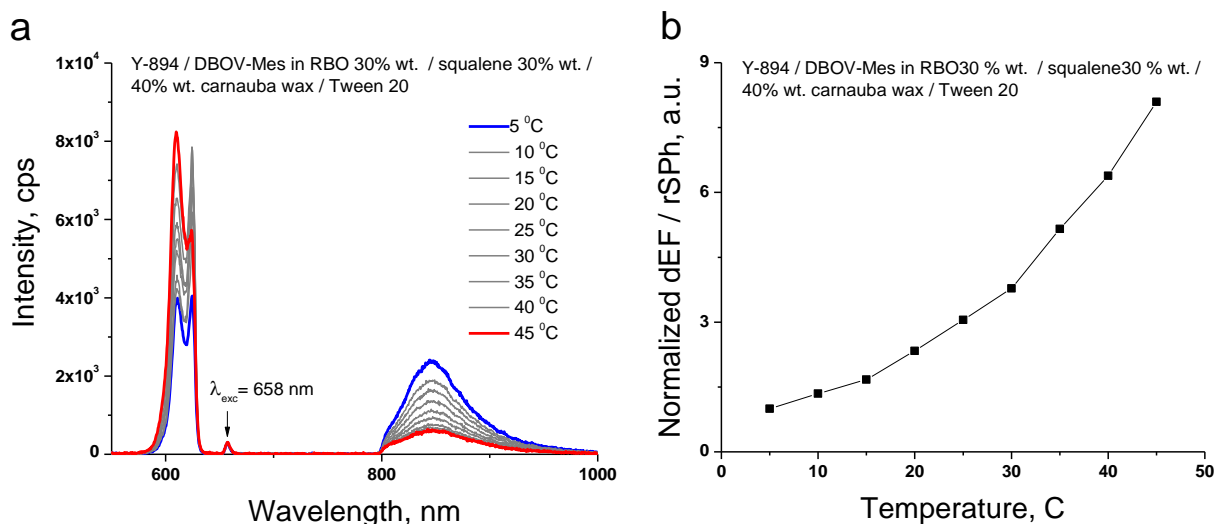


Figure 5.23 – (a) Luminescence spectra of UC-SLNPs. (b) Temperature dependence of the normalized ratio of maximal intensity of dEF signal to maximal intensity of residual rSPh of UC-SLNPs. Core material composition: Y-894 / DBOV-Mes in RBO 30 wt.% / squalene 30 wt.% / carnauba wax 40 wt.% / Tween-20. Conditions: continuous optical excitation at $\lambda_{exc} = 658$ nm in air saturated environment; the other experimental conditions are the same as in Figure 5.14.

The efficiency of the dEF- and rSPh-signals for UC-SLNPs with a core composition Y-894 / DBOV-Mes in RBO 30 wt.% / squalene 30 wt.% / carnauba wax 40 wt.% / Tween-

20 is higher than the efficiency of the parameters for UC-SLNPs without squalene in the core composition (Figure 5.23). The following normalization procedure of the parameters offsets the impact (Figure 5.23 (b)). The positive effect of the squalene content in the core matrix composition is the stability of the dEF- and rSPh-signals (Figure 5.24).

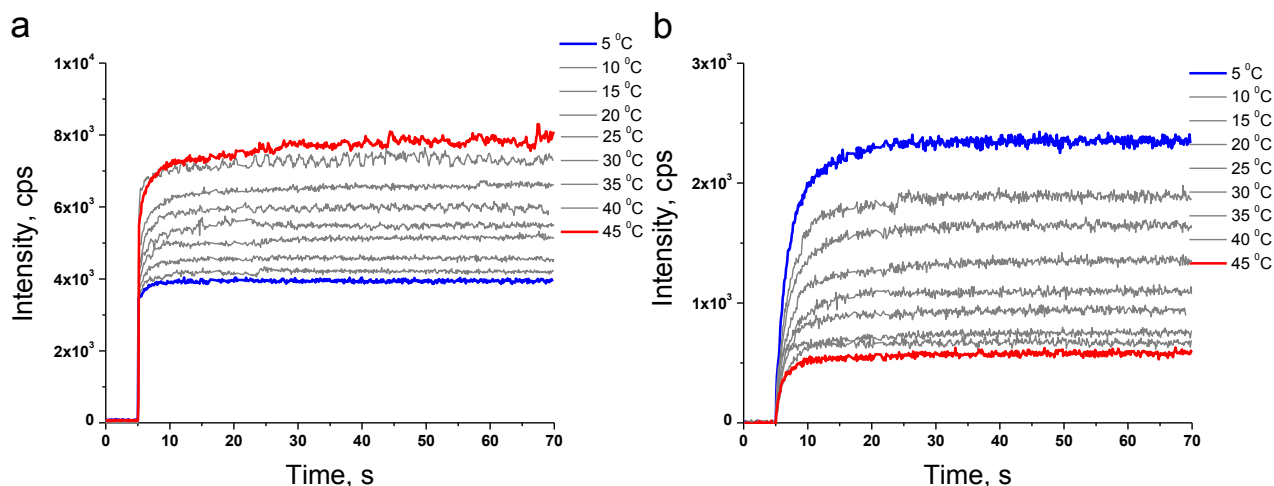


Figure 5.24 – Temporal evolution of the dependence of the dEF (at $\lambda_{max} = 609$ nm) (a) and the rSPh (at $\lambda_{max} = 849$ nm) (b) signals on the sample temperature of UC-SLNPs. Experimental conditions are the same as in Figure 5.14.

A few core matrix compositions possessing strong temperature sensitivity were found during the complex optimization procedure of the UC-SLNPs. The selected core matrix materials had very low optical absorption in the red and deep-red optical region. Thus the possible optical cross-talk of the T-sensing and O₂-sensing processes were avoided. The core matrix composition demonstrates significant sacrificial singlet oxygen scavenging properties allowing long-term operation of the T-sensors in ambient environment.

5.6 Cytotoxicity studies of UC-SLNPs

5.6.1 Cytotoxicity test of surfactants

Evaluation of the used surfactants cytotoxicity, namely Brij-78, GAET, TX-100, Tween-20 and Tween-80, was tested as the next step for UC-SLNPs composition optimization. HeLa cell line was used as a test culture system. MTS assay was used to determine cell

viability and cytotoxicity. Surfactants with different concentrations were incubated with living cells for 24 h. The cell viability was recorded to judge the toxicity of the surfactants (Figure 5.25). The exact values of the cytotoxicity results are represented in Table 5.2.

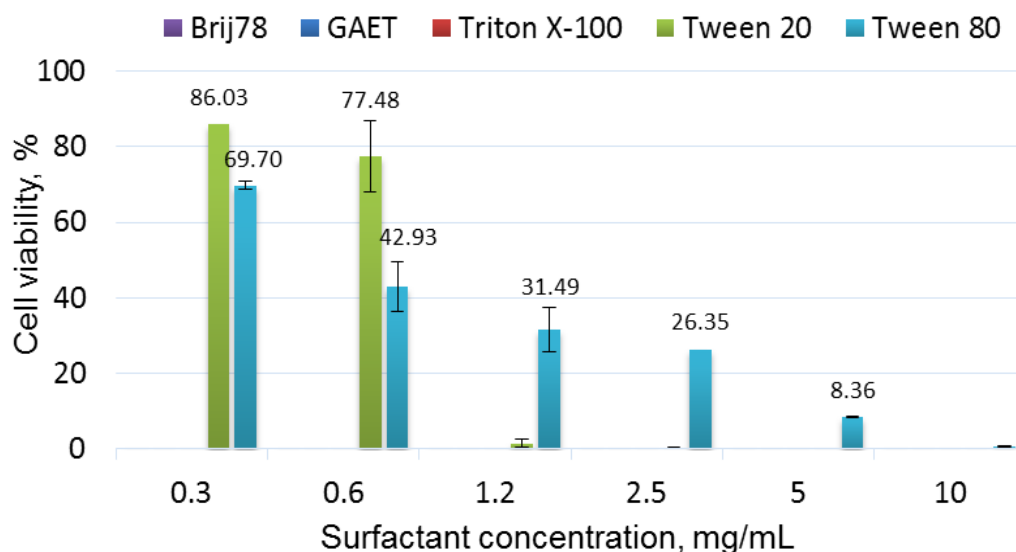


Figure 5.25 - Cytotoxicity test of the surfactants Brij-78, GAET, TX-100, Tween-20, and Tween-80 at different concentrations on HeLa cell culture. Each type of surfactants is indicated by its own color in the Figure.

Table 5.2 - Cytotoxicity results for different surfactants. SD - standard deviation.

mg/mL	Brij78		GAET		TritonX 100		Tween 20		Tween 80	
	Mean	SD	Mean	SD	Mean	SD	Mean	SD	Mean	SD
0	100,00	6,8	100,00	6,8	100,00	6,8	100,00	6,8	100,00	6,8
0,3	0,12	0,0	0,13	0,0	0,18	0,1	86,03		69,70	1,0
0,6	0,21	0,1	0,21	0,0	0,28	0,0	77,48	9,5	42,93	6,7
1,2	0,25	0,1	0,14	0,1	0,16	0,0	1,48	1,1	31,49	5,9
2,5	0,16	0,0	0,10	0,0	0,11	0,1	0,30	0,1	26,35	
5	0,12	0,0	0,03	0,0	0,06	0,0	0,20	0,1	8,36	0,2
10	0,06	0,0	0,03	0,0	0,03	0,0	0,06	0,0	0,55	0,2

The surfactants Tween-80 and Tween-20 demonstrate acceptable toxicity as shown in Figure 5.25. The gradual increase of Tween-80 and Tween-20 concentration from 0.3 up to 1.2 mg·mL⁻¹ causes a noticeable decrease of HeLa cell viability. All other surfactants are too toxic to HeLa cells. Therefore, they are not used for the following optimization steps.

5.6.2 Definition of the upper limit of cytotoxic concentration of UC-SLNPs

For the definition of the upper permissible limit of the cytotoxic concentration of UC-SLNPs it is necessary to consider next parameters: (i) acceptable level of the UC-SLNPs toxicity, (ii) intensity of the optical signals registered (dEF and rSPH) and (iii) sensitivity of the signals to the small changes of the local cell cytoplasm temperature and cytoplasm oxygen concentration. The acceptable cytotoxicity of the UC-SLNPs depends on the concentration of the UC-SLNPs (solid content of the NP-dispersion) and the total load of optically active dyes into the UC-SLNPs.

The upper limit of solid content of the UC-SLNP (PdTBP / BCP / RBO 60 wt.% / carnauba wax 40 wt.% / Tween-20 or Tween-80) dispersion is defined (optimization step (i)) (Figure 5.26 and Figure 5.27). It can be seen from the results shown in the Figure 5.26, that UC-SLNPs solid content up to $150 \mu\text{g}\cdot\text{mL}^{-1}$ shows acceptably low toxicity. Since the intensity of the dEF- and rSPH- signals are relatively low, the solid content of the UC-SLNPs must be further increased.

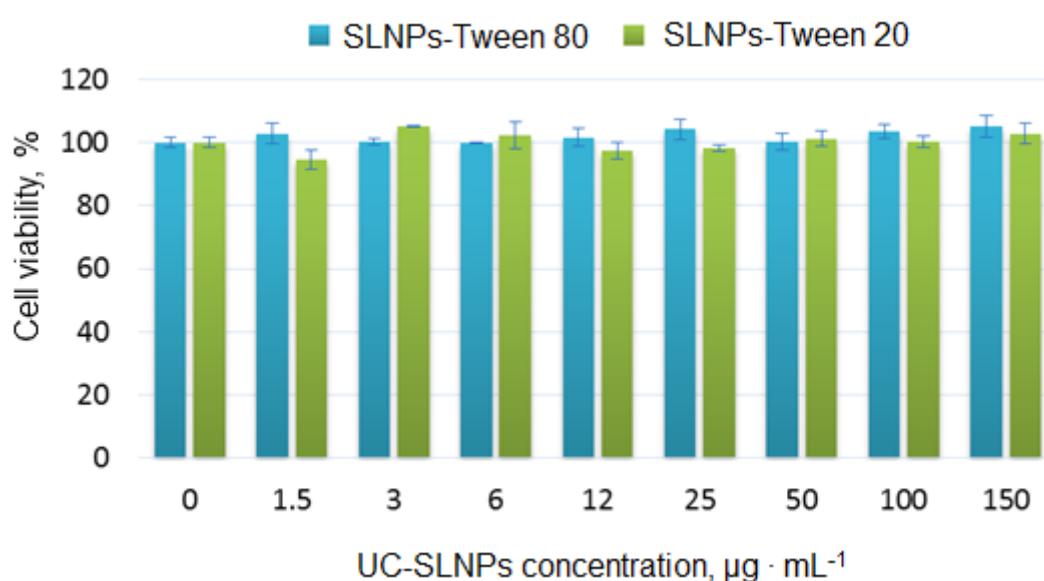


Figure 5.26 - Cytotoxicity evaluation of UC-SLNPs containing of PdTBP / BCP / RBO 60 wt.% / carnauba wax 40 wt.% / Tween-20 or Tween-80. Solid content ranges from $1.5 \mu\text{g}\cdot\text{mL}^{-1}$ up to $150 \mu\text{g}\cdot\text{mL}^{-1}$.

The cell viability assays demonstrate that cells remain viable after 24 h incubation with UC-SLNPs with concentration up to $1250 \mu\text{g}\cdot\text{mL}^{-1}$ (Figure 5.27). Further increasing of the incubation concentration of UC-SLNPs leads to the death of a significant part of the cell

culture. The survival rates (from Figure 5.27) for the UC-SLNPs loading are shown in Table 5.3. However, the allowable incubating concentration of UC-SLNPs allows realizing the desired optical sensing functions.

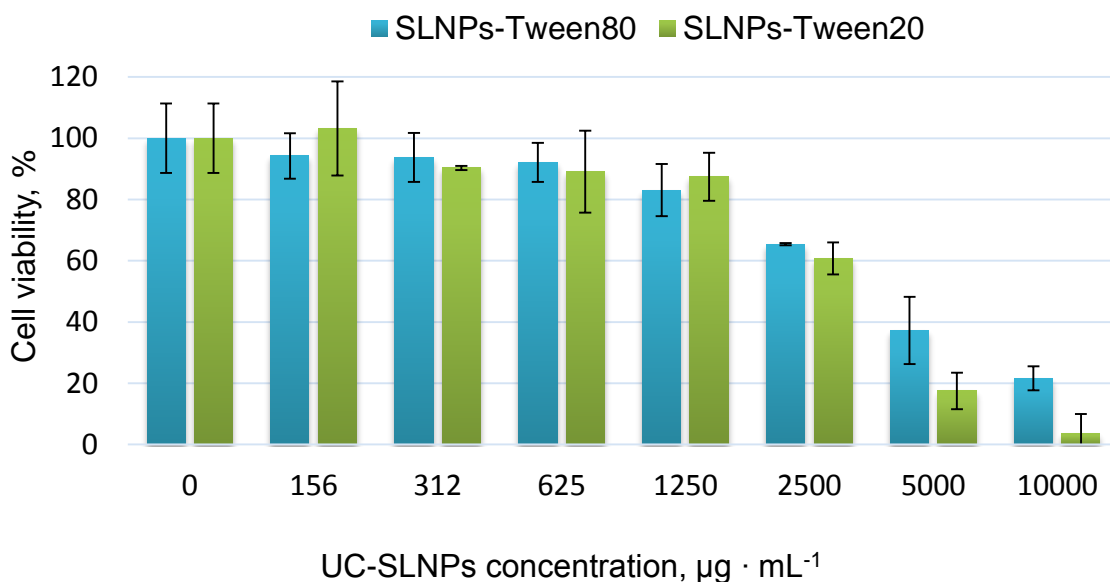


Figure 5.27 - Cytotoxicity evaluation of UC-SLNPs containing of PdTBP / BCP / RBO 60 wt.% / carnauba wax 40 wt.% / Tween-20 or Tween-80. The solid content ranges from 156 µg·mL⁻¹ up to 10,000 µg·mL⁻¹.

Table 5.3 - Cytotoxicity results for UC-SLNPs stabilized by Tween-20 and Tween-80. SD - standard deviation.

mg·mL ⁻¹	SLNPs-Tween80		SLNPs-Tween20	
	Mean	SD	Mean	SD
0	100	11.4	100	11.4
156	94	7.4	103	15.3
312	94	8.0	90	0.7
625	92	6.4	89	13.4
1250	83	8.6	87	7.9
2500	65	0.4	61	5.2
5000	37	11.0	17	6.0
10000	22	3.9	4	6.3

Both non-ionic surfactants show comparable low toxicity. Only Tween-20 was used for the further optimization steps.

In Figure 5.28 upper limit of the total load of optically active dyes into the UC-SLNPs was defined (optimization step (ii)). Two UC-SLNP core compositions were tested for cytotoxicity:

SLNP-Tween20-1: core material composition – PdTBP (6×10^{-5} M, 900 μ L) / BCP (1.4×10^{-4} M, 1800 μ L) / RBO 60 wt.% (180 mg) / carnauba wax 40 wt.% (120 mg) / Tween-20 – lower dye load;

SLNP-Tween20-2: core material composition – PdTBP (8×10^{-5} M, 900 μ L) / BCP (1.6×10^{-4} M, 1800 μ L) / RBO 60 wt.% (180 mg) / carnauba wax 40 wt.% (120 mg) / Tween-20 – higher dye load.

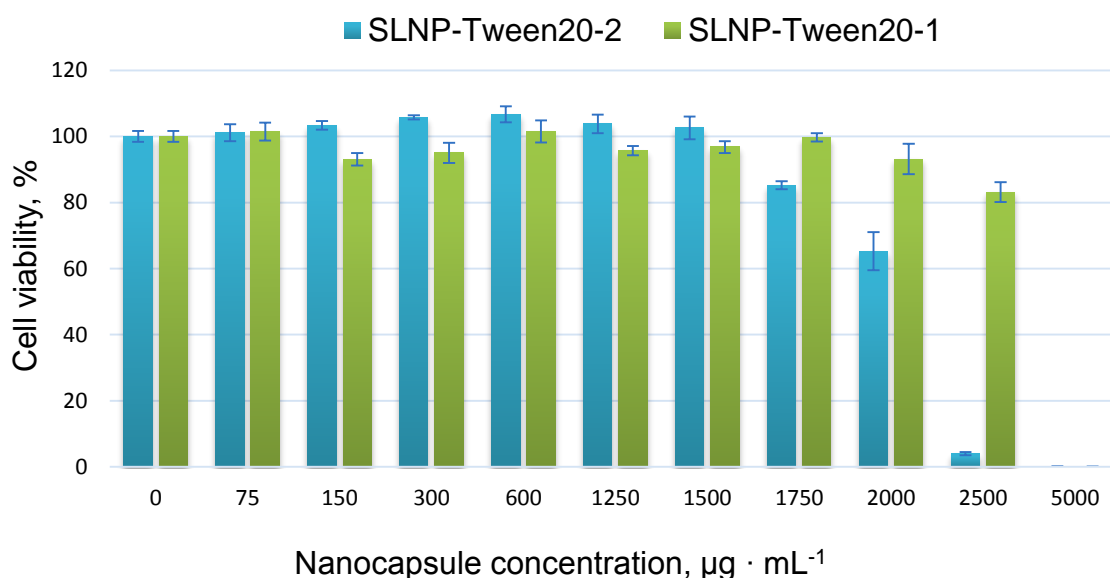


Figure 5.28 - Cytotoxicity evaluation of UC-SLNPs, containing different loadings of UC-dyes and different solid contents of the SLNP-dispersion. UC-SLNPs containing higher UC dye load (light blue), UC-SLNPs containing lower UC-dye load (light green).

An increase of the UC-dyes load leads to the decreased viability of the HeLa cells, especially for solid contents of the UC-SLNPs higher than $1500 \mu\text{g} \cdot \text{mL}^{-1}$ (Figure 5.28). The decrease of the TTA-UC dyes load leads to a significant increase in viability of the HeLa cells, keeping high viability for the solid content over $2000 \mu\text{g} \cdot \text{mL}^{-1}$.

5.6.3 Visualization of UC-SLNPs

Visualization of the UC-SLNPs taken up by HeLa cells is done in Figure 5.29. Fluorescent images of cell cultures incubated for 24 h with UC-SLNPs were obtained by confocal laser scanning microscopy. The excitation wavelengths for this confocal microscope are fixed to $\lambda_{exc} = 488$ nm; $\lambda_{exc} = 561$ nm and $\lambda_{exc} = 633$ nm. The emission spectrum of CLSM SP5 is limited to $\Delta\lambda_{ems} = 400 - 800$ nm. The UC-SLNPs composition for this study is as follows: PdTBP (10^{-4} M, 900 μ L) / BCP (10^{-3} M, 1800 μ L) / RBO 60 wt.% / carnauba wax 40 wt.% / Tween-20. The concentration of the TTA-UC sensing dyes was increased 6 times, in order to ensure good visualization of the UC-SLNPs in the HeLa cells.

For visualization of the cytoplasm membrane, the lipophilic dye CellMask™ Orange (ThermoFisher Scientific GmbH) was used. This dye has a small emission Stokes-shift. The strong fluorescence at $\Delta\lambda_{ems} = 570-600$ nm can be observed by excitation at $\lambda_{exc} = 561$ nm. The anthraquinone dye DRAQ5™ (ThermoFisher Scientific GmbH) with the high affinity for double-stranded DNA was used for imaging of the cell-nucleus. This is a membrane-permeable dye, that can label live cells. Since its emission demonstrates a relative large Stokes-shift, where the excitation wavelength is $\lambda_{exc} = 646$ nm and $\lambda_{ems} = 697$ nm, it was used as a nuclear counterstain.

The CLSM-image of HeLa cell with UC-SLNPs, excited with $\lambda_{exc} = 488$ nm, is demonstrated in emission window $\Delta\lambda_{ems} = 510-540$ nm, BCP emission ($\Delta\lambda_{ems} = 510-540$ nm coincides with the fluorescent spectrum of the emitter dye BCP). The CLSM-image of HeLa cell with UC-SLNPs, excited with $\lambda_{exc} = 561$ nm, is visualizes in emission window $\Delta\lambda_{ems} = 570-600$ nm, cytoplasm membrane ($\Delta\lambda_{ems} = 570-600$ nm coincides with the fluorescent spectrum of the CellMask™ Orange). The CLSM-image of HeLa cells with UC-SLNPs, excited with $\lambda_{exc} = 633$ nm, is visualized in the emission window $\Delta\lambda_{ems} = 650-710$ nm, cell-nucleus and PdTBP emission ($\Delta\lambda_{ems} = 650-710$ nm) coincides with the fluorescent spectra of the DRAQ5 and rSPh-signal of the sensitizer dye PdTBP. The integral CLSM-image of the HeLa cells with UC-SLNPs clearly shows, that the UC-SLNPs taken up in the cells are comprised of both sensitizer and emitter molecules.

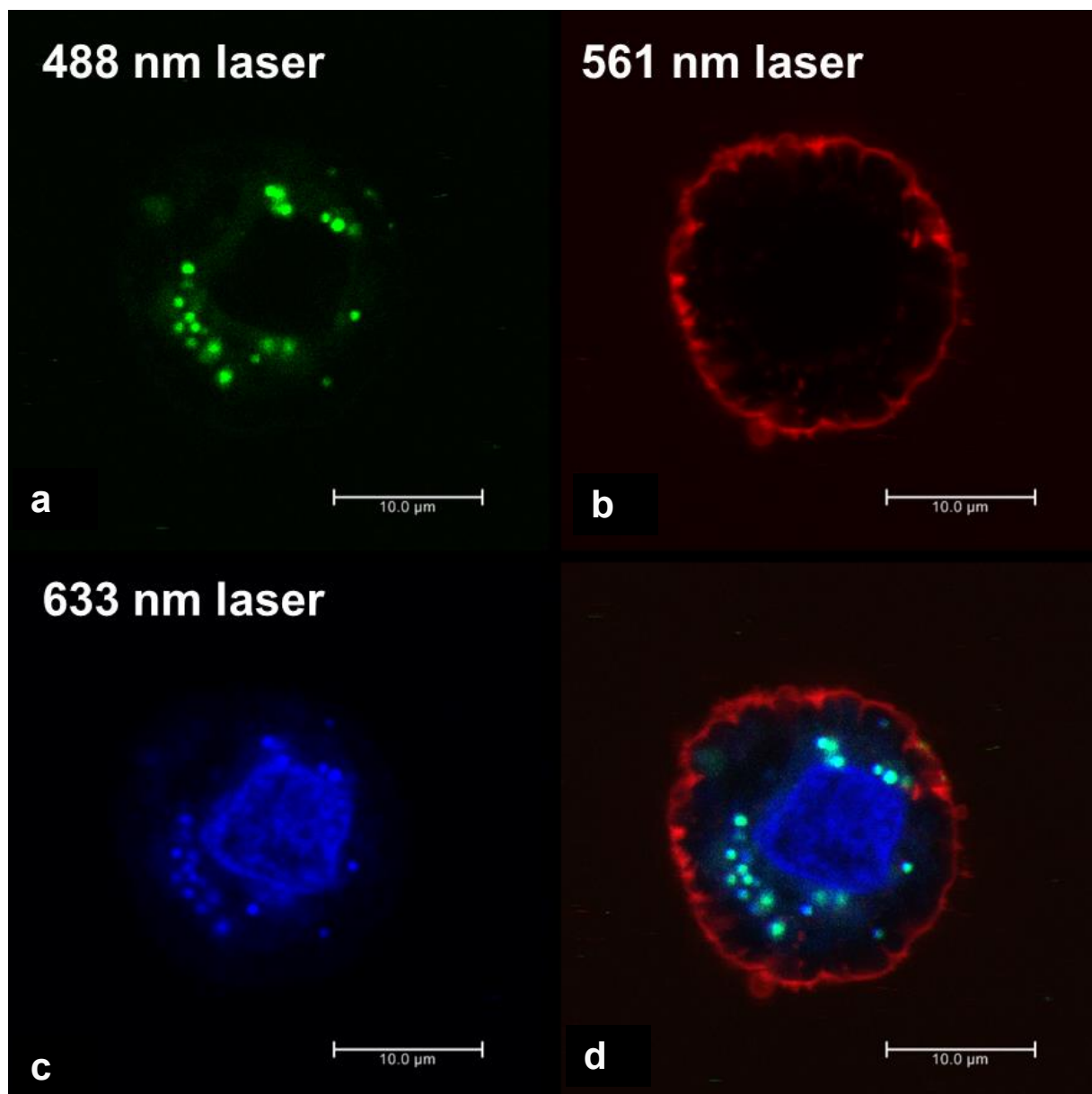


Figure 5.29 - Fluorescent images of HeLa cells incubated with UC-SLNPs (concentration $2 \text{ mg} \cdot \text{mL}^{-1}$). (a) A CLSM-image of HeLa cell with UC-SLNPs, excited with $\lambda_{exc} = 488 \text{ nm}$. The emission window is set to $\Delta\lambda_{ems} = 510\text{-}540 \text{ nm}$. This window coincides with the fluorescent spectrum of the emitter dye BCP, part of the TTA-UC couple used. At these excitation/emission spectra no other dyes are observable. (b) A CLSM-image of HeLa cell with UC-SLNPs, excited with $\lambda_{exc} = 561 \text{ nm}$. The emission window is set to $\Delta\lambda_{ems} = 570\text{-}600 \text{ nm}$. This window coincides with the fluorescent spectrum of the dye staining the cytoplasm membrane (CellMask™ Orange). (c) A CLSM-image of HeLa cell with UC-SLNPs, excited with $\lambda_{exc} = 633 \text{ nm}$. The emission window is set to $\Delta\lambda_{ems} = 650\text{-}710 \text{ nm}$. This window coincides with the fluorescent spectrum of the dye staining the cell-nucleus, (DRAQ5) and the residual phosphorescence of the sensitizer dye PdTBP, part of the TTA-UC couple used. (d) Integral CLSM-image of HeLa cell with UC-SLNPs, obtained by digital overlapping the images (a), (b) and (c). Note: The colors, used in Figure 5.29 are not through colors.

5.6.4 Uptake mechanism of UC-SLNPs by HeLa cells

Potential theranostic applications of the UC-SLNPs require precise knowledge about the interaction of NPs with the cell cultures and about uptake mechanisms by the cells. Fluorescent images of cell cultures, incubated for 0.5, 1, 4, 6, 24 h (mentioned at the Figures) with UC-SLNPs dispersion, were obtained with CLSM SP5. All images are digitally synthesized, similarly as the image from Figure 5.29 (d). The UC-SLNPs are colored in light green, the cytoplasm membrane - in red, and cell-nucleus - in blue (Figure 5.30). The time-dependent uptake of UC-SLNPs by HeLa cells is shown in Figure 5.30.

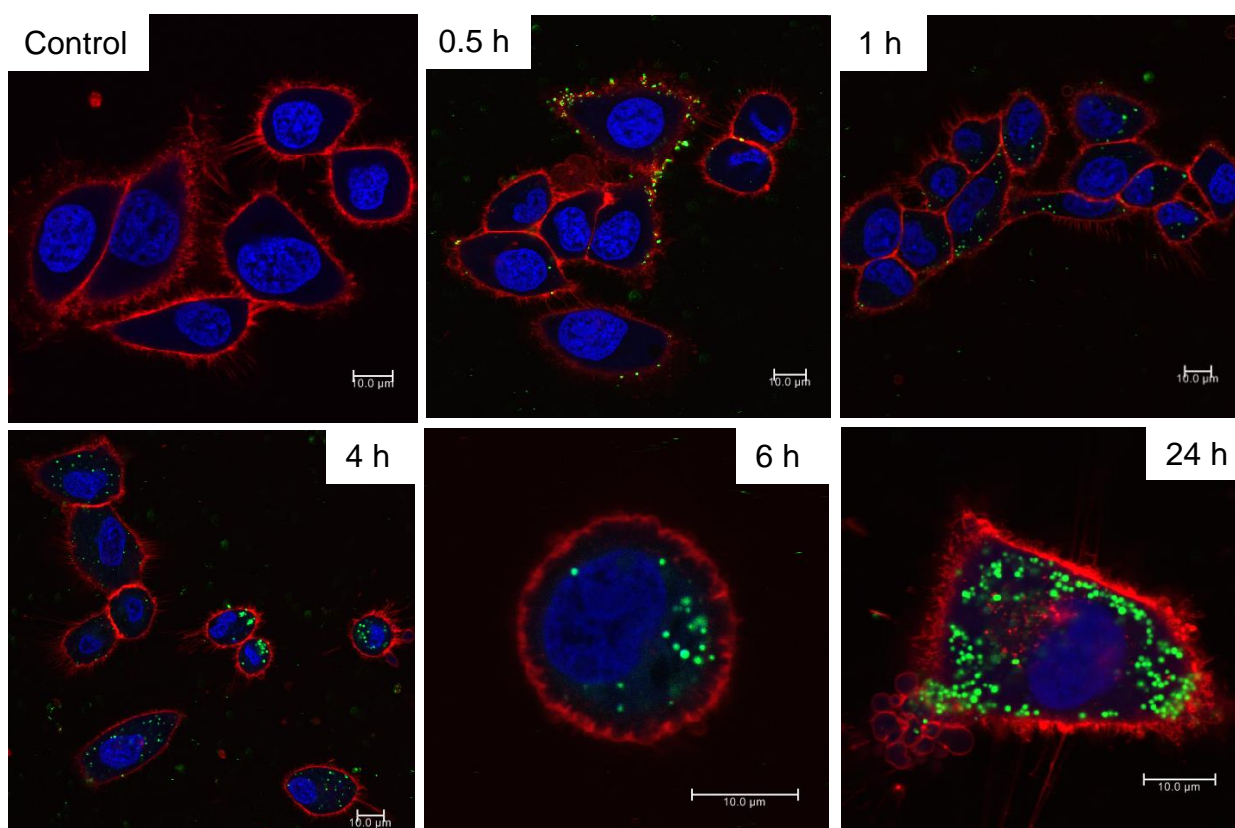


Figure 5.30 - Cellular uptake of UC-SLNPs by HeLa cells, concentration $2 \text{ mg}\cdot\text{mL}^{-1}$. UC-SLNP core composition: PdTBP (10^{-4} M , $900 \text{ }\mu\text{L}$) / BCP (10^{-3} M , $1800 \text{ }\mu\text{L}$) in RBO 60 wt.% / carnauba wax 40 wt.% / Tween-20. The different incubation times are shown in the photographs. The same excitation/emission conditions as at Figure 5.29 were used.

The cellular uptake temporal studies show that cancer cells rapidly accumulate UC-SLNPs. Gradual attachment of UC-SLNPs to a cell membrane occurs in 30 min after incubation start. Then an amount of intracellular UC-SLNPs vastly increases with rising

incubation time and in 24 h almost 100% of UC-SLNPs are accumulated by HeLa cells. It can be seen that the UC-SLNPs do not penetrate into the cell nucleus.

5.7 T-sensing in cell cytoplasm environment

5.7.1 Optimization of T-sensing system

The calibration procedure for measurement of the local temperature via T-sensing UC-SLNPs in a cell cytoplasm environment was studied next. The UC-SLNPs have a much higher load of optically active UC-dyes, in order to deliver well observable optical data even at a very strong dilution (up to 50 times, required by the cell viability tests, Figure 5.27) and lowering the effective samples thickness (up to 30 times, the used cell cultures are single-layered). The dilution and single-layer cell culture leads to a dramatic decrease in the intensity of the dEF- and rSPh-signals up to 1000 times.

Possible solutions to these severe problems can be:

- (i) The dramatic increase of the sensitizer molar concentration more than in 30 times in the UC-SLNPs (Figures 5.31 and 5.32).
- (ii) Increase of the laser excitation intensity more than 10 times in cell-sensing experiments reported below (up to 560 mW cm^{-2}). The excitation intensity will be reported explicitly for every experiment.

High load UC-SLNPs (Y-894 / DBOV-Mes in RBO 30 wt.% / carnauba wax 40 wt.% / squalene 30 wt.% / Tween-20) demonstrate high T-sensitivity (Figure 5.32). The ratio dEF / rSPh is changed more than in 9 times within the temperature window of interest of $\Delta T = 5 \text{ }^\circ\text{C} - 45 \text{ }^\circ\text{C}$. The results are comparable with the T-sensitivity obtained in paragraph 5.5.4 for this system at the optimal molecular concentration (Figures 5.23 and 5.4).

The T-sensitivity at high load is preserved. The ratio dEF / rSPh is changed more than 2.5 times within the life-science relevant temperature window of $\Delta T = 30 \text{ }^\circ\text{C} - 40 \text{ }^\circ\text{C}$. This fact allows observing a T-sensitivity up to 100 mK, optically achieved in the ambient environment. The dEF-signal increases monotonically with the sample temperature increase, simultaneously the rSPh-signal decreases monotonically with increasing the

sample temperature. Thus the non-ambiguous calibration curve is achieved (Figure 5.32 (b)).

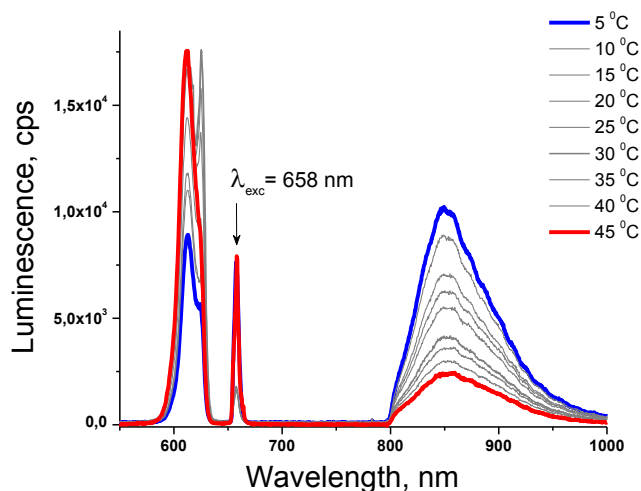


Figure 5.31 - Temperature dependence of the luminescence spectra of UC-SLNPs for different sample temperatures. Core material composition: Y-894 / DBOV-Mes in RBO 30 wt.% / squalene 30 wt.% / carnauba wax 40 wt.% / Tween-20. Conditions: water suspension of UC-SLNPs (solid content = 60 mg·mL⁻¹); sensitizer / emitter molar ratio 1:2; sensitizer / emitter load at least × 3.3 times; $\lambda_{exc} = 658$ nm; temperature window: $\Delta T = 5$ °C - 45 °C; spectra are obtained at $t = 15$ s after start of the continuous optical excitation. Samples were stored for 24 h at RT, ambient atmosphere.

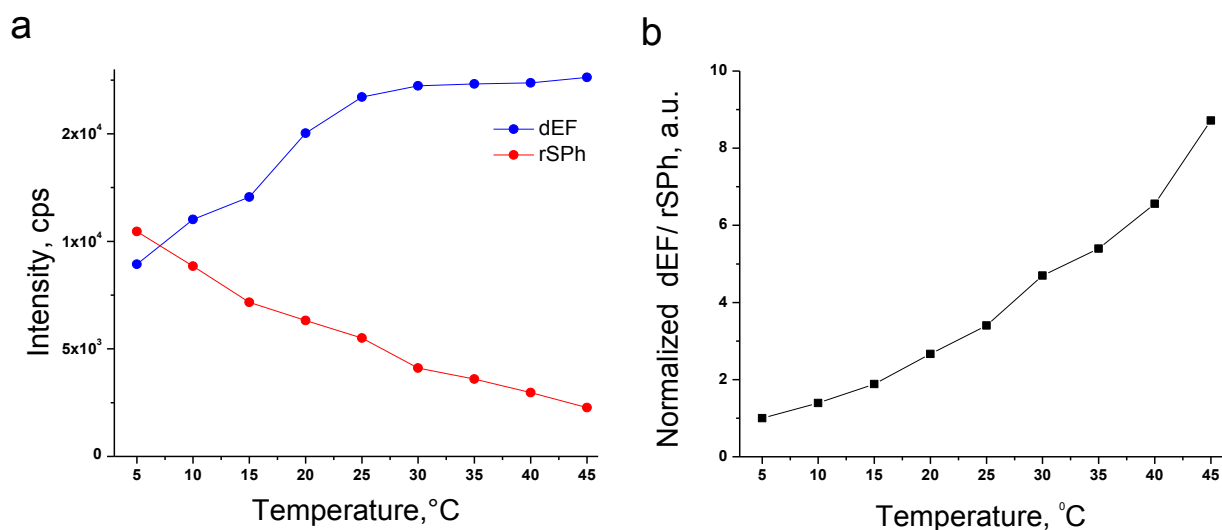


Figure 5.32 - (a) Temperature dependence of the maximal intensity of the dEF-signal (blue line) and rSPH-signal (red line). (b) Temperature dependence of the normalized ratio of maximal intensity of dEF to maximal intensity of rSPH for UC-SLNPs. Core material composition: Y-894 / DBOV-Mes in RBO 30 wt.% / squalene 30 wt.% / carnauba wax 40 wt.% / Tween-20. The experimental conditions are the same as in Figure 5.31.

The substantial dilution of the UC-SLNP dispersion up to 50 times allows to approach the sensing conditions in the cell-cytoplasm environment. The T-sensing experimental data (T-calibration curve) are obtained at $1250 \mu\text{g}\cdot\text{mL}^{-1}$ solid content, Figure 5.33.

In order to compensate the drastic loss of an optical signal, the excitation intensity is increased nearly in 14 times, reaching an excitation intensity of $560 \text{ mW}\cdot\text{cm}^{-2}$. This sensing intensity increase fulfills the crucial requirement for the sensing technique, to be minimally invasive.

The temperature sensitivity of the NPs is kept even at a drastic dilution of the UC-SLNPs dispersion (Figure 5.33). The T-calibration curve is obtained at strongly varying experimental conditions (the local concentration of UC-SLNPs, a total molecular load of the UC-SLNPs with TTA-UC sensing dyes or local (uncontrolled) variation of the excitation intensity (experimentally proven change up to 14 times)) is not significantly modified.

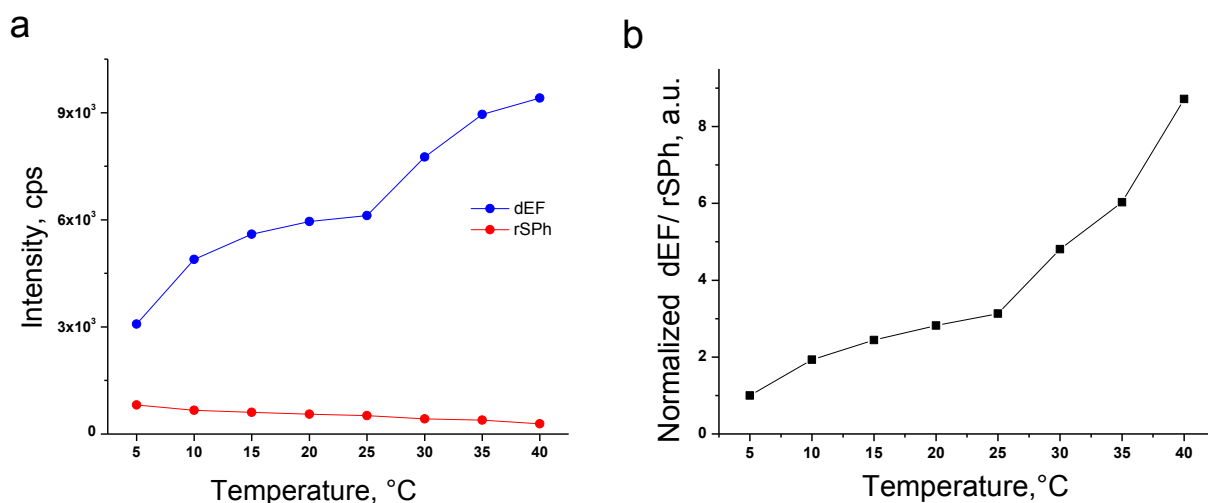


Figure 5.33 - (a) Temperature dependence of the maximal intensity of dEF-signal (blue line) and rSPh-signal (red line). (b) Temperature dependence of the normalized ratio of maximal intensity of dEF to maximal intensity of rSPh for UC-SLNPs. Core material composition: Y-894 / DBOV-Mes in RBO 30 wt.% / squalene 30 wt.% / carnauba wax 40 wt.% / Tween-20. Conditions: water suspension of UC-SLNPs, disperse phase $1250 \mu\text{g}\cdot\text{mL}^{-1}$; sensitizer / emitter molar ratio 1:2; sensitizer / emitter load at least $\times 3.3$ times; $\lambda_{\text{exc}} = 658 \text{ nm}$; temperature window: $\Delta T = 5 \text{ }^{\circ}\text{C} - 45 \text{ }^{\circ}\text{C}$; equilibration time = 1 h; sample isolated from ambient atmosphere; accumulation time 100 ms; excitation intensity = $560 \text{ mW}\cdot\text{cm}^{-2}$. Samples were stored for 24 h at RT, ambient atmosphere.

The T-sensitivity at high load is preserved. The ratio dEF / rSPh is changed more than in 1.5 times within life-science relevant temperature window: $\Delta T = 30\text{ }^{\circ}\text{C} - 40\text{ }^{\circ}\text{C}$. This fact allows observing T-sensitivity up to 150 mK, optically achieved in the ambient environment. The dEF signal increases monotonically with the sample temperature increase, simultaneously the rSPh signal decreases monotonically with the sample temperature increase. Thus the non-ambiguous calibration curve is achieved (Figure 5.33 (b)).

5.7.2 Intracellular T-sensing in HeLa cells

The following intracellular T-sensing experiments were carried out with UC-SLNPs incubated with HeLa cell line. The incubation conditions were described in detail in paragraph 5.6.4.

The temperature sensitivity of the NPs is sustained even after incubation at $37\text{ }^{\circ}\text{C}$ for 24 h and drastically decreased the sample thickness of the UC-SLNPs, taken up by HeLa cells (Figure 5.36). The dEF-signal increases monotonically (up to $30\text{ }^{\circ}\text{C}$) with the sample temperature increase, simultaneously the rSPh-signal decreases monotonically with the sample temperature increase. Thus the non-ambiguous calibration curve is achieved (Figure 5.36).

The data reported in Figure 5.37 are the first result for T-sensing in living tumor cells, based on the TTA-UC process. The T-sensitivity at high dye load, strong dilution, and drastic sample thickness reduction is sustained (the ratio dEF / rSPh is changed in more than 30% within temperature window $\Delta T = 30\text{ }^{\circ}\text{C} - 40\text{ }^{\circ}\text{C}$). This fact allows observing a T-sensitivity up to 250 mK, optically achieved in the ambient environment.

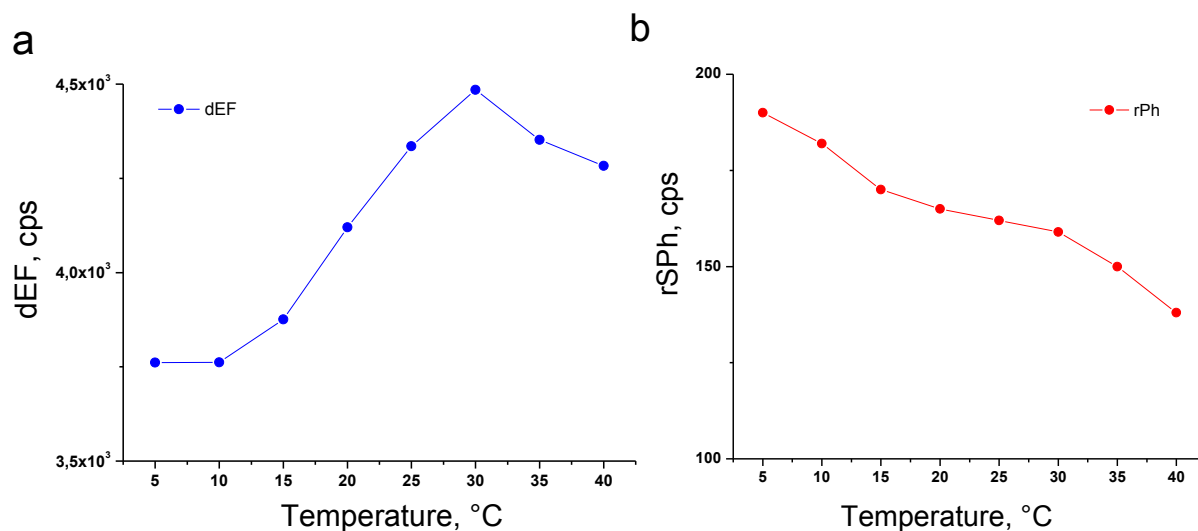


Figure 5.36 - (a) Temperature dependence of the maximal intensity of the dEF-signal and (b) Temperature dependence of the maximal intensity of rSPh-signal for UC-SLNPs, taken up by HeLa-cells. Core material composition: Y-894 / DBOV-Mes in RBO 30 wt.% / squalene 30 wt.% / carnauba wax 40 wt.% / Tween-20. Conditions: the concentration of UC-SLNPs dispersion, used for incubation with HeLa cells, is $1250 \mu\text{g}\cdot\text{mL}^{-1}$; sensitizer / emitter molar ratio 1:2; sensitizer / emitter load at least $\times 3.3$ times; $\lambda_{\text{exc}} = 658 \text{ nm}$; equilibration time = 1 h; accumulation time $t_{\text{AQ}} = 100 \text{ ms}$; excitation intensity = $560 \text{ mW}\cdot\text{cm}^{-2}$. Sample thickness $\sim 20 \mu\text{m}$; samples were incubated for 24 h at 37 °C, 95% relative humidity, 74 vol.% N₂, 20 vol.% O₂, 5 vol.% CO₂. Measured in an ambient atmosphere on top of the water phase, 21% O₂.

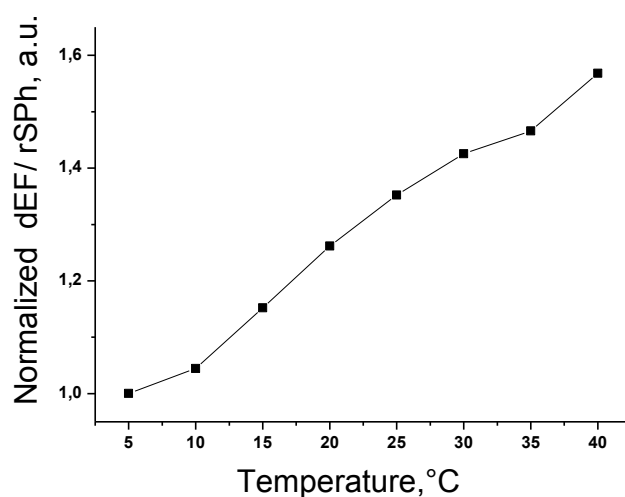


Figure 5.37 - Temperature dependence of the normalized ratio of maximal intensity of dEF to maximal intensity of rSPh for UC-SLNPs. Core material composition: Y-894 / DBOV-Mes in RBO 30 wt.%/ squalene 30 wt.%/ carnauba wax 40 wt.%/ Tween-20. The experimental conditions are the same as in Figure 5.36.

5.8 Conclusion

The complex of optimization procedures of the UC-SLNPs serving as T- and O₂-sensor was performed during this study. The selected UC-SLNPs core composition Y-894 / DBOV-Mes in RBO 30 wt.% / squalene 30 wt.% / carnauba wax 40 wt.% / Tween-20 is entirely biocompatible, consisting of natural wax, vegetable oil and pharmaceutically acceptable non-ionic surfactant. The selected sensitizer/emitter compositions demonstrate absorption/emission properties optimally matching the absorption/scattering spectra of the main tissue components of the human skin. The optimal UC-SLNPs core composition Y-894 / DBOV-Mes in RBO 30 wt.% / squalene 30 wt.% / carnauba wax 40 wt.% / Tween-20 demonstrates the monotonic increase of the dEF-signal and decrease of the rSPh-signal at monotonically increasing the sample temperature, that allows getting exclusively sustainable T-calibration curve. The obtained UC-SLNPs composition is pronounced oxygen sensitivity and demonstrates high oxygen scavenging ability. The upper limit of the solid content of the sensing UC-SLNPs with concentrations up to 1250 µg·mL⁻¹ demonstrates good viability of the tumor cell-cultures. For the first time, intracellular T-sensing in living HeLa cells was performed, using the UC-SLNPs (Y-894 / DBOV-Mes in RBO 30 wt.% / squalene 30 wt.% / carnauba wax 40 wt.% / Tween-20) with T-sensitivity – up to 250 mK, optically achieved in the ambient environment, around the life-science relevant temperature of $T = 36\text{ }^{\circ}\text{C}$.

Summary and conclusions

Biomedical optical technologies, based on a mutual combination of photonics, nanotechnology, and bio-compatible materials, have made profound impact on the development of a plethora of minimally-invasive optical approaches in diagnosis and therapy of many diseases. These light-activated theranostic applications state imperative requirements: the excitation and the emission wavelengths must match the tissue transparency window; the excitation intensity must be enough low, in order to keep the light-organic matter interaction on acceptable level. The singlet oxygen is often generated as a result of the sensing process. Therefore, such a minimally invasive sensing must control its concentration and distribution.

All these fundamental requirements are fulfilled if the sensing method is based on the TTA-UC process performed in a bio-compatible organic nano-confined environment. The crucial advantages of the studied in this thesis the TTA-UC process are proved by the unique ability to distinguish in a non-ambiguous manner the strong dependence of this process on local temperature and the local oxygen content.

This thesis is devoted to the synthesis and complete characterization (optical, cytotoxicity effects) of UC-SLNPs. The study was performed in several steps:

- selection of the energetically optimized sensitizer/emitter dye pairs;
- selection of the natural components for core matrix formation possessing pronounced singlet oxygen scavenging properties;
- evaluation of the impact of the organogel matrix composition on the optical response of UC-dyes on small changes of the matrix temperature. Creation of the non-ambiguous temperature calibration curve;
- identification of the optimal organogel matrix composition regarding protection against singlet-oxygen damage and the creation of an oxygen calibration curve;
- synthesis of UC-SLNPs based on the optimal core matrix composition, minimizing the cytotoxicity of the sensing UC-SLNPs;
- evaluation of the temperature and oxygen sensitivity of the UC-SLNPs *in vitro*.

The natural waxes and vegetable oils were selected as core matrix material. The optical temperature sensing in a natural wax / vegetable oil organogel matrices via annihilation

upconversion was realized. The matrix composition demonstrates pronounced and sustainable singlet oxygen scavenging properties, allowing long-term operation of the T-sensors and O_2 -sensors in the ambient environment. The matrix-material ensures the significant increase of the rotational diffusion of the optically active molecules for a temperature interval centered at 36 °C. Consequently, the ratio of the dEF versus rSPh changes more than in 15 times.

The selected sensitizer/emitter molecular compositions (Y-894/DBOV-Mes) demonstrate the absorption/emission properties optimally matching the absorption/scattering spectra of the main tissue components of the human skin. The optimal UC-SLNPs composition (Y-894 / DBOV-Mes in RBO 30 wt.% / squalene 30 wt.% / carnauba wax 40 wt.% / Tween-20) demonstrates the monotonic increase of the dEF-signal and decrease of the rSPh-signal at monotonically increasing the sample temperature, that allows getting exclusively sustainable T-calibration curve. The upper limit of solid content of the UC-SLNPs was experimentally derived. Concentrations up to 1250 $\mu\text{g}\cdot\text{mL}^{-1}$ demonstrate the good viability of the tumor cell cultures. Intracellular T-sensing in living HeLa cells was performed using the optimal UC-SLNP composition with a T-sensitivity up to 250 mK, optically achieved in the ambient environment around $T = 36$ °C.

References

1. G. L. Semenza, Wiley Interdiscip. Rev.: *Syst. Biol. Med.*, **2010**, 2, 336-361.
2. K. Ito, T. Suda, *Nature Reviews: Molecular Cell Biology*, **2014**, 15, 243-256.
3. J. Bailey, T. Fukao, D. J. Gibbs, M. J. Holdsworth, S. C. Lee, F. Licausi, P. Perata, L. A. C. J. Voesenek, J. T. van Dongen, *Trends Plant Sci.*, **2012**, 17, 129-138.
4. A. A. Turschatov, S. B. Balushev, Handbook of Coherent-Domain Optical Methods, **2012**, 1289-1311.
5. N. V. Nazarova, Yu. S. Avlasevich, K. Landfester and S. Balushev, *Dalton Transactions*, **2018**, 47, 8605-8610.
6. S. Balushev, T. Miteva, V. Yakutkin, G. Nelles, A. Yasuda, G. Wegner, *Phys. Rev. Lett.*, **2006**, 97, 143903.
7. T. F. Schulze, J. Czolk, Y. Y. Cheng, B. Fückel, R. W. MacQueen, T. Khoury, M. J. Crossley, B. Stannowski, K. Lips, U. Lemmer, A. Colsmann, T. W. Schmidt, *J. Phys. Chem. C.*, **2012**, 116, 22794–22801.
8. Y. Murakami, H. Kikuchi, A. Kawai, *J. Phys. Chem. B.*, **2013**, 117, 2487–2494.
9. J. Hu, M. Chen, L. Wu, *Polym. Chem.*, **2011**, 2, 760-772.
10. J. M. Asua, Miniemulsion Polymerization, 2002, *Prog. Polym. Sci.*, 27, 1283 – 1346.
11. K. Landfester, *Angewandte Chemie International Edition*, **2009**, 48, 25, 4488-507.
12. Svagan, K. Landfester, J. Risbo, S. Balouchev, “*Capsule, namely nanocapsule, microcapsule or macrocapsule, having very low oxygen permeability*”, WO 2015/059179 A1; EP 2 865 443 A1.
13. K. Landfester, Yu. Avlasevich, D. Busko, F. Wurm, S. Balouchev, “*Single all-optical nano-sensor device probing simultaneously the local temperature and local oxygen concentration in soft-matter in non-invasive manner*”, WO 2016/150677 A1.
14. S. Chauvie, E. Bertone, F. Bergesio, A. Terulla, D. Botto, P. Cerello, *Computer Methods and Programs in Biomedicine*, **2018**, 156, 47 – 52.
15. I. Rauscher, C. Dewel, B. Haller, C. Rischapler, M. M. Heck, J. E. Gschwend, M. Schwaiger, T. Maurer, M. Eiber, *European Urology*, **2018**, 73, 656 – 661.

16. I. Pergoline, S. Crippa, M. Salgarello, G. Belfiori, S. Partelli, G. Ruffo, A. Pucci, G. Zamboni, F. Falconi, *Digestive and Liver Disease*, **2018**, 50, 84–90.
17. N. Almassi, M. A. Gorin, A. S. Purysko, S. P. Rowe, J. Kaouk, M. E. Allaf, S. C. Campel, A. Rhee, *Urology*, 2018, 113, 206 - 208.
18. M. C. H. Heknam, M. Rijpkema, E. N. Aarntzen, S. F. Mulder, J. F. Langenhuijsen, E. Oosterwijk, O. C. Boerman, W. J. G. Oyen, P. F. A. Mulders, *European Urology*, **2018**, 74, 257 – 260.
19. H. Chen, Y. Li, X. Gao, X. Shen, *Clinical Imaging*, **2018**, 52, 365 – 369.
20. P. Russo, M. Larobina, F. D. Lillo, S. D. Vecchio, G. Mettivier, *Nuclear Instruments and Methods in Physics Research A.*, **2016**, 809, 58–66.
21. A. T. Alves, D. de P. Faria, C. de G. Garneiro, A. T. Garcez, V. P. Gutierrez, W. das Neves, N. R. de Almeida, Y. Cury, R. Chammas, P. C. Brum, *Life Sciences*, **2018**, 206, 29 – 34.
22. D. M. Plecha, P. Faulhaber, *European Journal of Radiology*, **2017**, 94, A26 – A34.
23. H. J. Greenwood, *Clinical Imaging*, **2019**, 53, 169 – 173.
24. L. Wang, *Sensors*, **2017**, 17, 7, 1572.
25. D. Peer, J. M. Karp, S. Hong, O. C. Farkhzad, R. Margalit, R. Langer, *Nature Nanotechnology*, **2007**, 2, 751-760.
26. W. Jeong, J. Bu, L. J. Kubiatowicz, S. S. Chen, Y. Kim, S. Hong, *Nano Converg.*, **2018**, 5, 38.
27. X. Chen, S. Wong, *Cancer Theranostics*, Elsevier Inc., ISBN: 978-0-12-407722-5, **2014**, 544.
28. A. Ficai, A. M. Grumezescu, *Nanostructures for cancer therapy*, Elsevier Inc., ISBN: 978-0-323-46144-3, **2017**, 920.
29. A. Marcus, B. G. Gowen, T. W. Thompson, A. Iannello, M. Ardolino, W. Deng, L. Wang, N. Shifrin, D. H. Raulet, *Adv. Immunol.*, **2014**, 122, 91–128.
30. G. Ciofani, *Smart Nanoarticles for Biomedicine*, Elsevier Inc., ISBN: 978-0-12-814156-4, **2018**, 268.
31. P. Jozwiak, E. Forma, M. Brys, A. Krzeslak, *Frontiers in endocrinology*, **2015**, 5, article 145.
32. J. Zheng, *Oncol. Lett.*, **2012**, 4(6), 1151–1157.
33. L. Phan, S. Yeung, *Cancer Biol. Med.*, **2014**, 11, 1-19.

34. A.G. Hunderz, D. F. Bruley, Oxygen transport to tissue XX, *Springer Science + Business media*, **1998**, 705 p.
35. S. R. McKeown, *Br. J. Radio.*, **2014**, 87, 20130676.
36. D. M. Brizel, S. P. Scully, J. M. Harrelson, L. J. Layfield, J. M. Bean, L. R. Pronitz, T. V. Samulski, L. R. Prosnitz, M. W. Dewhirst, *Cancer research*, **1996**, 56, 941 – 943.
37. Y. Kim, Q. Lin, P.M. Glazer, Z. Yun, *Curr. Mol. Med.*, 2009, 9(4), 425–434; P. Vaupel, A. Mayer, *Cancer Metastasis Rev.*, **2007**, 26(2), 225-39.
38. J. S. Donner, S. A. Thompson, M. P. Kreuzer, G. Baffou, R. Quidant, *Nano Lett.*, **2012**, 12, 2107–2111.
39. R. Jayasundar, V. P. Singh, *Neurol India*, **2002**, 50(4), 436-9.
40. C.R. Lowe, *Trends in Biotechnology*, **1984**, 2, 3, 59–65.
41. R. Monosik, M. Stredansky, E. Sturdik, *Acta Chemica Slovaca*, **2012**, 5, 1, 109-120.
42. P. Damborsky, J. Svitel, J. Katrlík, *Essays in Biochemistry*, **2016**, 60, 91–100.
43. X. Fan, I. M. White, S. I. Shopova, H. Zhu, J. D. Suter, Y. Sun, *Analytica Chimica Akta*, **2008**, 620, 8-26.
44. A. Syahir, K. Usui, K. Tomizaki, K. Kajikawa, H. Mihara, *Microarrays*, **2015**, 4, 228-244.
45. K. A. Krohn, J. M. Link, R. P. Mason, *J of Nuclear Medicine*, **2008**, 49,129S-148S.
46. H. Liu, Y. Fan, J. Wang, Z. Song, H. Shi, R. Han, Y. Sha, Y. Jiang, *Sci Rep.*, **2015**, 5, 14879.
47. S. A. Binslem, M. R. Ahmad, Z. Awang, *J Teknologi (Sciences & Engineering)*, **2015**, 73, 71-80.
48. J. S. Chien, M. Mohammed, H. Eldik, M. M. Jbrahim, J. Martinez, S. P. Nichols, N. Wisniewski, B. Klitzman, *Sci Rep.*, **2017**, 7, 8255.
49. K. Okabe, R. Sakaguchi, B. Shi, S. Kiyonaka, *European Journal of Physiology*, **2018**, 470 (5), 717-731.
50. W. Hiesinger, S. A. Vinogradov, P. Atluri, J. R. Fitzpatrick III, J. R. Frederick, R. Livit, R. C. McCormick, J. R. Muenzer, E. C. Yang, N. A. Marotta, J. W. MacArthur, D. F. Wilson, J. J. Woo, *J Appl Physiol.*, **2011**, 110, 1460-1465.

51. E. G. Mik, T. Johannes, C. J. Zuurbier, A. Heinen, J. H. P. M. Houben-Weerts, G. M. Balestra, J. Stap, J. F. Beek, C. Ince, *Biophysical Journal*, **2008**, 95,3977-3990.
52. G. Nishimura, C. G. Pack, M. Tamura, *Experimental and Molecular Pathology*, 2007, 82 (2), 175-183.
53. M. Dramicanin, *Luminescence Thermometry*, ISBN: 978-0-08-102030-2, **2018**, 295.
54. M. Sauer, J. Hofkens, J. Enderlein, *Handbook of Fluorescence Spectroscopy and Imaging*, Wiley-VCH Verlag GmbH, ISBN: 978-3-527-31669-4, **2011**, 282.
55. J. M. de la Fuente, V. Grazu, *Nanobiotechnology*, Elsevier Inc., ISBN: 978-0-12-415769-9, **2012**, 520.
56. R. Narayan, *Nanobiomaterials. Nanostructured Materials for Biomedical applications*, Elsevier Inc., ISBN: 978-0-08-100716-7, **2017**, 574.
57. Sanali, M. K. Viswanadh, R. P. Singh, P. Agrawal, A. K. Mehata, D. M. Pawde, Narendra, R. Sonkar, M. S. Muthu, *Nanotechnology*, **2018**, 2 (1), 70-86.
58. A. L. Da Roz, M. Ferreira, F. de Lima Leite, O. N. de Oiveira Jr., *Nanoscience and its Applications*, Elsevier Inc., ISBN: 978-0-323-49780-0, **2016**, 238.
59. Y. Wang, K.C.L. Black, H. Luehmann, W. Li, Y. Zhang, X. Cai, et al., *ACS Nano*, **2013**, 7, 3, 2068–2077.
60. E. Lim, T. Kim, S. Paik, S. Haam, Y. Huh, K. Lee, *Chem. Rev.*, **2015**, 115, 327-394.
61. P. Xing, Y. Zhao, *Advanced Materials*, **2016**, 28, 34, 7304-7339.
62. C. Altavilla, E. Ciliberto, *Inorganic Nanoparticles: Synthesis, Applications, and Perspectives*, ISBN 9781439817612, Taylor and Francis Group, **2010**, 576.
63. R. Brayner, F. Fievet, T. Coradin, *Nanomaterials: A Danger or a Promise*, Springer, ISBN: 978-1-4471-4213-3, **2013**, 400.
64. C. Pietsch, A. Vollrath, R. Hoogenboom, U. S. Schubert, *Sensors*, **2010**, 10, 7979-7990.
65. X. Ma, Y. Wang, T. Zhao, Y. Li, L. C. Su, Z. Wang, G. Huang, B. D. Sumer, J. Gao, *J. Am. Chem. Soc.*, **2014**, 136, 11085–11092.
66. H. Y. Yoon, H. Koo, K. Y. Choi, S. J. Lee, K. Kim, I. C. Kwon, J. F. Leary, K. Park, S. H. Yuk, J. H. Park, *Biomaterials*, **2012**, 33, 3980–3989.

67. C. Wohnhaas, V. Mailaender, M. Droege, M. A. Filatov, D. Busko, Y. Avlasevich, S. Balushev, T. Miteva, K. Landfester, A. Turshatov, *Macromol. Biosci.*, **2013**, 13, 1422–1430.
68. T. Zhang, H. Xu, H. Wang, J. Zhu, Y. Zhai, X. Bai, B. Dong, H. Song, *RSC Adv.*, **2017**, 7, 28987-28987.
69. M. L. Immordino, F. Dosio, L. Cattell, *International Journal of Nanomedicine*, **2006**, 1, 3, 297 – 315.
70. G. S. Bangale, K. S. Rajesh, G. V. Shinde, *International Journal of Pharma Sciences and Research*, **2014**, 5, 11, 750 – 759.
71. Y. C. Barenholz, *Journal of Controlled Release*, **2012**, 160, 2, 117-134.
72. D. Bobo, K. J. Robinson, J. Islam, K. J. Thurecht, S. R. Corrie, *Pharm Res.*, **2016**, 33, 2373-2387.
73. H. Zhang, *OncoTargets and Therapy*, **2016**, 9, 3001-3007.
74. Onivyde (irinotecan liposome injection) [prescribing information]. Cambridge, MA: Merrimack Pharmaceuticals, Inc; **2015**.
75. C. L. Ventola, *Pharmacy and Therapeutics*, **2017**, 42, 12, 742-755.
76. J. P. May, S. D. Li, *Expert Opin Drug Deliv.*, **2013**, 10, 4, 511-527.
77. K. K. Ng, G. Zheng, *Chem. Rev.*, **2015**, 115, 11012-11042.
78. H. C. Huang, S. Barua, G. Sharma, S. K. Dey, K. Rege, *Journal of Controlled Release*, **2011**, 155, 344-357.
79. M. Jiao, P. Zhang, J. Meng, Y. Li, C. Liu, X. Luo, M. Gao, *Biomater. Sci.*, **2018**, 6, 726-745.
80. A. Borowik, K. Butowska, K. Konkel, R. Banasiuk, N. Derewonko, D. Wyrzykowski, M. Davydenko, V. Cherepanov, V. Styopkin, Y. Prilutskyy, P. Pohl, A. Krolicka, I. Piosik, *Nanomaterials*, **2019**, 9, 973.
81. A. D. Sezer, Recent Advances in Novel Drug Carrier Systems, InTech, ISBN: 978-953-51-0810-8, **2012**, 512.
82. A. Lunkoff, M. Arabski, A. Wegierek-Ciuk, M. Kruszewski, *Nanotoxicology*, **2012**, 7, 3.
83. M. Aliofkhazraei, Modern Surface Engineering Treatments, InTech, ISBN: 978-978-953-51-1149-8, **2013**, 230.

84. S. H. C. Askes, W. Pomp, S. L. Hopkins, A. Kros, S. Wu, T. Schmidt, S. Bonnet, *Small*, **2016**, 12, 40, 5579-5590.
85. Q. Duo, L. Jiang, D. Kai, C. Owh, X. J. Loh, *Drug Discovery Today*, **2017**, 22, 9, 1400-1411.
86. C. Parker, C. Hatchard, *Proc. Chem. Soc. Lond.*, **1962**, 14, 386-387.
87. W. Wang, Q. Liu, C. Zhan, A. Barhoumi, T. Yang, R. G. Wylie, P. A. Armstrong, D. S. Kohane, *Nano Lett.*, **2015**, 15, 6332-6338.
88. O. S. Kwon, H. S. Song, J. Conde, H. Kim, N. Artzi, J. H. Kim, *ACS Nano*, **2016**, 10, 1512-1521.
89. S. M. Borisov, C. Larndorfer, I. Klimant, *Adv. Funct. Mater.*, **2012**, 22, 4360-4368.
90. S. H. C. Askes, M. Kloz, G. Bruylants, J. T. Kennis, S. Bonnet, *Phys. Chem. Chem. Phys.*, **2015**, 17, 27380-27390.
91. S. H. C. Askes, A. Bahreman, S. Bonnet, *Angew. Chem. Int. Ed.*, **2014**, 53, 1029-1033.
92. Y. Y. Cheng, B. Fueckel, T. Khoury, R. G. C. R. Clady, M. J. Y. Tayebjee, N. J. Ekins-Daukes, M. J. Crossley, T. W. Schmidt, *J. Phys. Chem. Lett.*, **2010**, 1, 1795-1799.
93. C. Ye, L. Zhou, X. Wang, Z. Liang, *Phys. Chem. Chem. Phys.*, **2016**, 16, 10818-10835.
94. K. N. Solovyov, E. A. Borisovich, *Physics-Uspeski*, **2005**, 48, 3, 231-253.
95. V.V. Tuchin, Handbook of Coherent-Domain Optical Methods, ISBN 978-1-4614-5176-1, Springer Science+Business Media New York, **2013**, 1332.
96. A. Cristobal, A. Marti Vega, A. Luque Lopez, Next Generation of Photovoltaics, ISBN 978-3-642-23369-2, Springer-Verlag Berlin Heidelberg, **2012**, 356.
97. C. P. Hsu, *Accounts of Chemical Research*, **2009**, 42, 4, 509-518.
98. F. A. Villamena, Reactive Species Detection in Biology, Elsevier Inc., ISBN: 978-0-12-420017-3, **2015**, 340.
99. V. Gray, D. Dzebo, M. Abrahamsson, B. Albinsson, K. Moth-Poulsen, *Phys. Chem. Chem. Phys.*, **2014**, 16, 22, 10345-10352.
100. S. Braslavsky, *Pure Appl. Chem*, **2007**, 79, 3, 293-465.

101. D. Busko, Noncoherent Upconversion in Multimolecular Organic Systems, **2013**, 141.
102. M. A. Filatov, I. Z. Ilieva, K. Landfester, S. Balushev, *Conference Paper: Nanotech*, **2013**, At Washington D. C., 3.
103. S. Amemori, Y. Sasaki, N. Yanai, N. Kimizuka, *J. Am. Chem. Soc.*, **2016**, 138, 8702– 8705.
104. S. Nonell, C. Flors, Singlet Oxygen: Applications in Biosciences and Nanosciences, ISBN: 978-1-78262-220-8, **2016**, 472.
105. M. A. Filatov, S. Balushev, K. Landfester, *Chem. Soc. Rev.*, **2016**, 45, 4668– 4689.
106. M. Laing, *Journal of Chemical Education*, **1989**, 6, 66, 453-455.
107. X. Cui, J. Zhao, Y. Zhou, J. Ma and Y. Zhao, *J. Am. Chem. Soc.*, **2014**, 136, 26, 9256–9259.
108. R. Tao, J. Zhao, F. Zhong, C. Zhang, W. Yang and K. Xu, *Chem. Commun.*, **2015**, 51, 12403–12406.
109. A. Monguzzi, M. Mauri, A. Bianchi, M. K. Dibbanti, R. Simonutti, F. Meinardi, *J. Phys. Chem. C*, **2016**, 120, 5, 2609–2614.
110. S. H. C. Askes, P. Brodie, G. Bruylants, S. Bonnet, *J. Phys. Chem. B*, **2017**, 121, 4, 780–786.
111. G. Massaro, J. Hernando, D. Ruiz-Molina, C. Roscini, L. Latterini, *Chem. Mater.*, **2016**, 28, 738.
112. J. M. Aubry, C. Pierlot, J. Rigaudy, R. Schmidt, *Acc. Chem. Res.*, **2003**, 36, 668-675.
113. C. S. Foote, S. Wexler, *J. Am. Chem. Soc.*, **1964**, 86, 18, 3879-3880
114. N. J. Turro, M. F. Chow, J. Rigaudy, *J. Am. Chem. Soc.*, **1981**, 103, 24, 7218-7224.
115. H. H. Wasserman, J. R. Scheffer, *J. Am. Chem. Soc.*, **1967**, 89, 3073 – 3075.
116. M. Balci, *Chem. Rev.*, **1981**, 81, 91-108.
117. M. A. Filatov, M. O. Senge, *Mol. Syst. Des. Eng.*, **2016**, 1, 219-346.

118. J. A. Spencer, F. Ferraro, E. Roussakis, A. Klein, J. Wu, J. M. Runnels, W. Zaher, L. J. Mortensen, C. Alt, R. Turcotte, R. Yusuf, S. A. Vinogradov, D. T. Scadden, C. P. Lin, *Nature*, **2014**, 508, 269-273.
119. M. A. Filatov, S. Balushev, K. Landfester, *Chem. Soc. Rev.*, **2016**, 45, 4631-4852.
120. K. Landfester, A. Svagan, J. Risbo, S. Balouchev, *WO 2015/059179 A1, EP 2 865 443 A1*, **2015**.
121. K. Landfester, M. Filatov, Yu. Avlasevich, D. Busko, A. Turshatov, F. Wurm, F. Marsico, S. Balouchev, *EP2851407A1, WO 2015/044129 A1*, **2015**.
122. J. Zhou, Q. Liu, W. Feng, Y. Sun, F. Li, *Chem. Rev.*, **2015**, 115, 395-465.
123. S. H. C. Askes, N. Lopez Mora, R. Harkes, R. I. Koning, B. Koster, T. Schmidt, A. Kros, S. Bonnet, *Chem. Commun.*, **2015**, 51, 9137-9140.
124. J. H. Kim, J. H. Kim, *J. Am. Chem. Soc.*, **2012**, 134, 17478-17481.
125. Q. Liu, T. S. Yang, W. Feng, F. Y. Li, *J. Am. Chem. Soc.*, **2012**, 134, 5390-5397.
126. C. Wohnhaas, A. Turshatov, V. Mailander, S. Lorenz, S. Balushev, T. Miteva, K. Landfester, *Macromol. Biosci.*, **2011**, 11, 772-778.
127. S. M. Borisov, R. Saf, R. Fischer, I. Klimant, *Inorg. Chem.*, **2013**, 52, 1206-1216.
128. K. Börjesson, P. Rudquist, V. Gray, K. Moth-Poulsen, *Nat. Comm.*, **2016**, 7, 12689.
129. Z. Huang, X. Li, M. Mahboub, K. M. Hanson, V. M. Nichols, H. Le, M. L. Tang, C. J. Bardeen, *Nano Lett.*, **2015**, 15, 5552-5557.
130. C. Mongin, S. Garakyaraghi, N. Razgoniaeva, M. Zamkov and F. N. Castellano, *Science*, **2016**, 351, 369-372.
131. T. F. Schulze, J. Czolk, Y. Y. Cheng, B. Fuckel, R. W. MacQueen, T. Khoury, M. J. Crossley, B. Stannowski, K. Lips, U. Lemmer, *J. Phys. Chem. C*, **2012**, 116, 22794-22801.
132. W. Q. Zou, C. Visser, J. A. Maduro, M. S. Pshenichnikov, J. C. Hummelen, *Nature Photonics*, **2012**, 6, 560-564.

133. P. Duan, N. Yanai, H. Nagatomi, N. Kimizuka, *J. Am. Chem. Soc.*, **2015**, 137, 1887-1894.
134. T. F. Schulze, T. W. Schmidt, *Energy & Environmental Science*, **2015**, 8, 103-125.
135. R. E. Keivanidis, S. Balushev, G. Lieser, G. Wegner, *ChemPhysChem.*, **2009**, 10, 2316-2326.
136. J. M. Aubry, B. Mandard-Cazin, M. Rougee, R. V. Bensasson, *J. Am. Chem. Soc.*, **1995**, 117, 36, 9159-9164.
137. M. Seip, H. D. Brauer, *J. Am. Chem. Soc.*, **1992**, 114, 12, 4486-4490.
138. J. C. Pouilly, J. P. Schermann, N. Nieuwjaer, F. Lecomte, G. Gregoire, C. Desfrancois, G. A. Garcia, L. Nahon, D. Nandi, L. Poisson, M. Hochlaf, *Phys. Chem. Chem. Phys.*, **2010**, 12, 3566-3572.
139. S. A. Hejazi, O. I. Osman, A. O. Alyoubi, S. G. Aziz, R. H. Hilal, *Int. J. Mol. Sci.*, **2016**, 17, 11, 1893.
140. J. A. Frey, R. Leist, A. Mueller, S. Leutwyler, *ChemPhysChem*, **2006**, 7, 1494-1499.
141. S. Benz, S. Nötzli, J. S. Siegel, D. Eberli, H. J. Jessen, *J. Med. Chem.*, **2013**, 56, 10171-10182.
142. C. Changtong, D. W. Carney, L. Luo, C. A. Zoto, J. L. Lombardi, R. E. Connors, *J. Photochem. Photobiol. A: Chemistry*, **2013**, 260, 9-13.
143. D. Saini, N. K. Rangra, P. C. Behra, Exploring the Biological Potential of Pyridones, Lambert Academic Publishing, ISBN-13:978-3-659-39505-5, **2015**, 128.
144. A. J. Svagan, D. Busko, Yu. Avlasevich, G. Glasser, S. Balushev, K. Landfester, *ACS Nano*, **2014**, 8, 8198-820.
145. S. McN. Sieburth, C. H. Lin, D. Rucando, *J. Org. Chem.*, **1999**, 64, 950-953.
146. Ch. Reichardt, Solvent and Solvent Effects in Organic Chemistry, ISBN: 3-527-30618-8, Wiley-VCH Verlag GmbH, **2003**, 629.
147. H. Gudapati, M. Dey, I. Ozbolat, *Biomaterials*, **2016**, 102, 20-42.
148. I. Donderwinkel, J. C. M. van Hest, N. R. Cameron, *Polym. Chem.*, **2017**, 8, 4451-4471.

149. P. R. Ogilby, *Chem. Soc. Rev.*, **2010**, 39, 3181–3209.
150. T. T. Ruckh, H. A. Clark, *Anal. Chem.* **2014**, 86, 1314–1323.
151. X. Wang, O. S. Wolfbeis, *Chem. Soc. Rev.*, **2014**, 43, 3666–3761.
152. X. Wang, O. S. Wolfbeis, R. J. Meier, *Chem. Soc. Rev.*, **2013**, 42, 7834–7869.
153. D. B. Papkovsky, R. I. Dmitriev, *Chem. Soc. Rev.*, **2013**, 42, 8700–8732.
154. K. Okabe, N. Inada, C. Gota, Y. Harada, T. Funatsu, S. Uchiyama, *Nature Communication*, **2012**, 3, 705.
155. A. E. Albers, E. M. Chan, P. M. McBride, C. M. Ajo-Franklin, B. E. Cohen, B. A. Helms, *J. Am. Chem. Soc.*, **2012**, 134, 9565–9568.
156. E. J. McLaurin, L. R. Bradshaw, D. R. Gamelin, *Chem. Mater.*, **2013**, 25, 1283–1292.
157. J. Donner, S. Thompson, M. Kreuzer, G. Baffou, R. Quidant, *Nano Lett.*, **2012**, 12, 2107–2111.
158. S. Balushev, K. Katta, Yu. Avlasevich, K. Landfester, *Mater. Horiz.*, **2016**, 3, 478–486.
159. A. R. Patel, M. Babaahmadi, A. Lesaffer, K. Dewettinck, *J. Agric. Food Chem.*, **2015**, 63, 4862–4869.
160. P. Goufo, H. Trindade, *Food Science & Nutrition*, **2014**, 2, 2, 75–104.
161. A. E. Midaoui, Y. Haddad, R. Couture, *Nutrition*, 2016, 32, 1132–1137.
162. Eu. Choe, D. B. Min, *Comprehensive reviews in food science and food safety*, **2006**, 5, 169–186.
163. A. L. Petrou, P. L. Petrou, Th. Ntanos, A. Liapis, *Antioxidants*, **2018**, 7, 35.
164. D. Guillaume, Z Charrouf, *Alternative Medicine Review*, **2011**, 16, 3, 275–279.
165. A. Drissia, J. Gironab, M. Cherkia, G. Godas, A. Derouichea, M. E. Messalc, R. Sailea, A. Kettania, R. Sola, L. Masanab, A. Adlouni, *Clinical Nutrition*, **2004**, 23, 1159–1166.
166. A. Gliszczyńska-Świgło, E. Sikorska, I. Khmelinskii, M. Sikorski, *Pol. J. Food Nutr. Sci.*, **2007**, 57, 4, 157–161.
167. V.R. Pestana, R.C. Zambiazzi, C.R.B. Mendonça, M.H. Bruscatto, M.J. Lerma, G. Ramis-Ramos, *J. Amer. Oil Chem. Soc.*, **2008**, 85, 11, 1013–1019.
168. M. E. Carrin, A. A. Carelli, *Eur. J. Lipid Sci. Technol.*, **2010**, 112, 697–707.

169. Sh. A. Shahid Chatha, F. Anwar, M. Manzoor, J. Bajwa, *Grasas Y Aceites*, **2006**, 57, 2, 328-335.
170. P. Sawadikiat, P. Hongsprabhas, *International Journal of Food Science and Technology*, **2014**, 49, 2030–2036.
171. K. Rabie, K. Mourad, E. Meryem, D. Zouhra, B. Abdelaziz, Ch. Yahia, A. Katim, *J. Chem. Pharm. Res.*, **2016**, 8, 11, 173-179.
172. L. M.L. Nollet, F.I Toldra, *Handbook of Food Analysis*, **2015**, ISBN 97-814-665565-46, CRC Press, 3rd edition, 1568.
173. E. L. Bakota, J. K. Winkler-Moser, H. S. Hwang, M. J. Bowman, D. E. Palmquist, S. X. Liu, *Eur. J. Lipid Sci. Technol.*, **2013**, 115, 847–857.
174. L. M. Diamante, T. Lan, *Journal of Food Processing*, **2014**, 2014, 6.
175. R. G. Craig, J. D. Eick, F. A. Peyton, *J. dent. Res.*, **1965**, 44, 6, 1308-1316.
176. S. H. Yun, S. J. J. Kwok, *Nat Biomed Eng.*, **2017**, 1, 0008.
177. T. Sarna, R.C. Sealy, *Photochem. Photobiol.*, **1984**, 39, 69-74
178. R.P. Crippa, V. Cristofolletti, N. Romeo, *Biochim. Biophys. Acta*, **1978**, 538, 164-170.
179. A. H. Guenther, *International trends in Applied Optics*, SPIE Press, **2002**, 699
180. D. M. Coles, Q. Chen, L. C. Flatten, J. M. Smith, K. Muellen, A. Narita, D. G. Lidzey, *Nano Lett.*, **2017**, 17, 9, 5521–5525.
181. N. Hoshyar, S. Gray, H. Han, G. Bao, *Nanomedicine (Lond)*, **2016**, 11, 6, 673–692.
182. A. H. Faraji, P. Wipf, *Bioorg. Med. Chem.*, **2009**, 17, 2950–2962.

List of abbreviations

AIDS	Acquired Immune Deficiency Syndrome
ATP	Adenosine triphosphate
AO	Argan oil
BCP	3,4,9,10-tetra(butoxycarbonyl) perylene
BDP	3,10-bis(3,3-dimethylbutyn1-yl) perylene
BMP	3,9(10)-bis(3,5-dimethoxyphenyl) perylene
Brij-78	Poly(ethylene glycol octadecyl ether), non-ionic surfactant
CT	Computed tomography
CW	Continuous Wave
CLSM	Confocal Laser Scanning Microscopy
DBOV-Mes	Dibenzo[hi,st]ovalene
dEF	Delayed Emitter Fluorescence
DMEM	Dulbecco's Modified Eagle Medium
DMSO	Dimethyl sulfoxide
DNA	Deoxyribonucleic acid
EPO	Endoperoxid
FDA	Food and Drug Administration
FSC	Fetal Bovine Serum
GAET	Glycolic acid ethoxylate 4-nonylphenyl ether
HLB	Hydrophilic-Lipophilic Balance
ISC	Intersystem Crossing
MRT	Magnetic Resonance Imaging

MTS	3-(4,5-dimethylthiazol-2-yl)-5-(3-carboxymethoxyphenyl)-2-(4-sulfophenyl)-2H-tetrazolium
NMR	Nuclear Magnetic Resonance
NP	Nanoparticle
OMe-PEG ₃₅₀	Poly(ethylene glycol) methyl ether
PBS	Phosphate-Buffered Saline
PEEP	Poly(ethyl ethylene phosphate)
PET	Positron Emission Computed Tomography
PdTBP	Meso-tetraphenyl-tetrabenzo[2,3]porphyrin palladium (II)
PO	Peanut oil
QD	Quantum dots
RBO	Rice Bran Oil
rSPh	Residual Sensitizer Phosphorescence
RPMI 1640	Roswell Park Memorial Institute medium
SC	Scavenging Compound
SLNP	Solid-Lipid Nanoparticle
SPECT	Single Photon Emission Computed Tomography
SN-38	7-Ethyl-10-hydroxy-camptothecin
SOG	Singlet Oxygen Scavenger
TTA	Triplet-Triplet Annihilation
TTA-UC	Triplet-Triplet Annihilation Upconversion
TTT	Triplet-Triplet Transfer
Tween-20	Polysorbate 20, non-ionic surfactant
Tween-80	Polysorbate 80, non-ionic surfactant

TX-100	Triton X-100, non-ionic surfactant
UC	Upconversion
UCNP	Upconversion Nanoparticles
UC-SLNP	Upconversion Solid-Lipid Nanoparticle
UV	Ultraviolet
WAT	White Adipose Tissue
Y-894	Pd(II) mixture of benzo/naphto porphyrin

Acknowledgments

This work was performed under the European Union's Horizon 2020 Research and Innovation Program under Grant agreement No. 732794—project HYPOSENS.

First of all, I would like to express my greatest gratitude to my advisor [REDACTED] [REDACTED] for allowing me to join her research team and for offering such an exciting project to me. It was my pleasure to work and study at Max Planck-Institute for Polymer research under the supervision of [REDACTED] with her continuous support and motivation.

I extend my sincere gratitude to my co-supervisor, [REDACTED] for his wonderful support and rewarding discussions throughout the period of these studies. I am very thankful for your continuous guidance and the great effort during both the research and preparation of my manuscripts and this thesis.

I want to acknowledge [REDACTED] for his continuous support, helpful advice, and valuable discussions throughout my Ph.D. study.

Sincere thanks also to [REDACTED] for your invaluable help and sharing experience at the start of my research.

Special thanks to [REDACTED] [REDACTED], and [REDACTED] for their work on the cell culture experiments. I genuinely appreciate our friendship and effort throughout this work.

I am also grateful to [REDACTED] for the TEM measurement and help with the analysis of the results.

Furthermore, I would like to thank my splendid colleagues, [REDACTED] [REDACTED] [REDACTED] [REDACTED] and [REDACTED] for your endless friendship and support in all manners during this work. It has been a pleasure working together.

I extend my sincere gratitude to all the members of Max Planck Institute for Polymer Research for providing a friendly, exciting, and stimulating environment.

Last but not least, I would like to express my deepest gratitude to my beloved family and friends for their immeasurable love and support throughout this work and my life in general.

Scientific contributions

Publications

- N. V. Nazarova, Yu. S. Avlasevich, K. Landfester, S. Balushev «Stimuli-responsive protection of optically excited triplet ensembles against deactivation by molecular oxygen» // Dalton Trans., 2018, 47, pp. 8605-8610.
- N. V. Nazarova, Yu. S. Avlasevich, K. Landfester, S. Balushev «All-optical Temperature Sensing in Organogel Matrices *via* Annihilation Upconversion», ChemPhotoChem, 2019, 1020-1026.
- N. V. Nazarova, Yu. S. Avlasevich, R. Thiramanas, V. Mainlaender, K. Landfester, S. Balushev «Sensing technique based on Solid Lipid Upconverting Nanoparticles for early-stage cancer diagnostic», in progress.
- B. Jyisan, N. Nazarova, R. Thiramanas, Yu. Avlasevich, V. Mailaender, S. Baloushev, K. Landfester, «Temperature sensing in cells using polymeric upconversion nanoparticles», Advanced Biosystems, submitted.

Conferences

- N. Nazarova, Yu. Avlasevich, St. Balushev, K. Landfester «Upconversion in Organic Systems for temperature and oxygen sensing» // 51st winter seminar “Biophysical Chemistry, Molecular Biology and Cybernetics of Cell Functions», Klosters, 2016, poster.
- N. Nazarova, Yu. Avlasevich, St. Balushev, K. Landfester «Annihilation upconversion as an all-optical temperature sensing tool for life-science» // 60th scientific conference for young students of physics and natural sciences “Open Readings 2017”, Vilnius, 2017, p. 108, talk.
- B. Jyisan, R. Thiramanas, N. Nazarova, Y. Avlasevich, V. Mailänder, S. Balushev, K. Landfester «Temperature sensing in cells by polymeric upconversion nanocapsules» // 33rd conference of the European Colloid and Interface Society (ECIS) ECIS, Leuven, 2019, talk.
- The international research training group "Guided light, tightly packed: novel concepts, components and applications", Jena, 2019.